Three jet production in neutral current deep inelastic scattering with ZEUS at HERA

by

Liang Li

A dissertation submitted in partial fulfillment of the

requirements for the degree of

Doctor of Philosophy

(Physics)

at the

University of Wisconsin – Madison

2005

Abstract

Trijet production rates in neutral current deep inelastic scattering have been measured in the range of exchanged boson virtualities $10 < Q^2 < 5000\,\mathrm{GeV}^2$. The data were taken at the ep collider HERA with centre-of-mass energy $\sqrt{s} = 318\,\mathrm{GeV}$ using the ZEUS detector and correspond to an integrated luminosity of $82.2\,\mathrm{pb}^{-1}$. Jets were identified in the Breit frame using the k_T-cluster algorithm in the longitudinally invariant inclusive mode. Measurements of differential dijet and trijet cross sections are presented as functions of jet transverse energy ($E^{\mathrm{jet}}_{T,B}$), pseudorapidity ($\eta^{\mathrm{jet}}_{\mathrm{LAB}}$) and Q^2 with $E^{\mathrm{jet}}_{T,B} > 5\,\mathrm{GeV}$ and $-1 < \eta^{\mathrm{jet}}_{\mathrm{LAB}} < 2.5$. Next-to-leading-order QCD calculations describe the data well. The value of the strong coupling constant $\alpha_s(M_Z)$, determined from the ratio of the trijet to dijet cross sections, is $\alpha_s(M_Z) = 0.1179 \pm 0.0013\ (\mathrm{stat.})^{+0.0028}_{-0.0046}\ (\mathrm{exp.})^{+0.0064}_{-0.0046}\ (\mathrm{th.})$.

Acknowledgements

I would like to thank my advisors, Wesley Smith and Don Reeder, for their invaluable support during my Ph.D. period. Thanks to Don Reeder for his knowledgeable answers and deep insight into physics, which helped me understand my analysis in a wider context. My direct supervisor, Wesley Smith's enthusiasm and integral view on both research and detector hardware, has made a deep impression on me. Their concern and dedication for the students is rare and laudable.

Special Thanks to Nils Krumnack, for being such a good partner and putting an immense effort in this analysis.

Thanks to the former and current QCD group coordinators at ZEUS, Juan Terron, Sergei Chekanov, Mark Sutton, Alexandre Savin and Claudia Glasman, for their valuable suggestions and discussions.

Thanks to all the Wisconsin group members at ZEUS: Sascha, Matti, Dorian, Sabine, Adam, Pat and Michelle. My experience in the group is certainly enjoyable and entertaining. Thanks to the previous group members, Torsten, Richard and Doug, for being great hosts and introducing the ZEUS way of physics during my first summer visit at DESY.

Thanks to all my friends at Madison and Hamburg, especially to my buddy Huican.

I am deeply grateful for my family. The love and support from my parents and my wife is the best thing happened to me in the world. I would like to thank my wife for the uncounted sacrifices she has made for our relationship and her unique personality

that has made life such a wonderful journey. One of the best experience that we lived through in this period was the birth of my son Kehao, who brings a new meaning and pleasure to our life. To them, I dedicate this thesis.

Contents

List of Tables

List of Figures

Chapter 1

Introduction

The basic of particle physics embraces two fundamental questions: what are the true elements that build up this world and how do those elements interact with each other in the "building" process? Ever since the birth of particle physics, those questions have been driving and directing particle physics research.

1.1 Standard Model

The Standard Model is by far the most successful theory of particle physics that provides an answer to the above questions. The Standard Model assumes that the elementary constituents of matter are quarks and leptons which are fermions of spin 1/2, see Table 1.1. There are six leptons (electron, muon, tau and their associated neutrinos) and six quarks (down, up, strange, charm, bottom and top). For each of them there exists an anti-particle with the same properties, but opposite quantum numbers.

To describe how these particles interact, there are four known forces in nature: Gravity, Electromagnetism, the Weak Force and the Strong Force. Fermions interact with each other through forces mediated by the exchange of bosons: γ, Z, $W^{\pm}$ and

	Particle	Charge (e)	Spin	Mass	Color
Quarks	up	$+\frac{2}{3}$	$\frac{1}{2}$	3 MeV	Yes
	down	$-\frac{1}{3}$	$\frac{1}{2}$	6 MeV	
	charm	$+\frac{2}{3}$	$\frac{1}{2}$	1.2 GeV	
	strange	$-\frac{1}{3}$	$\frac{1}{2}$	120 MeV	
	top	$+\frac{2}{3}$	$\frac{1}{2}$	174 GeV	
	bottom	$-\frac{1}{3}$	$\frac{1}{2}$	4.25 GeV	
Leptons	electron	-1	$\frac{1}{2}$	0.51 MeV	No
	muon	-1	$\frac{1}{2}$	106 MeV	
	tau	-1	$\frac{1}{2}$	1.78 GeV	
	ν_e	0	$\frac{1}{2}$	< 3 eV	
	ν_μ	0	$\frac{1}{2}$	< 0.19 MeV	
	ν_τ	0	$\frac{1}{2}$	< 18.2 MeV	
Bosons	γ	0	1	0	Yes
	$W^\pm$	± 1	1	80.4 GeV	No
	Z	0	1	91.2 GeV	
	gluon	0	1	0	

Table 1.1: Fermions (quarks and leptons) and gauge bosons

gluon.

The electromagnetic force is mediated by photons and is described by the well-known classic Electrodynamics at the macroscopic scale and is described by the Quantum Electrodynamics (QED) at the microscopic scale ("quantum level"). The weak force and strong force only act at the microscopic scale. The weak force is mediated by the massive bosons Z^0 and $W^\pm$. The weak force and electromagnetic force are both described by the electro-weak theory, thus they are also called the Electroweak Force. The strong force is mediated by gluons and is described by the Quantum Chromodynamics (QCD). The gravity force is described by the general theory of relativity at the macroscopic scale and there are theories of quantum gravity at the microscopic scale which predict the existence of force mediator "graviton", however, such a boson

particle has not been observed yet.

The Standard Model of particle physics represents our understanding of the classification schemes of the fundamental particles, and the way these particles behave. It is based on the principles of quantum field theory, and has successfully described almost all experimental data which has tested the electroweak and strong forces.

1.2 Quantum Chromodynamics

1.2.1 Confinement of Quarks and Coupling Constant

Quarks cannot be observed in nature as free particles, but they cluster into groups of two or three to form bound states ("colorless") called hadrons. Quantum Chromodynamics (QCD) provides an explanation for the confinement of quarks. Quarks exist in three different quantum numbers called "colors" and are bound by the strong force, overruling the electromagnetic repulsion of same-signed charged quarks, and this force is mediated by the colored gluon.

The place of electrical charge in QED is taken by "color charge" in QCD. Unlike electrical charge, color charge comes in three types: red, green, and blue (and their respective anti-colors). In QED, the force mediator photon does not have an electrical charge but in QCD the gluons are also colored, which not only allows them to interact with quarks but also with other gluons. There are eight gluons in QCD, each carrying color plus anti-color ($r\bar{g}$, $g\bar{r}$, etc.). The strength of the strong force interactions is given by the strong coupling constant, α_s, which is analogous to the electroweak coupling constant, α_{EM}.

1.2.2 Coupling Constant and Asymptotic Freedom

α_s is the only one fundamental constant of QCD that must be determined from experiment. α_s varies according to the separation distance between the interacting particles. The strength of the interaction, or magnitude of the coupling, decreases at short distances (large momentum transfer or high energies) and increases rapidly at large distances. In the very short distance limit, quarks and gluons can be treated as free particles since their coupling is small ("asymptotic freedom"). It is only in this domain that high-precision tests, similar to those in QED, can be performed using perturbative expansion of terms proportional to different orders of α_s. ("perturbative QCD").

1.2.3 Perturbative QCD and Renormalization Scheme

Perturbative QCD (pQCD) provides predictions for a physics observable associated to a given particle scattering process using the Feynman rules, which effectively sum the amplitudes of all possible Feynman diagrams for that scattering process. Some contributions come from self-interactions, like loop diagrams, where an integration over the loop momenta is calculated. Divergencies appear when the loop momenta tend to infinity (small wavelength). This problem can be solved by a technique known as a Renormalization Scheme (RS) [1] in which a cutoff μ_R on the loop momenta is introduced.

As a result of RS, the strong coupling constant α_s acquires a dependence on μ_R. As μ_R can have an arbitrary value, the value of any physical observable should be independent of μ_R. This requirement is expressed mathematically through the

Renormalization Group Equation:

$$\mu_R^2 \frac{\mathrm{d}C}{\mathrm{d}\mu_R^2} = \left(\mu_R^2 \frac{\partial}{\partial \mu_R^2} + \mu_R^2 \frac{\partial \alpha_s}{\partial \mu_R^2} \frac{\partial}{\partial \alpha_s} \right) C = 0 \tag{1.1}$$

where C is the physics observable of interest. Equation 1.1 shows the dependence of α_s on the renormalization scale μ_R. This dependence has been calculated explicitly and α_s can be written in reverse powers of $ln(\mu_R^2)$ with a perturbative expansion. At the first order,

$$\alpha_s(\mu_R^2) = \frac{12\pi}{(11n - 2n_f) ln(\mu_R^2/\lambda^2)} \tag{1.2}$$

where $n = 3$ is the number of colors, n_f is the number of quark flavors with mass less than the energy scale μ_R and λ is a dimensional parameter introduced to provide a parameterization of the μ_R dependence of α_s. The definition of λ is arbitrary and typically between 100 to 300 MeV.

If n_f is smaller than 17, α_s tends to zero as μ_R gets large, proving the characteristic of the "asymptotic freedom". In this analysis, $n_f = 5$. At low μ_R, α_s gets large. Therefore at large distances the strong force becomes so large that it is not possible to observe free quarks outside bound states ("color confinement"). The renormalization scale μ_R is the scale at which α_s is evaluated. The most sensible choice for α_s is the value of α_s at a fixed-reference scale μ_0. It has become standard to choose $\mu_0 = M_Z$ (the mass of Z).

1.3 Deep Inelastic Scattering

Deep Inelastic Scattering (DIS), in which a high energy lepton scatters from a proton (or neutron), is an ideal environment to study the strong force and QC., In particular, it tests the currently accepted understanding of how quarks and gluons

interact with each other inside the proton and illustrates the structure of proton. The term "inelastic" refers to the fact that the proton breaks up, resulting in a system of particles. The term "deep" refers to the regime where the momentum transferred by the lepton and the center-of-mass energy of the boson-proton system are larger than the mass of the proton. The scattering can proceed via neutral current (exchange of a virtual photon or Z) or charged current (exchange of W^+ or W^-) processes. An example of neutral current positron-proton scattering is shown in Fig. 1.1.

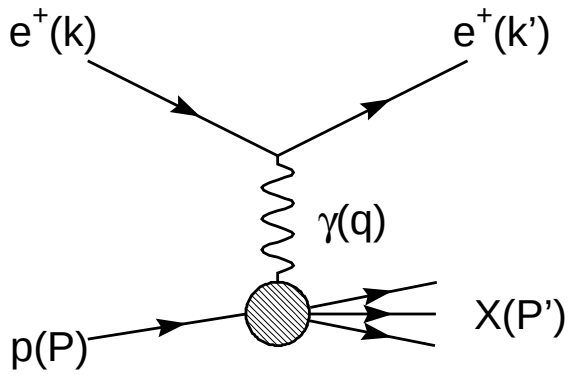

Figure 1.1: Neutral current inelastic scattering

1.3.1 DIS Kinematics

The initial state lepton with four-momentum k and initial state proton with four-momentum P exchange a virtual photon with four-momentum q. The final state lepton has four-momentum k'. The proton breaks up into a system of particles with large invariant mass.

Lorentz invariant variables, x, y and Q^2 are used to describe DIS processes:

$$Q^2 = -q^2 = -(k - k')^2 \tag{1.3}$$

- Q^2 is the negative square of four-momentum transfer, q. It is also known as the virtuality of the exchanged photon. It is related to the distance at which the proton structure is "probed" by the exchanged photon. In the proton's rest frame, the wavelength of the virtual photon is $\lambda = \frac{1}{|q|} \simeq \frac{2xM_p}{Q^2}$, where M_p is the mass of the proton. Therefore a high energy probe (a high value of Q^2) resolves smaller structure in the proton.

$$x = \frac{Q^2}{2P \cdot q} \tag{1.4}$$

- x is the fraction of the proton momentum involved in the scattering, within the context of the Quark Parton Model (Section 1.3.3) where the proton is made of quarks alone.

$$y = \frac{P \cdot q}{P \cdot k} \tag{1.5}$$

- y is the inelasticity, which is the fraction of the lepton's energy transfered to the proton in the proton's rest frame. y is also related to the scattering angle θ^*, in the lepton-quark center-of-mass frame: $y = \frac{1}{2}(1 - \cos\theta^*)$.

$$s = (k + P)^2 \simeq 4E_pE_e \tag{1.6}$$

- s is the center-of-mass energy of the lepton-proton system, where E_P and E_e are the incoming energies from the proton and lepton respectively.

- From above equations, it can be shown that x, y and Q^2 are related by the

square of the center-of-mass energy s:

$$s = \frac{Q^2}{xy} \tag{1.7}$$

1.3.2 Inclusive DIS Cross Section and Structure Functions

The general form of the inclusive DIS cross section is written in terms of its leptonic tensor ($L_{\mu\nu}$) and hadronic tensor ($W^{\mu\nu}$):

$$\mathrm{d}\sigma = L_{\mu\nu} W^{\mu\nu} \tag{1.8}$$

$L_{\mu\nu}$ comes from the leptonic part of the interaction. It can be calculated exactly from QED and is symmetric with respect to μ and ν exchange for an unpolarized beam of electrons. The hadronic tensor, $W^{\mu\nu}$, serves to parameterize the structure of the proton and the details of the interaction at the hadronic vertex. $W^{\mu\nu}$ can be written in terms of proton structure functions in QCD. The details can be found in [2]. The ep differential cross section can be expressed in terms of structure functions (F_1, F_2, F_L and F_3):

$$\frac{\mathrm{d}^2\sigma(e^{\pm}p)}{\mathrm{d}x\mathrm{d}Q^2} = \frac{4\pi\alpha_s^2}{xQ^4}[Y_+ F_2(x,Q^2) - y^2 F_L(x,Q^2) \mp Y_- x F_3(x,Q^2)] \tag{1.9}$$

where $Y_\pm = 1 \pm (1-y)^2)$ and the initial lepton can have positive or negative charge. F_2 is the contribution to the cross section due to interaction between transversely polarized virtual bosons and spin 1/2 quarks. It is related to the density of quarks and anti-quarks in the proton. The longitudinal structure function, $F_L = F_2 - 2xF_1$, is the contribution due to longitudinally polarized virtual bosons. Finally, F_3 is the contribution due to parity violating exchange of a Z-boson and only makes a significant contribution in the region $Q^2 > M_Z^2$.

1.3.3 Quark Parton Model and Scaling Violation

When DIS events were first studied, Quark Parton Model (QPM) was developed to describe the structure of the proton. QPM assumes that the proton is made of only "quarks" which are quasi-free point-like objects ("partons"). Therefore, the inclusive DIS cross section is the incoherent sum of the cross sections for elastic scattering off the individual partons. This implies that the structure functions should be independent of Q^2, which is the resolution of the scattering, since probing a point-like object with increasing resolution will not reveal any further structure. The structure functions will only depend on the likelihood to find a parton carrying the fraction x of the proton's momentum [3]. If a structure function has no dependence on Q^2, it is said to "scale" with Q^2 ("Bjorken scaling"):

$$F_i(x, Q^2) \longrightarrow F_i(x) \tag{1.10}$$

In the QPM, partons are spin 1/2 quarks, which only couple with the transversely polarized bosons, thus the cross sections for longitudinally polarized bosons will vanish [2], resulting in the relation:

$$F_L = 0 \Rightarrow F_2(x) = 2xF_1(x) \tag{1.11}$$

The naive Quark Parton Model is quite successful in kinematic regions where the effects of gluons can be neglected. However, the presence of gluons modifies the proton structure, causing the structure functions to depend on Q^2, so-called "scaling violation".

The structure function F_2 has been studied in great detail by the ZEUS and H1 experiments at HERA (Chapter 2) [4]. Figure 1.2 shows the kinematic reach

of those measurements as compared to the fixed target data measurement. The F_2 measurement exhibits Bjorken scaling at medium values of x, and scaling violation at very low and high values of x.

1.3.4 Proton Structure and Splitting Functions

QCD makes corrections to the proton structure in QPM. A quark in the proton can radiate a gluon before the interaction with the photon, thus acquiring transverse momentum. Therefore spin 1/2 quarks can also couple with longitudinally polarized photons, and Equation 1.11 no longer holds. The existence of gluons also leads to scaling violations. A "sea" of quark anti-quark pairs surrounds the quarks due to the continuous radiation and absorption of gluons by the quarks. An increase in Q^2 allows one to probe deeper into the sea, which is no longer a point-like structure. Considering only virtual photon exchange, the structure function F_2 is the sum of the momentum distributions of the quarks and anti-quarks weighted by the charge squared:

$$F_2(x, Q^2) = \sum_i e_i^2 [x q_i(x, Q^2) + x \bar{q}_i(x, Q^2)] \tag{1.12}$$

where the sum runs over quark and anti-quark flavors, e_i is the charge of a quark of flavor i and $q_i(x, Q^2)$ is the probability density of finding a quark of flavor i. A gluon can be radiated by a quark and a gluon can split into a gluon pair or a quark anti-quark pair. Gluon radiation and splitting result in a cascade of gluons and quarks within the proton. With respect to the QPM, this results in a modified proton structure consisting of the original valence quarks, gluons and sea quarks (a quark and anti-quark pair which was split into by a gluon), as illustrated in Fig. 1.3.

The lower the value of x, the more phase space available for gluon radiation,

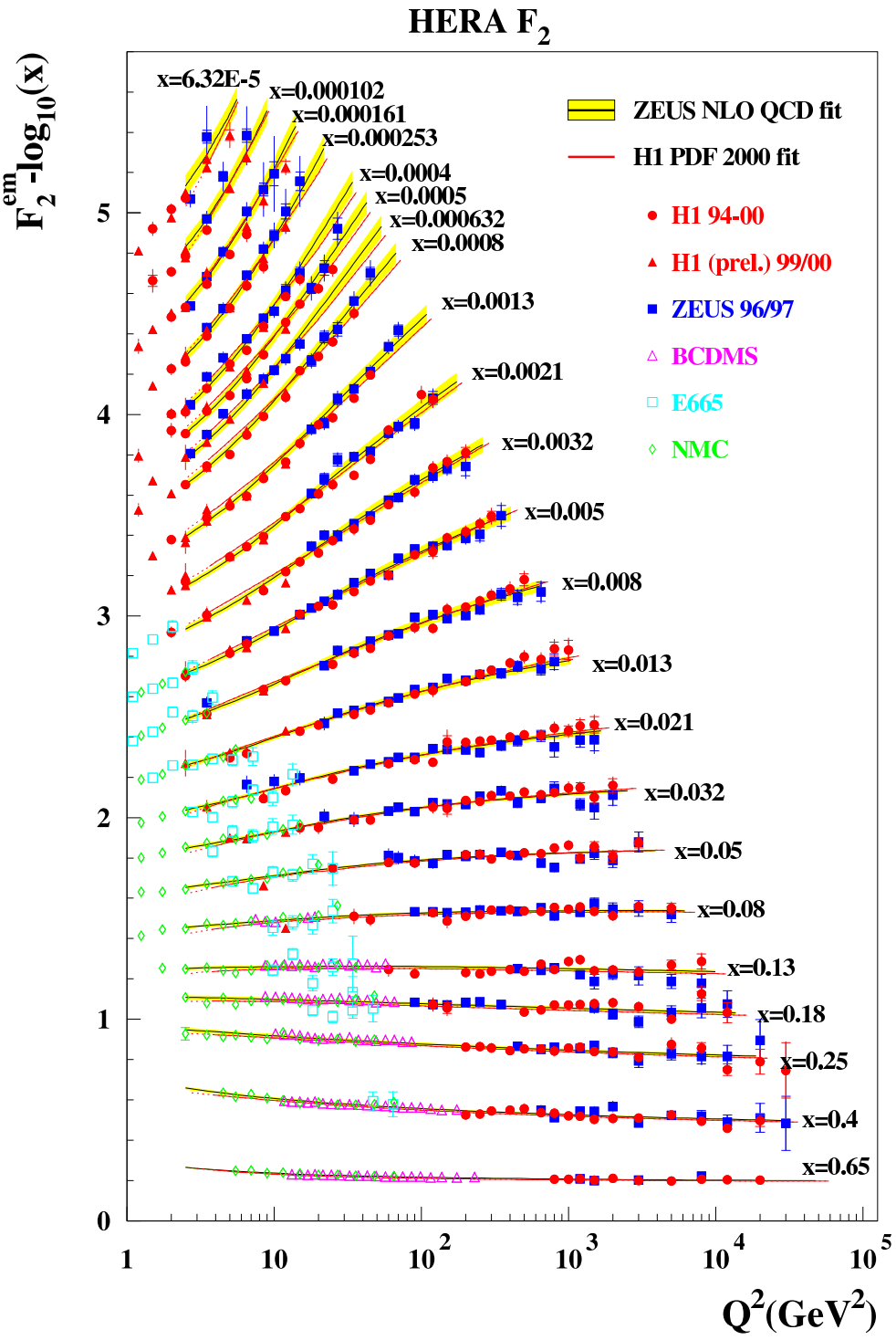

Figure 1.2: Measurements of the structure function F_2 by the HERA experiments ZEUS and H1, and fixed target experiments. The HERA data span the kinematic region $6 \cdot 10^{-5} < x < 0.65$ and $1\,\mathrm{GeV}^2 < Q^2 < 10^5\,\mathrm{GeV}^2$.

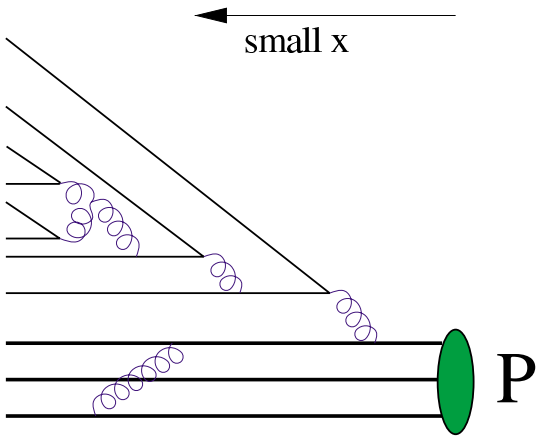

Figure 1.3: The structure of the proton in QCD at varying values of the kinematic variable Bjorken x.

which thereby increases the sea quark density as well. On the other hand, how much of this sea quark distribution can be revealed depends on the resolution of the scattering (Q^2). Due to this effect, QCD predicts the rise of F_2 with Q^2 at low x, which was observed in Fig. 1.2.

The probabilities of the splitting and radiation of the gluons (Figure 1.4) are characterized by splitting functions, which to first order in pQCD are [2]:

$$\begin{aligned} P^0_{qq}(z) &= \frac{4}{3}\left(\frac{1+z^2}{1-z}\right); \\ P^0_{gq}(z) &= \frac{4}{3}\left(\frac{1+(1-z)^2}{z}\right); \\ P^0_{qg}(z) &= \frac{1}{2}(z^2+(1-z)^2); \\ P^0_{gg}(z) &= 6\left(\frac{(1-z)}{z}+\frac{z}{1-z}+z(1-z)\right) \end{aligned} \tag{1.13}$$

These are the first-order probabilities of a parton j emitting a parton i with momentum fraction z of the parent parton.

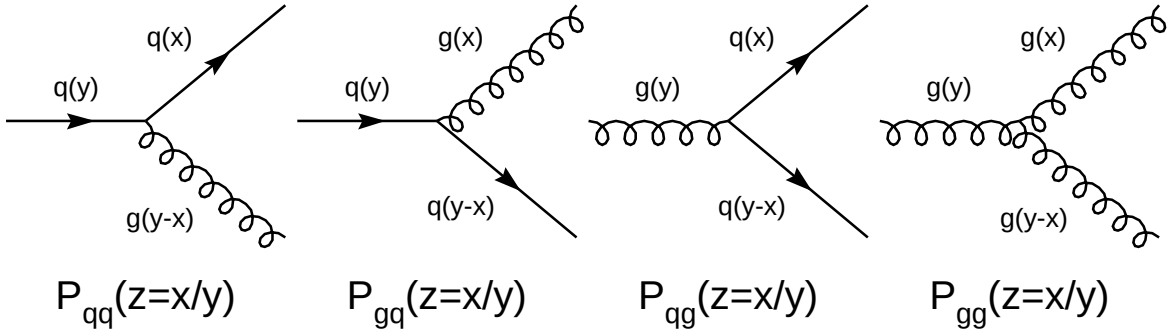

Figure 1.4: QCD Splitting Functions

1.3.5 Factorization and Parton Density Function

The QCD modified Quark Parton Model was shown to work very well in the perturbative region where the partons inside the proton are asymptotically free and where Q^2 is large. However, there are contributions to the cross section that come from long-range (soft) interactions where α_s is large, which are non-perturbative and non-calculable. This can be dealt with by using the concept of factorization. Similar to the renormalization scheme described in Sec. 1.2.3, a factorization scale μ_F is introduced, to separate the long-range (soft) and short-range (hard) processes.

The general form of DIS cross section is a convolution of the calculable partonic interactions and the parton distributions

$$d\sigma = \sum_{a=q,\bar{q},g} \int dx \; f_a(x, \mu_F^2) \; d\hat{\sigma}_a(x, \alpha_s(\mu_R), \mu_R^2, \mu_F^2). \tag{1.14}$$

where the sun runs over all parton flavors: gluon, quarks and anti-quarks. $f_a(x, \mu_F^2)$ is the parton density function (PDF): the probability of finding a parton of type a with proton momentum fraction x at scale μ_F^2. The factorization scale eliminates the divergencies in the partonic cross section by introducing a cutoff in the transverse momentum of the involved parton. If the transverse momentum of the parton is

below the value chosen for the factorization scale, it is absorbed into the PDF. If it is above the factorization scale, it is included in the calculation of the partonic cross section.Therefore the hard perturbative processes are separated ("factorized") from the non-perturbative processes implicitly included in the PDFs at the scale μ_F. The factorization scale, μ_F, is the scale at which the PDF is evaluated.

The newly factorized parton distribution function takes the general form

$$f(x,\mu_F^2) = f(x) + \frac{\alpha_s}{2\pi}\int_x^1 \frac{\mathrm{d}y}{y} q(y) f(P_{ij}^0, \mu_F) \tag{1.15}$$

where the P_{ij}^0 are the leading order QCD splitting functions given in the previous section including P_{qq}, P_{qg}, P_{gg} and P_{gq}. By differentiating Equation 1.15 with respect to the factorization scale μ_F, setting $\mu_F = Q$ and separating the pieces associated with quark radiation and gluon radiation, the following coupled equations are found:

$$\begin{aligned}
\frac{\mathrm{d}q_i(x,Q^2)}{\mathrm{d}\ln Q^2} &= \frac{\alpha_s(Q^2)}{2\pi}\int_x^1 \frac{\mathrm{d}y}{y}\Big(\sum_i q_i(y,Q^2)P_{qq}(\frac{x}{y}) + g(y,Q^2)P_{qg}(\frac{x}{y})\Big) \\
\frac{\mathrm{d}g(x,Q^2)}{\mathrm{d}\ln Q^2} &= \frac{\alpha_s(Q^2)}{2\pi}\int_x^1 \frac{\mathrm{d}y}{y}\Big(\sum_i g(y,Q^2)P_{gg}(\frac{x}{y}) + q_i(y,Q^2)P_{gq}(\frac{x}{y})\Big)
\end{aligned} \tag{1.16}$$

where now the full splitting function with its perturbative expansion in α_s is included. These are the DGLAP equations [5] which give the evolution of the PDFs. The specific values of the PDFs given in Equation 1.15 can not be predicted by QCD and must be determined from experiment. The primary source of input are measurements of the F_2 structure function in DIS experiments, which provide the initial quark distributions at a given x and Q^2.

To determine the parton density functions in practice, the input distributions are parameterized at first, then evolved in Q^2 using the DGLAP equations, and compared with the experimental data sets. Finally, the parameterizations are adjusted iteratively

until a best fit with the data sets is achieved [6]. Parton distributions at $Q^2 = 10\,\mathrm{GeV}^2$ from the ZEUS-S [7], MRST2001 [8] and CTEQ6M [9] PDFs are shown in Fig. 1.5. The ZEUS-S, MRST2001 and CTEQ6M sets of PDFs differ on the choice of experimental data sets and parameterizations of the input parton distributions.

1.4 Jet Physics in DIS

This analysis is interested in a certain class of DIS events in which a highly collimated stream of final-state particles, called a jet, is located in the detector. The partonic cross sections in DIS are shown in Eqn. 1.14. However, those final-state partons are not observable particles in the experimental, due to color confinement in QCD. These partons undergo showering and hadronization as described in Chapter 3. The observable quantities are groups of hadrons that originate from partons emitted in the hard interaction, i.e. jets. Therefore jet study is necessary in the comparison of data to theoretical predictions. Jets with a sufficient (transverse) energy originate from a parton emitted from the hard scattering process, while soft partonic radiations should form low energy jet or "merge" back to the jet they radiate from. To achieve an accurate mapping between jets and corresponding hard partons of the hard scattering process, a tool of jet algorithm is introduced, see Section 5.5.1.

1.4.1 Trijet Production in DIS

The differential partonic jet cross section in DIS, $d\sigma$, can be written in term of perturbative expansions in α_s:

$$d\sigma = A\alpha_s(\mu_R^2) + B\alpha_s^2(\mu_R^2) + C\alpha_s^3(\mu_R^2) + ... \tag{1.17}$$

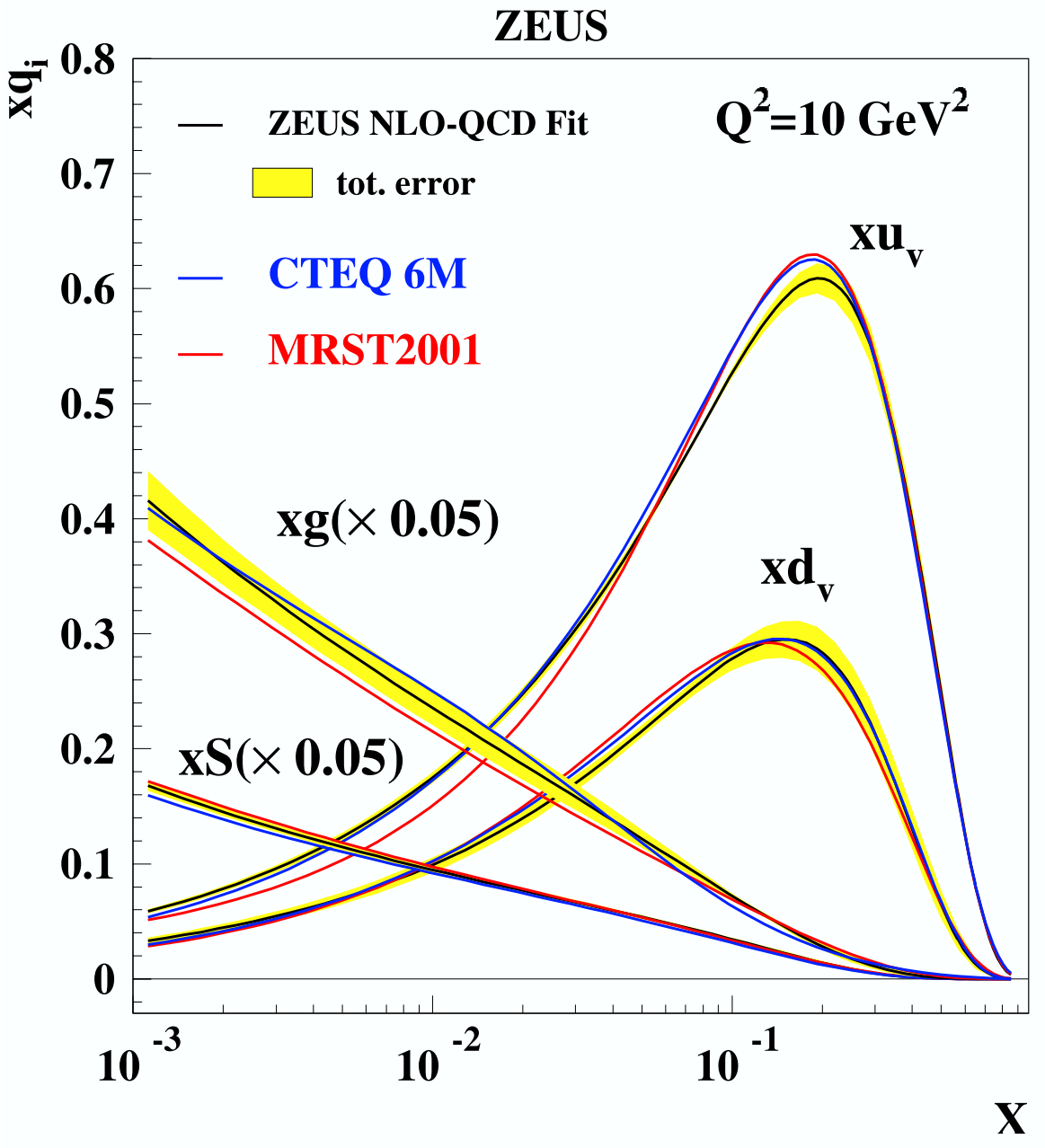

Figure 1.5: The proton parton momentum densities times x for the up valence quark (xu_v), down valence quark (xd_v), sea quarks (xS), and the gluon (xg). The gluon and sea quark distributions are divided by a factor of 20. The shaded band are the estimated errors from the ZEUS-S PDF set.

where A, B and C are coefficients. The first term of the expansion is commonly referred as leading order or first order (LO) and the second term as next-to-leading order or second order (NLO).

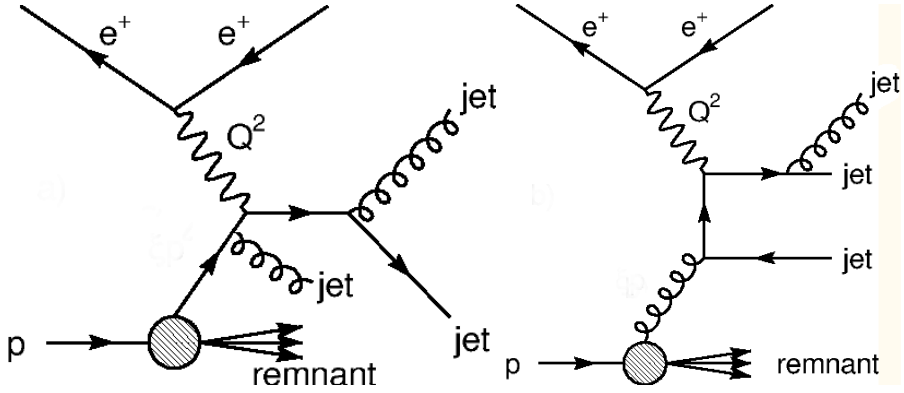

Figure 1.6: Diagrams of the QCD Compton process (left) and Boson-Gluon Fusion process (right) in trijet production in DIS.

At leading order (LO) in dijet production in neutral current DIS, Boson-Gluon Fusion (BGF, $V^*g \to q\bar{q}$ with $V = \gamma$, Z^0) and QCD Compton (QCDC, $V^*q \to qg$) processes are the only contributions to the first term in Eqn. 1.17. In the QCDC process a gluon is radiated in the initial or final state. In the BGF process, a gluon present in the proton and the exchanged photon participate in the hard scattering process and produce two quarks, observed as jets in the final state.

Trijet production can be seen as dijet processes with an additional gluon radiation (Figure 1.4.1) or splitting of a gluon into a quark-antiquark pair. It is directly sensitive to $\mathcal{O}(\alpha_s^2)$ QCD effects in LO. The higher sensitivity to α_s and the large number of degrees of freedom of the trijet final state allow a detailed and accurate quantitative test of QCD. In addition, the cross-section ratio of trijet to dijet pro-

duction is directly proportional to α_s at LO, resulting in a cancellation of correlated experimental and theoretical uncertainties, thus allowing a precise determination of α_s (Chapter 8).

Chapter 2

Experimental Setup

The data used in this analysis were collected during the 1998-2000 running period with the ZEUS detector at HERA, when HERA operated with protons of energy $E_p = 920\,\text{GeV}$ and electrons or positrons of energy $E_e = 27.5\,\text{GeV}$, and correspond to an integrated luminosity of $82.2 \pm 1.9\ \text{pb}^{-1}$.

2.1 HERA

The Hadron Elektron Ring Anlage (HERA) is the first and only electron-proton collider in the world. It is located at the Deutsches Electronen Synchrotron (DESY) laboratory in Hamburg, Germany, and has operated since 1992. Considered to be the "world's most powerful electron microscope", HERA allows deep inelastic scattering to be studied at much higher center-of-mass energy and in a much wider kinematic range than previous fixed-target experiments, see Figure 2.1.

Figure 2.2 shows a layout of the HERA facility and its pre-accelerator system. The proton acceleration chain starts with negative hydrogen ions (H^-) accelerated to 50 MeV. The electrons are extracted from the H^- ions to produce protons, which are injected into the proton synchrotron DESY III, accelerated up to 7.5 GeV, and

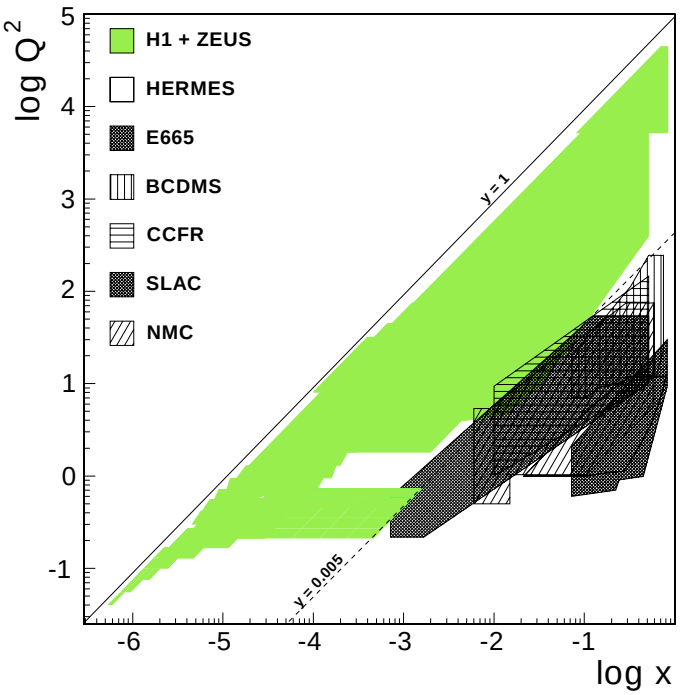

Figure 2.1: Kinematic available to the HERA collider experiments H1, ZEUS and several fixed-target experiments.

then transferred to PETRA, where they are accelerated to 40 GeV. Finally they are injected into the HERA proton storage ring, where they reach the nominal beam energy of 920 GeV. The electron[1] pre-acceleration chain starts in a linear accelerator, LINAC, where the electrons are accelerated up to 450 MeV. The electrons are then injected into DESY-II, accelerated to 7 GeV and then transferred to PETRA II, where they reach an energy of 14 GeV. They are then injected into HERA where they reach the nominal electron beam energy of 27.5 GeV.

Four experiments are located along the HERA ring, separated by 90 degree arcs. Electron-proton collisions occur in two interactions points, one in the North Hall where

[1]In the following, the term "electron" denotes generically both the electron (e^-) and the positron (e^+).

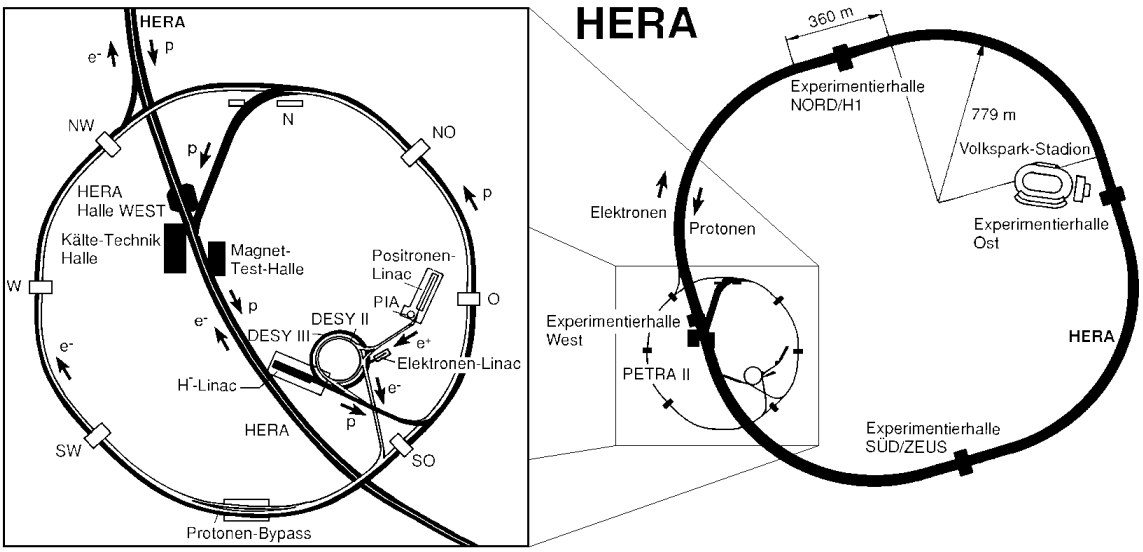

Figure 2.2: The HERA collider complex and associated experiments.

the H1 experiment is located, the other in the South Hall where the ZEUS experiment is placed. Two fixed-target experiments HERMES and HERA-B are located in the remaining two halls. In the East Hall, the HERMES experiment studies the spin structure of the nucleon using the collisions of polarized electrons on an internal polarized gas target. The HERA-B experiment, located in the West Hall, was designed to study CP violation in the B system using the proton beam on a wire target.

The HERA tunnel is 6.3 km long and it is located between 15 and 30 meters below the ground level electrons and protons are accelerated in two different rings. The beam line of the electron ring consists of conventional magnets with maximum field of 0.165 T, while the proton beam is made of superconducting magnets with a maximum field of 4.65 T. HERA can be filled with a maximum of 210 bunches of each electrons and protons spaced by 96 ns. Some of these bunches are kept empty (so-

called "pilot bunches") in order to study the background conditions. When either the electron or the proton bunch is empty, the beam-related background, originating from the interaction of the electron or the proton beam with the residual gas in the beam pipe, can be studied, whereas when both bunches are empty the non-beam-related background can be estimated, such as the rates of cosmic rays.

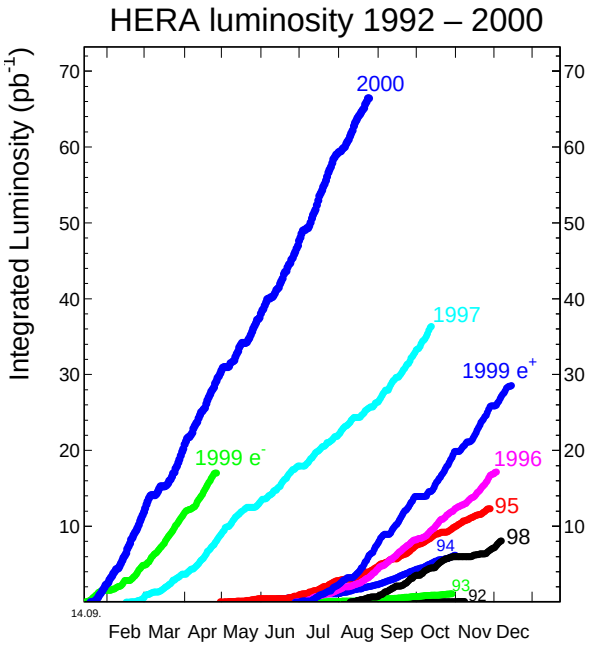

Figure 2.3: Integrated luminosity delivered by HERA for each year of running.

The luminosity delivered by HERA run I period is shown in Figure 2.3. The running operations began in 1992 with an electron beam, but in 1994 it was realized that the electron beam current was limited by positively ionized dust particles getting in the beam pipe through the pumps, reducing the lifetime of the beam. For this reason HERA switched to positrons in July 1994, achieving a more stable beam and a significant increase in the integrated luminosity of the collected data. During the 1997-98 shutdown period, new pumps were installed to improve the electron beam

lifetime and the proton beam energy was raised from 820 to 920 GeV. During 1998 and part of 1999 HERA was running with electrons, afterward it switched back to run with positions.

2.2 ZEUS

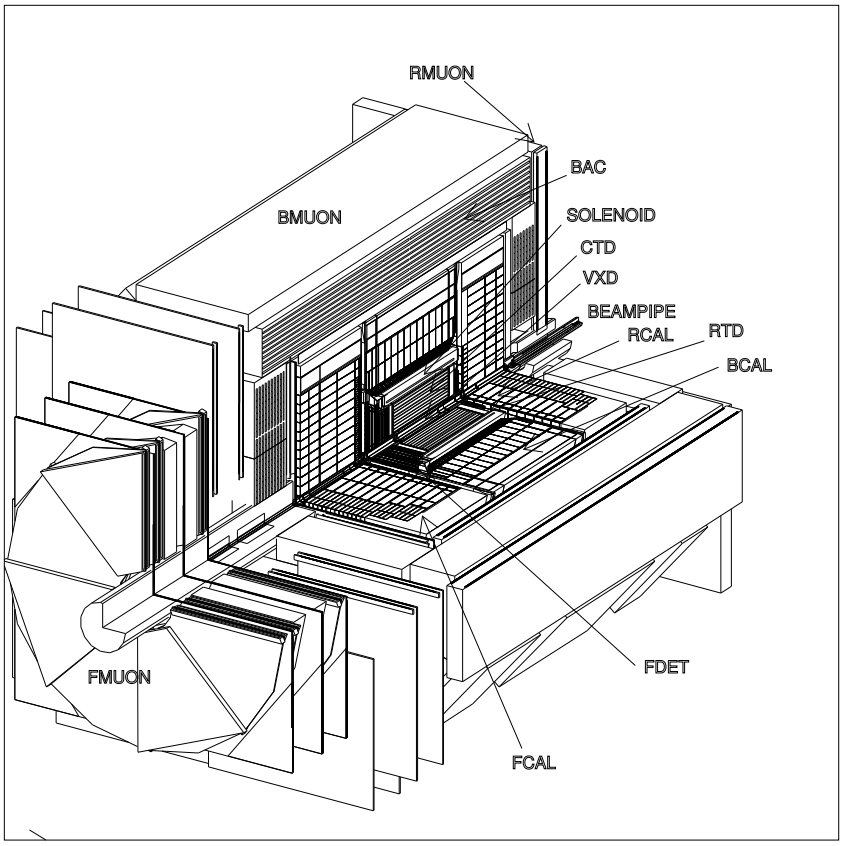

Figure 2.4: A 3D view of the ZEUS detector.

The ZEUS detector is a multipurpose detector designed to study electron-proton scattering at HERA. It is a quasi-hermetic detector since it covers most (99.7%) of the solid angle around the collision point, except small regions around the beam pipe. The layout of the ZEUS detector is given in Fig. 2.4. ZEUS uses a right-handed

CAL Section	Angular coverage	EMC	HAC
FCAL	$2.5° - 39.9°$	20×5 cm^2	20×20 cm^2
BCAL	$36.7° - 129.2°$	20×5 cm^2	20×20 cm^2
RCAL	$128.1° - 178.4°$	20×10 cm^2	20×20 cm^2

Table 2.1: FCAL, BCAL and RCAL parameters.

coordinate system with the nominal interaction point at the origin. The z-axis points in the proton beam direction, referred to as the "forward direction" and the x-axis points toward the center of the HERA ring. The polar angle, θ is defined with respect to the positive z-axis and the azimuthal angle ϕ is defined with respect to the x-axis. Reference to the polar angle is often made with its Lorentz invariant counterpart, η, defined as $\eta = -\ln\tan\frac{\theta}{2}$. The large difference in the electron and proton beam energies causes the final-state particles to be boosted in the proton beam direction, thus the forward direction of the detector is deeper than the rear region.

A detailed description of the ZEUS detector can be found elsewhere [10]. A brief outline of the components that are most relevant for this analysis is given below.

2.2.1 The Uranium-scintillator Calorimeter

The ZEUS calorimeter (CAL) [11] is a high-resolution uranium-scintillator calorimeter surrounding completely the tracking devices and the solenoid. It measures the energy and position of the final-state particles and is used for scattered electron identification and hadronic final state reconstruction.

The CAL is divided into 3 sections: a forward calorimeter (FCAL), a barrel calorimeter (BCAL) that encloses the Center Tracking Detector and a rear calorimeter (RCAL), see Figure 2.5 and Table 2.1. Each section is subdivided into *modules*,

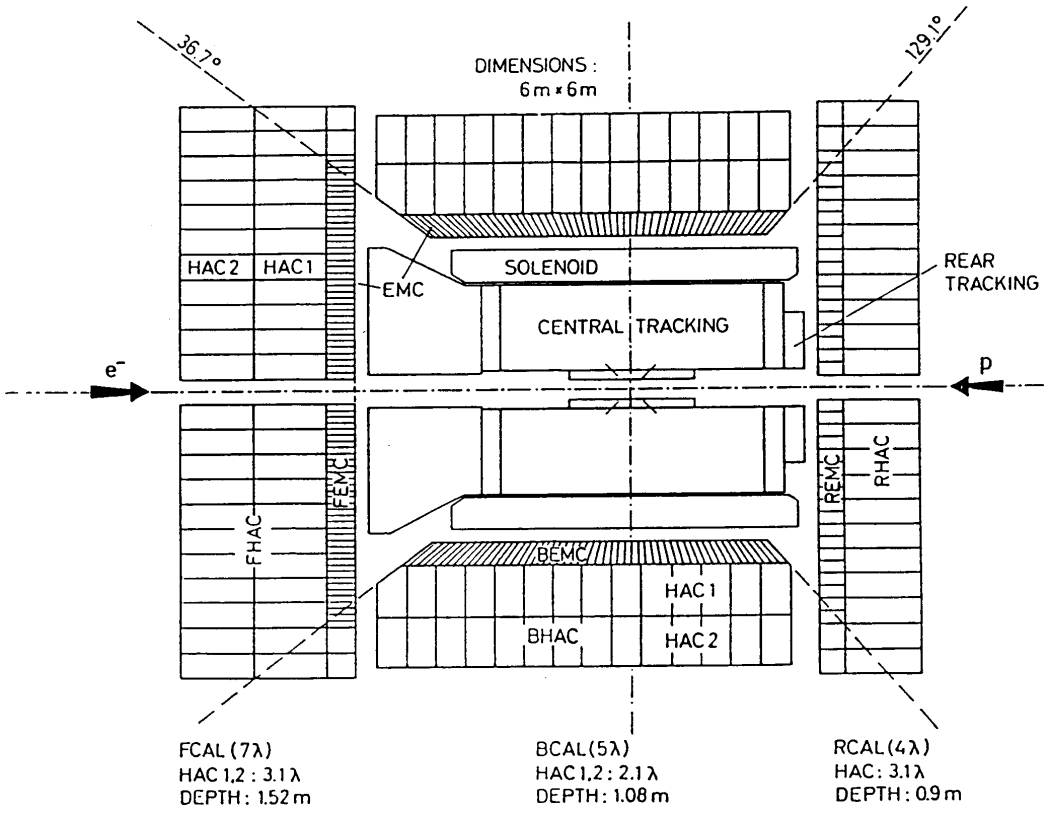

Figure 2.5: A $x - y$ side view of the ZEUS Calorimeter.

with those in FCAL/RCAL (BCAL) oriented along the y-axis z-axis) with faces perpendicular (parallel) to the axis. Modules are segmented into *towers* with a front surface dimensions of $20 \times 20\,\text{cm}$. FCAL/RCAL towers are rectangular, while BCAL towers are wedge shaped and projective in η. Each tower is subdivided longitudinally into one inner electromagnetic section (EMC) and either one hadronic section (HAC) as in RCAL, or two hadronic sections (HAC1, HAC2) as in FCAL/BCAL. A typical BCAL tower is depicted in Fig. 2.6. The longitudinal length of each EMC section is typically 25 radiation lengths, where one radiation length (X_O) corresponds to the thickness of material which reduces the mean energy of a electron by a factor of e. A typical HAC section is longitudinally two nuclear interaction lengths thick, where one

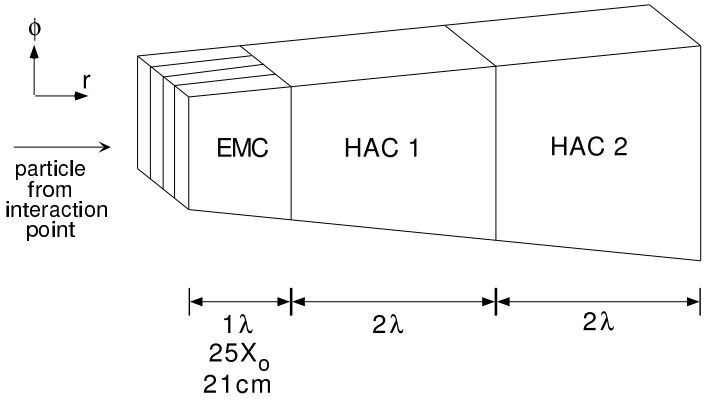

Figure 2.6: The structure of a BCAL tower.

interaction length (λ) is the mean distance traveled before a nuclear interacts with the material. One HAC section consist of one *cell*, and one EMC section consists of four cells. Each cell consists of alternating plates of absorber (3.3 mm-thick depleted uranium) and active material (2.6 mm-thick plastic scintillator).

Particles entering each cell produce showers of particles which create ultra-violet light in the scintillator The light is read by 2 mm thick wavelength shifter bars on both sides of the module, and brought to photomultiplier tubes (PMT) where it is converted into an electrical signal. All cells are read out by two (right and left) PMTs simultaneously for a more accurate position measurement and redundancy. Also by checking PMTs from both sides, one reduces the hardware noise generated by PMT and its infrastructure. The PMT pulses are used for energy and time measurement.

One complexity in measuring a particle's energy with the calorimeter comes from the fact that the signal response of hadrons and electrons is different. The response from hadronic particles is typically less than that from electromagnetic particles because they lose some of their energy in nuclear processes that don't result in a measurable signal. Because the hadronic shower usually has an electromagnetic com-

ponent as well, the hadronic measurement is much more difficult to make . One can develop complex correction schemes to deal with this problem or make the calorimeter "compensating". The CAL achieves equal response to electrons and hadrons by using depleted uranium as an absorber which gives additional signal from fission of slow neutrons, and by tuning the ratio of absorber to scintillator width (3.3 mm of absorber for every 2.6 mm of scintillator). The achieved electromagnetic resolution is $\sigma(E)/E = 18\%/\sqrt{E}$, while the hadronic resolution is $\sigma(E)/E = 35\%/\sqrt{E}$, where E is the particle energy, measured in GeV. The CAL also provides accurate timing information, with a resolution of the order of 1 ns for particles releasing an energy deposit greater than 1 GeV.

2.2.2 Central Tracking Detector

The Central Tracking Detector (CTD) [12] is a cylindrical wire drift chamber along the z-axis used to measure the direction and momentum of the charged particles, and the position of the event vertex. The CTD is also used to identify the scattered electron in DIS events.

The CTD has inner radius 16.2 cm, outer radius 85.0 cm, and length 241 cm, corresponding to an angular coverage of $15°<\theta<164°$. It is operated within a 1.4 T magnetic field and filled with a gas mixture of argon, carbon dioxide, and ethane. It consists of 72 radial layers of sense wires, divided in groups of eight into nine superlayers (SL) with the associated field wires. One octant of the CTD is shown in Fig. 2.7. When charged particles enter the CTD, they ionize the gas. The electrons from the ionization drift toward the positive sense wires, whereas the positively charged ions drift toward the negative field wires. The trail of ions produced by the traversing

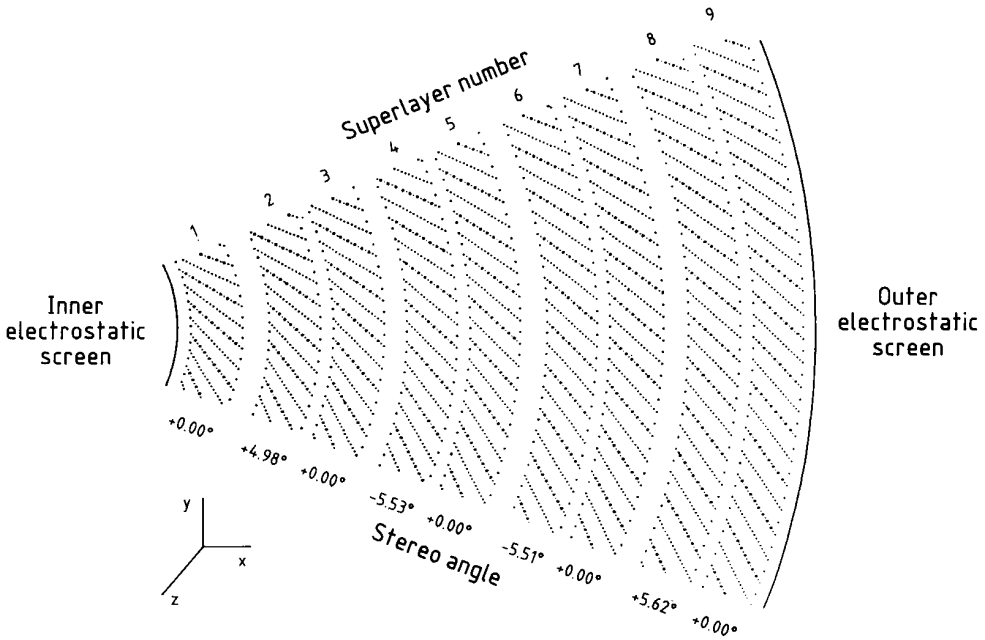

Figure 2.7: Diagram of one octant of the CTD.

particle create a series of hits which are then reconstructed as tracks. *Goodtracks* are defined as tracks in which 3 superlayers are used to reconstruct the trajectory of the particle.

The odd-numbered superlayers have wires parallel to the z-axis (*axial wires*), while the even-numbered superlayer wires are inclined at angles around $\pm 5^\circ$ with respect to the z-axis (*stereo wires*) in order to measure the z-position more accurately. The achieved resolution is $\sim 200\,\mu$m in the $r-\phi$ plane and $\sim 4\,\mu$m in the $z-$ position. The curvature of tracks in the magnetic field serves to measure their transverse momentum. The resolution on the transverse momentum, p_T, for good tracks and with p_T>150 MeV, is given by: $\sigma(p_T)/p_T = \sqrt{(0.0058 \cdot p_T)^2 + 0.0065^2 + (0.0014/p_T)^2}$, where the first term is the hit position resolution, the second and the third depend on the multiple scattering inside and before the volume of the chamber, respectively.

The three inner superlayers are equipped with a z-by-timing system which uses the axial wires to make a fast determination of the event vertex z-position [12]. This is used in the trigger selection (Section 6.1.2).

2.2.3 Luminosity Monitor

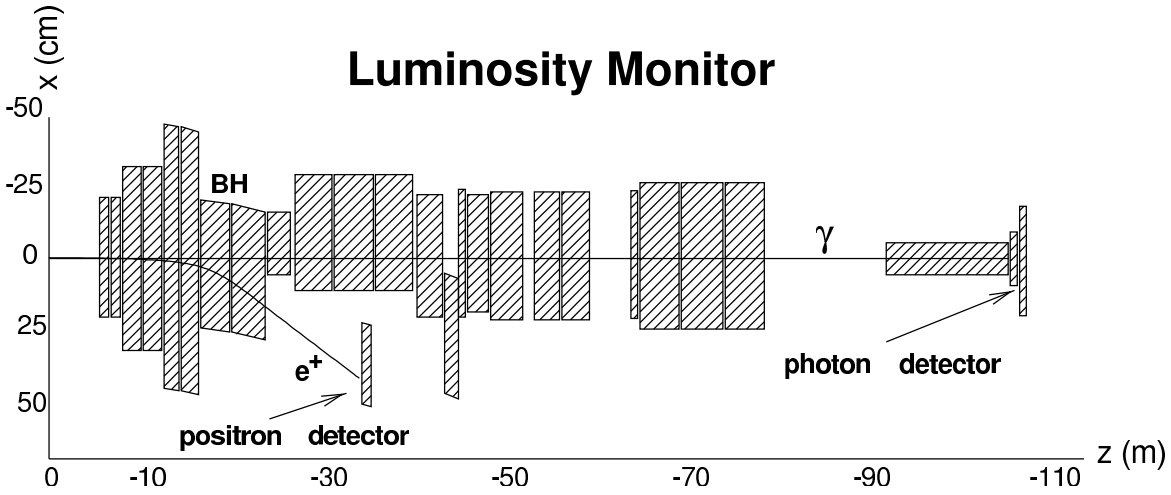

Figure 2.8: The layout of the ZEUS luminosity monitor system. The nominal interaction point is located at (0,0).

A precise measurement of the integrated luminosity is necessary in order to obtain the correct absolute normalization of all measured cross section (Section 7.1) The luminosity measurement at ZEUS is done by studying the bremsstrahlung events $ep \to ep\gamma$, where the electron and the photon are scattered at very small angle. The cross section (σ_B) for this process at fixed photon scattering angle, θ_γ, and energy, E_γ, is well known. The cross section and a measurement of the photon rate (N_γ) for photons in the same range of θ_γ and E_γ can be used to obtain the luminosity: $\mathcal{L} = N_\gamma/\sigma_B$. The theoretical prediction for the process is known with an accuracy of $\sim 0.5\%$, allowing a precise determination of the luminosity.

N_γ is measured by the Luminosity Monitor System, see Figure 2.8. It consists of a photon and a electron calorimeter, located along the beam line at $z = -107\,\mathrm{m}$ and $z = -35\,\mathrm{m}$, respectively. To protect the photon calorimeter against synchrotron radiation, it was shielded by a carbon-lead filter. The photon and electron calorimeter resolutions are $\sigma(E)/E = 23\%/\sqrt{E}$ and $\sigma(E)/E = 18\%/\sqrt{E}$ respectively, with E in GeV. The bremsstrahlung event rate is determined by counting the number of photons above a fixed energy threshold, and not by the simultaneous identification of the electron and the photon, because of the dependence of the electron calorimeter acceptance on the beam position and angle. Events with coincident energy deposits in the photon and electron detectors are used to calibrate the energy scale of the photon calorimeter since the scattered electron and photon energies sum to the initial electron energy.

The main contribution to the background is given by the bremsstrahlung of electrons on the residual gas in the beam pipe. This can be estimated using pilot bunches, i.e. electron bunches with no associated proton bunches. The achieved precision on the luminosity measurement during the 1998-2000 running period for this analysis is 2.25%.

2.2.4 Scattered Electron Measurements

The measurement and identification of the scattered electron is essential in any NC DIS analysis. Considerable efforts are taken to achieve an accurate measurement of the scattered electron's position and energy using detectors in addition to the calorimeter and tracking detector. The Hadron-Electron Separator (HES) [13] and Small angle Rear Tracking Detector (SRTD) [14] are used to make a precise position

measurement, while the Rear Presampler (RPRES) [15] together with SRTD is used to correct for energy loss in front of the calorimeter.

2.2.4.1 HES

The HES is an array of 3×3 cm silicon diodes located at a depth of three radiation lengths into the EMC section of the Forward and Rear calorimeters. Since it has much finer granularity than the main calorimeter, the HES information is used to correct the position of the electron measured by the main calorimeter.

2.2.4.2 RPRES and SRTD

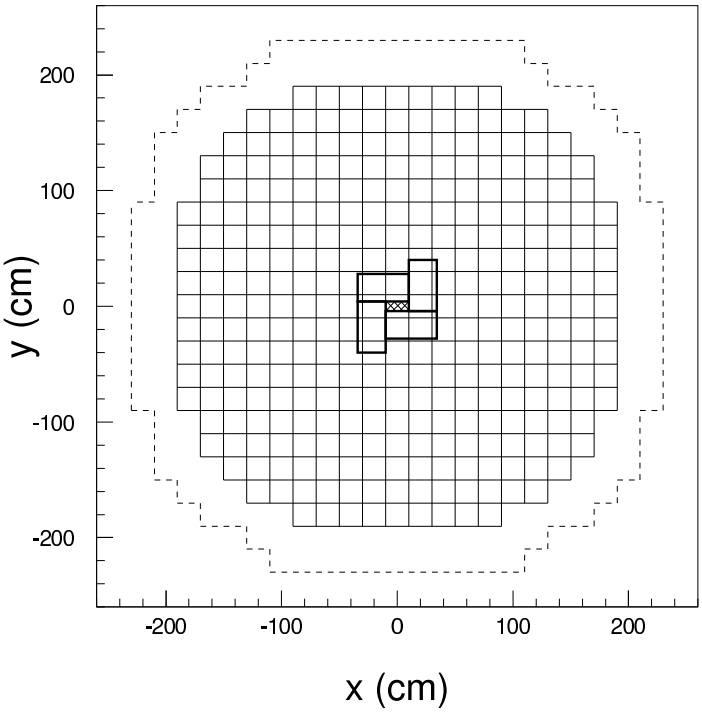

Figure 2.9: The layout of the Rear Presampler tiles (boxes) and the Small angle Rear Tracking Detector (thick lines) with respect to the RCAL boundary (dashed line).

Before particles reach the calorimeter they pass through *dead material* (inactive material that is not designed to sample the energy absorbed). A non-exhaustive

list of types of dead material includes: the beam-pipe, the solenoid magnet, support structures, cooling systems, cables, and on-detector electronics. In particular as the scattered electron interacts with dead material, it produces a shower of charged particles (positrons and electrons) and photons, which ionize atoms in the material. This results in a loss of energy with respect to the original positron that is proportional to the number of particles produced in the shower.

In order to determine the energy loss, two pre-shower detectors RPRES and SRTD, were placed in front of RCAL to count the number of minimum ionizing particles (MIPS) incident on the face of RCAL. The layout of RPRES and SRTD with respect to the RCAL boundary are shown in Fig. 2.9.

The Rear Presampler consists of 20×20 cm scintillator tiles placed directly in front of RCAL and has a combined angular coverage of approximately $128° < \theta < 176°$. The Small angle Rear Tracking Detector is a scintillator strip detector located on the front face of RCAL. The SRTD consists of four sections with dimensions of 24×44 cm surrounding the beam pipe hole in RCAL, as shown in Fig. 2.9, and has a maximum angular coverage of approximately $150° < \theta < 178°$. Each section consists of two $x - y$-oriented planes of 1 cm-wide scintillator strips. The strips in one plane are orthogonal to the strips in the other plane.

A particle passing through the SRTD deposits energy in both planes, allowing the impact position to be reconstructed with a resolution in $x - y$-plane of approximately 2.9 mm. The SRTD is particularly useful for correcting low-Q^2 DIS electrons, where the electron scatters at small angles. The energy measured by the calorimeter is scaled up by a factor proportional to the number of MIPS measured in either the SRTD or

RPRES to correct for the energy loss due to the dead material.

2.2.5 The Veto Wall and C5 Counter

The Veto Wall is an iron wall covered with scintillator on both sides and has dimensions of $8 \times 7.6 \times 0.86\,\mathrm{m}$ with square holes of 0.95 m to accommodate the beam pipe and magnets. It is located at $z = -7\,\mathrm{m}$, shielding the detector from upstream proton beam halo particles and providing a timing signal used to reject upstream beam-gas interactions. The C5 collimator is located directly behind RCAL at $z = 3.15\,\mathrm{m}$ surrounding the beam pipe. Attached scintillator counters provide timing information used to synchronize the HERA and ZEUS clocks and reject off-time beam-gas interactions.

The background rejection using the Veto Wall and C5 counter timing information is described in Sec. 6.1.1.

2.2.6 Trigger System

The high bunch crossing rate (96 ns crossing time corresponds to a rate of 10.4 MHz), together with the high background rate of 30 kHz, and the wide variety of interesting physics processes require a sophisticated, state-of-the-art *online* trigger. ZEUS has a three-level trigger system [10, 16] as shown in Fig. 2.10. The task of each level is to reduce the input rate such that its output rate is below the rate required for the next level. As the input rates for each trigger level decrease, the complexity of the decisions and the data they are based on increase. In addition to the 3 online trigger levels, further data selection is achieved *offline* as the data are reconstructed.

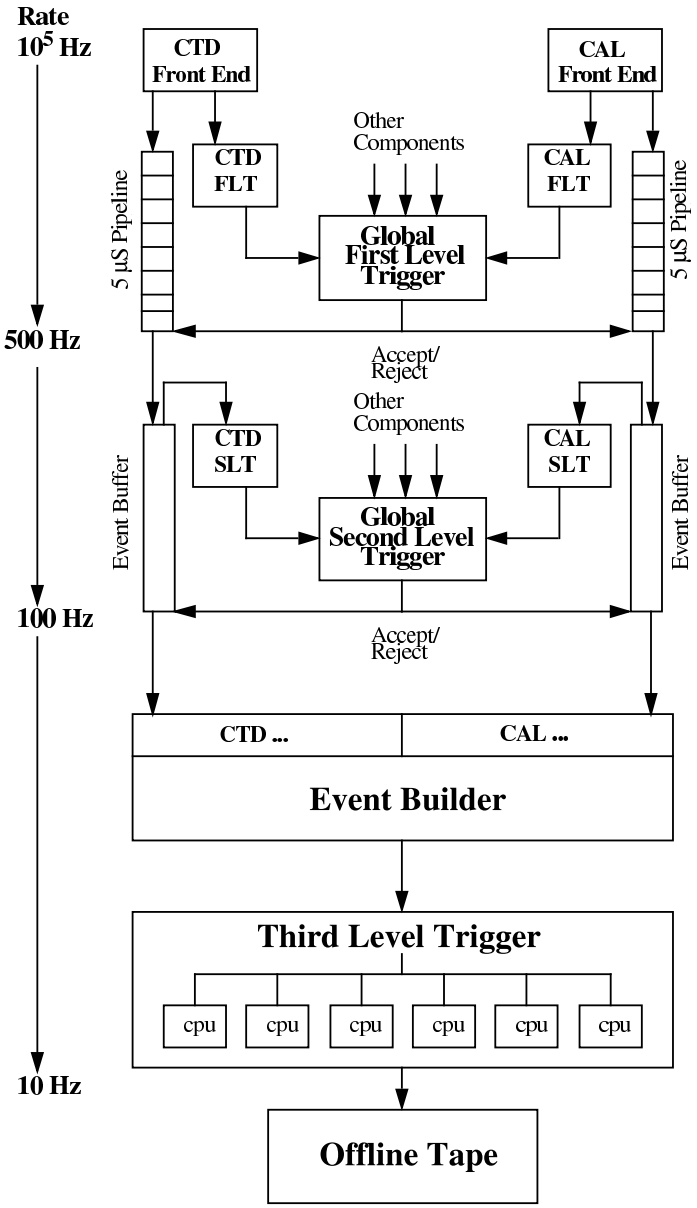

Figure 2.10: Diagram of the ZEUS trigger and data acquisition system

2.2.6.1 First Level Trigger

The whole First Level Trigger (FLT) system is pipelined for 5 μs, to avoid deadtime, since the time it takes to collect, make and transmit a trigger decision, 4.4 μs, is much greater than the 96 ns interval between bunch crossings. The ZEUS FLT relies mainly on the Calorimeter First Level Trigger (CFLT) [17] and the CTD First Level Trigger (CTD FLT) [18]. The FLT has access to only a limited amount of component data, such as simple energy sums, number of isolated electrons, number of isolated muons, times from the veto components, and number of CTD tracks, in order to make a trigger decision within every bunch crossing interval. The CFLT takes 5% of the Calorimeter signal from every PMT, shapes and digitizes the analog signal, and computes global calorimeter sums such as total transverse energy and missing p_T. It also performs some primitive electron finding. The Global First level trigger (GFLT) receives and examines the coarse FLT information from all components and makes the final decision whether to accept or reject the event. The decision is returned to the detector components exactly 46 bunch crossings ($\sim 4.4\,\mu$s) after the event occurred. The whole process is completely deadtimeless.

There is additional processing of calorimeter trigger data by the Fast Clear system between GFLT accepts. The Fast Clear aborts events before processing by the Second Level Trigger (SLT). The GFLT, including the Fast Clear, brings the event rate below 1 kHz, a typical rate is between 200 and 300 Hz.

2.2.6.2 Second Level Trigger

In case of a GFLT accept, the complete component data for an event is passed to the component's Second Level Trigger (SLT) where it is stored in memory buffers.

The SLT processor functions as an asynchronous pipeline, i.e. a series of parallel processors. The SLT software is executed on a network of transputers [19]. Component SLTs analyze the data and send processed information on to the Global Second Level Trigger (GSLT). At this level, most of data has already been digitized. Due to the longer time available ($\sim$ 7 ns), the larger amount of information available, and the flexibility of the GSLT architecture, more complicated and detailed calculations can be done. The SLT reduces the event rate further to below 100 Hz, typically around 35 Hz. Upon a GSLT accept, data are sent to the Event Builder (EVB). EVB collects and puts it in the standard ZEUS format before sending it to the Third Level Trigger (TLT).

2.2.6.3 Third Level Trigger

In contrast to the first two trigger levels, the TLT has no local trigger systems. The TLT is software based and runs a slightly reduced version of the offline reconstruction code on a processor farm built from commodity computers. The full event information is available to the TLT and the available processing time is significantly longer ($\sim$ 300 ns) than previous levels. At the TLT complicated algorithms are run to search for specific types of physics events required by different physics analysis groups. The TLT accept rate is typically near 10 Hz. Accepted events are written to mass storage (tape) for later processing.

2.2.6.4 Offline Reconstruction

At a later time, the data selected by the trigger system are passed through the reconstruction software package which contains the reconstruction code of different

components. This $offline$ reconstruction is nearly identical for both data and Monte Carlo events, see Section 3.6. The reconstruction program calculates quantities more usable for physics analyses and processes the data into a Data Summary Tape (DST) format, which allows for fast access for a specific type of physics event.

Chapter 3

Monte Carlo Simulations

3.1 Introduction

Monte Carlo (MC) simulations are based on the theory of underlying physical process and their phenomenological models. In this case (neutral current deep inelastic ep scattering), all the possible leading order (LO) Feynman diagrams for the hard interaction between an electron and a proton are generated according to their possibilities, where the possibilities are taken from the integral of the relevant LO matrix element. The parameters that define the kinematics and types of particles participating in a MC generated event are assigned according to a random sampling of known probability distributions. In this way, the kinematic behavior of the accumulated events is consistent with that of the probability distribution. If the underlying theoretical and phenomenological structure is correct, the MC generated sample should match the observed sample within the statistical precision.

MC techniques are essential in this analysis:

- to compare experimental results with theoretical predictions, see Section 7.2.2;

- to correct data for the detector effects so the measured inclusive jet production cross sections are *independent* of the experiment apparatus (the ZEUS detector in this case), see Chapter 7 and 8;

- to generate hadronization (Section 3.4) correction factors needed to compare the measured cross sections to higher-order pQCD calculations, see Section 7.5.

- to correct data for QED radiative effects (Section 3.5) in order to compare the measured cross sections to higher-order pQCD calculations, see Section 7.4.

In this analysis, two Monte Carlo generators, LEPTO 6.5 program [20] and ARIADNE 4.08 program [21], are used to generate DIS events to leading order in pQCD (LO MCs).

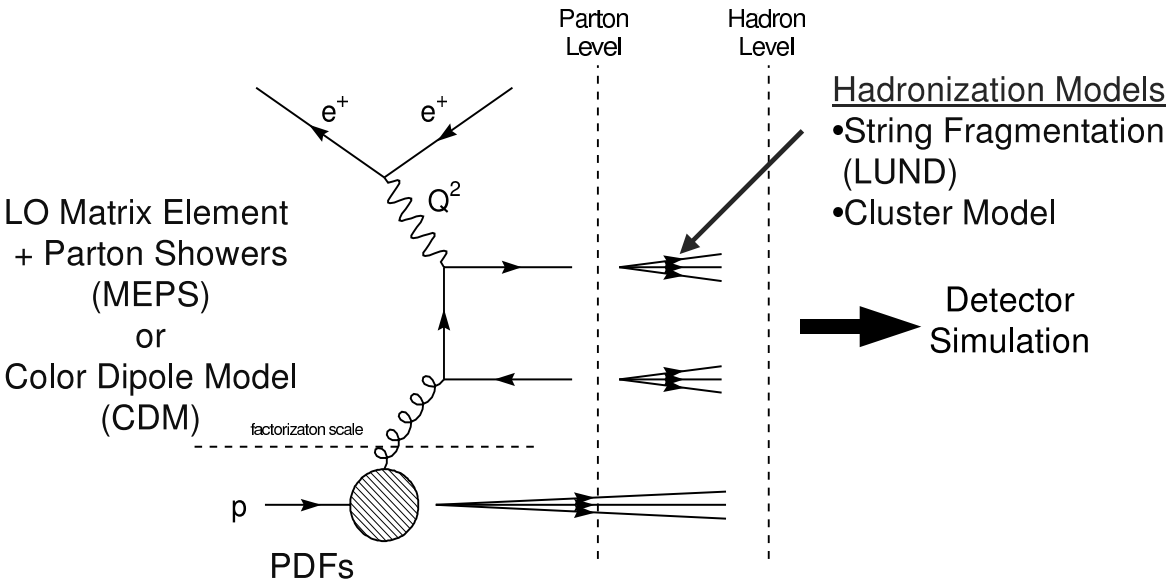

Figure 3.1: The hard scattering process, parton cascade, hadronization and detector simulation phase of a Monte Carlo generated Boson-Gluon Fusion event.

There are generally four stages of evolution for a MC generated event (Figure 3.1). The hard scattering process is calculated according to the Feynman rules,

the final state partons emitted from the hard scattering produce a parton cascade and the proton remnant evolves according to phenomenological models. The particles resulting from the parton cascade are grouped into stable hadrons. In this analysis, the *parton level* is considered to be after the parton cascade, and the *hadron level* is considered to be after hadronization stage where all particles present are stable hadrons. The output of the Monte Carlo simulation is a list of all particles that participated in the event during one or more of its phases, from the initial colliding particles and exchange boson, to the final hadrons. The list of final state particles is then propagated through a detector simulation program which simulates the response of the detector components to individual particles.

3.2 Hard Scattering and PDF

As described in Sec. 1.3.5, the amplitude for an ep scattering process can be factorized into a calculable convolution of partonic interaction that describes the hard scattering process and a non-perturbative PDF term. The hard scattering processes are generated by different models in MC based on LO matrix element. The PDF is an input to the Monte Carlo simulations. The factorization scale is the scale at which the parton density functions are evaluated. In this analysis, the CTEQ4D PDF [22] is used in the generation of DIS events by all MC programs.

3.3 Parton Cascade

The parton cascade stage is not only important as a connection between the analytically calculable hard scattering process and the hadronic final states, but it is also as a model for higher-order QCD effects, which are very difficult and time-consuming

to calculate. These higher order effects are particularly important in describing multijet events which arise from multiple parton emissions.

There are several models for parton cascade. The LEPTO program uses the matrix element plus parton shower model (MEPS) [23] and the ARIADNE program uses the color dipole model [24].

3.3.1 Matrix Element plus Parton Shower Model

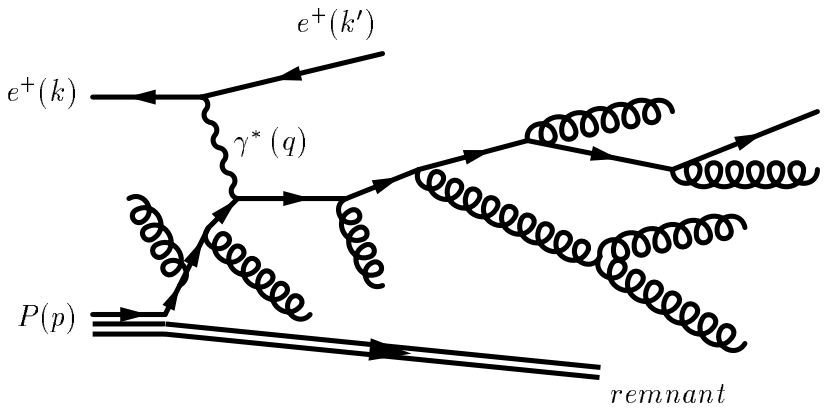

Figure 3.2: Matrix element plus parton shower (MEPS) model for parton cascade as implemented in LEPTO program.

In DIS, QCD radiation can occur both before and after the hard interaction, as shown in Fig. 3.3.1. Parton showers are controlled by looking at the virtuality of the partons, separating between on-shell ($m^2 \approx 0$) partons and off-shell partons which are either space-like ($m^2 < 0$) or time-like ($m^2 > 0$). A parton close to or on-shell in the proton can initiate a parton cascade where in each branching one parton becomes increasingly off-shell with a space-like virtuality and the other is on-shell with a time-like virtuality) From this space-like shower, a space-like quark is generated which participates in the hard interaction with the exchange boson. The

interaction with the boson turns the outgoing quark into one with either a time-like virtuality or one that is on-shell. In the former case, the shower continues, which each branching producing decreasingly off-shell masses until all the partons are on-shell.

In the MEPS model [23], these two showers (before and after the hard interaction) are treated differently, although they are both based on splitting functions as described by the DGLAP equations. The initial- and final-state radiation are combined with the matrix element calculation, but interference terms between initial and final state radiation are not included. This approach also does not treat QCD emissions from the proton remnant.

3.3.2 Color Dipole Model

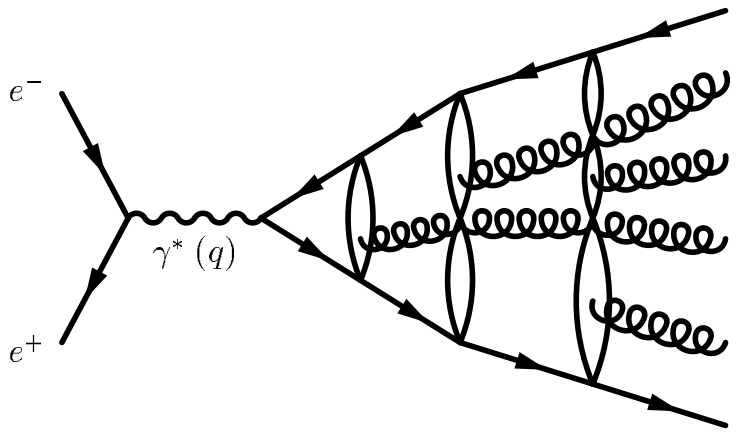

Figure 3.3: Color dipole model for parton cascade as implemented in ARIADNE program.

The color dipole model [24] is inspired by classical dipole radiation. The struck quark and the remnant carry color and anti-color charge. and can be interpreted as a color dipole. Instead of modeling an initial- and final-state radiation process independently, all radiation is assumed to occur between the color dipole formed between

the struck quark and the proton remnant. The radiation process can be thought of as modified e^+e^- scattering, with one of the quarks from the hard interaction substituted with the proton remnant (Figure 3.3.2). In the simplified scenario, a color dipole forms between the $q\bar{q}$ from the hard interaction, which induces a gluon emission. The emitted gluon itself carries color and anti-color. Softer gluon emission can be treated as radiation from two independent dipoles, one between the quark and gluon, the other between the gluon and antiquark. The parton cascade is treated as a formation of color dipoles, each of which may produce one or more softer emissions. This approximation would be adequate if in DIS, as with e^+e^-, the initial color dipole had point-like constituents. However, the proton remnant is an extended object. Modifications are made to allow only a fraction of the proton remnant's momentum to take part in an emission, thus reducing the available phase space as compared with e^+e^-.

Boson-Gluon Fusion(BGF) process does not occur in e^+e^- scattering. In order to include BGF process in the model, a matching procedure is needed in the first emission. In the procedure, the initial dipole between the struck quark and the hadron remnant can either emit a gluon according to the LO matrix element (as usual) or "emit" the anti-partner of the struck quark according to the BGF matrix element. In the latter case, two color dipoles are created which continue to radiate independently according to the model.

3.4 Hadronization

At the end of the parton cascade process, the MEPS and color dipole model produces an event consisting of a shower of colored partons (quarks and gluons) which can never be observed as free particles. What can be observed and measured are hadrons:

color-singlet bound states of confined quarks and gluons. The process that accounts for the conversion of final-state partons into final-state hadrons, called *hadronization*, cannot be described by perturbative calculations. Phenomenological hadronization models are introduced in order to produce stable final-state hadrons from input partons.

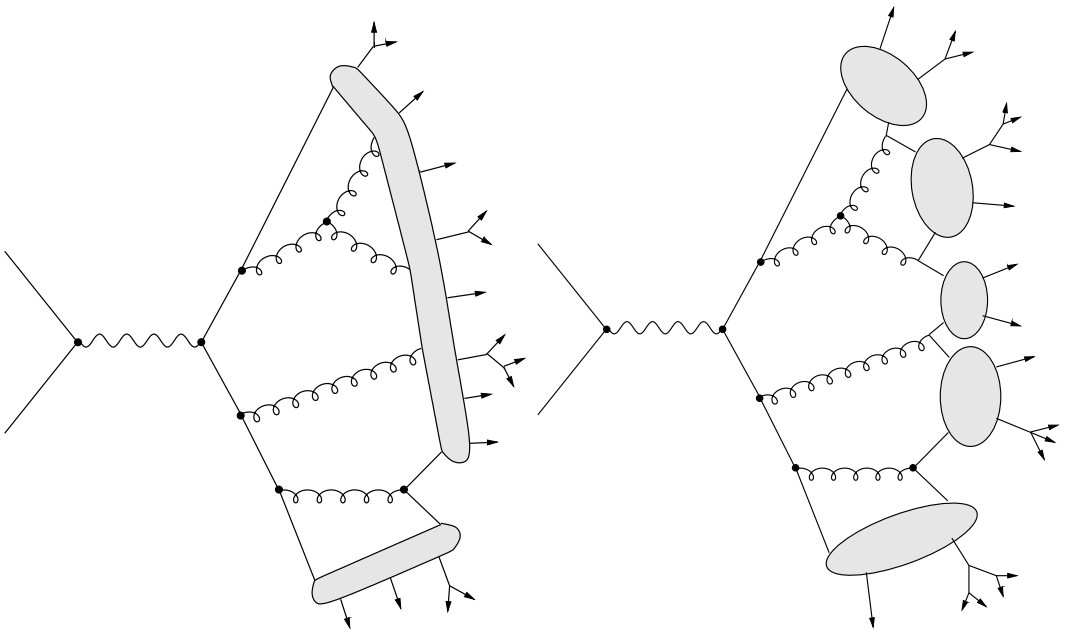

Figure 3.4: Hadronization scheme according to the Lund String Model (left) and Cluster Model (right). The strings and clusters are represented in the shaded regions of each drawing, and the outgoing arrows represent hadrons.

Two hadronization models are commonly used by the MC generators for DIS, see Figure 3.4. The Lund String Model [25] is used by the LEPTO and ARIADNE program as implemented in JETSET 7.4 [26, 27] and the Cluster Model [28] is used by the HERWIG program.

3.4.1 Lund String Model

In the Lund String Model [25], the hadronization process occurs through the formation of color strings and the fragmentation of those strings into hadrons. A given pair of quarks $q\bar{q}$ move away from each other effectively stretching out the "string" that represents the force of the color connection. The farther away the two partons move from each other, the greater potential energy stored in the string, until the string breaks due to the creation of a new $q\bar{q}$ pair in the color field. The two strings formed in the process continue to evolve independently, and the process continues until the invariant mass of a given string is below a specific threshold. Hadrons are formed from the colorless, stable objects spanned by the string below the mass threshold. The string structure gets more complicated as gluons and sea quarks are introduced to the model, those details can be found in [25].

3.4.2 Cluster Model

The cluster model [28] begins by splitting gluons non-perturbatively into $q\bar{q}$ or $qq\bar{q}\bar{q}$ pairs. Neighboring quarks and antiquarks are then grouped into color-singlet objects (clusters). These clusters are then split into hadrons, according to their mass. A cluster too light to form two hadrons becomes the lightest hadron of the appropriate flavor, by shifting its mass by exchanging momentum with neighboring clusters. The flavor of the hadrons is determined by the density of states available.

The strength of this model is its emphasis on the perturbatively calculable parts of the simulation, minimizing the number of model dependencies used to generate predictions. It assumes any observable quantity will be dominated by the perturbative part of the calculation and therefore has very few tunable parameters. The HERWIG

program uses the cluster model. However, HERWIG MC gives a poorer description of the hadronic final state in this analysis compared to LEPTO and ARIADNE, so it isn't the preferred Monte Carlo for modeling the detector or hadronization effects.

3.5 QED Effects

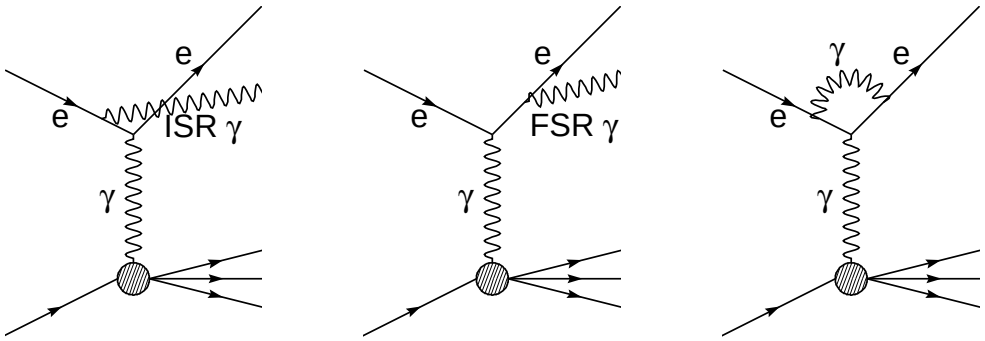

Figure 3.5: Diagrams illustrating QED radiation in the initial state (ISR), the final state (FSR) and as a virtual loop.

The stand-alone MC generators by default do not include the effects of QED radiation. Figure 3.5 shows the first order photon radiation diagrams. In the case of initial state (ISR) and final state QED radiation (FSR), the event kinematics can be significantly affected. In order to take these effects into account, the MC programs are interfaced to HERACLES 4.5.2 [29] via DJANGO 6.2.4 [30]. The HERACLES program includes QED effects up to $\mathcal{O}(\alpha_{\rm EM}^2)$.

3.6 Detector Simulation

The final state particles of each generated MC event are processed through a simulation program of the entire ZEUS detector, which is based on GEANT 3.13 [31]. The GEANT program includes the response of the detector components and the interaction

of particles in dead material. The generated events were passed through the detector simulation, subjected to the same trigger requirements as the data, and processed by the same reconstruction and offline programs. The output of the MC generators, after the detector simulation, is referred to in this analysis as the *detector level* MC. The detector level MC sample is in the same format as the actual ZEUS data sample and a direct comparison can be made. The comparison results are shown in Section 7.2.2.

3.7 Monte Carlo Simulations Summary

Neutral current DIS events were generated using the ARIADNE 4.08 program [21] and the LEPTO 6.5 program [20] interfaced to HERACLES 4.5.2 [29] via DJANGO 6.2.4 [30].

Measured distributions of kinematic variables are well described by both the ARIADNE and LEPTO MC models after reweighting in Q^2 (Section 7.2.1). The LEPTO simulation gives a better overall description of the $E_{T,B}^{\text{jet}}$ and invariant mass distributions. Therefore, the events generated with the LEPTO program were used to determine the acceptance corrections. The events generated with ARIADNE were used to estimate the systematic uncertainty associated with the treatment of the parton cascade as described in Sec. 8.5.

Chapter 4

NLO Calculations

NLO calculations in this chapter refer to a class of programs which calculate partonic jet cross sections in deep inelastic scattering to second-order (next-to-leading order, NLO) in the strong coupling constant, α_s. In these programs, QCD matrix elements are calculated exactly to second order without phenomenological models, one order higher than the LO Monte Carlo programs (Chapter 3). The NLO calculations provide the most accurate predictions of the jet cross sections.

4.1 Introduction

The differential cross section for inclusive trijet production in deep inelastic scattering at NLO in pQCD is given by (Section 1.3.5):

$$d\sigma = \sum_{a=q,\bar{q},g} \int dx \; f_a(x,\mu_F^2) \; d\hat{\sigma}_a(x,\alpha_s(\mu_R),\mu_R^2,\mu_F^2). \tag{4.1}$$

The partonic cross section for the inclusive trijet cross section, $d\hat{\sigma}$, has contributions from four-parton final states and from virtual loop corrections to three-parton states (Figure 4.1). However, such contributions lead to divergent terms in the calculation. The four-parton states contributions are positive and diverge as the energy of the

radiated gluon (real emission) approaches zero ("soft") or as the angle of the radiated gluon respect to the parent parton approaches zero ("collinear"), the so-called infrared divergency. The virtual-loop contributions are negative and diverge as the four-momentum of the virtual gluon loop (virtual emission) is integrated to infinity, the so-called ultraviolet divergency. A finite cross section is obtained by factorizing (at a scale μ_F, see Section 1.3.5) divergencies from initial state radiation into the parton density functions (PDFs) and by cancelling the remainder of the (positive) soft and collinear contributions with the (negative) virtual-loop contributions.

The NLO programs mainly use two different methods to cancel these divergencies: the phase splicing method [32] and the subtraction method [33].

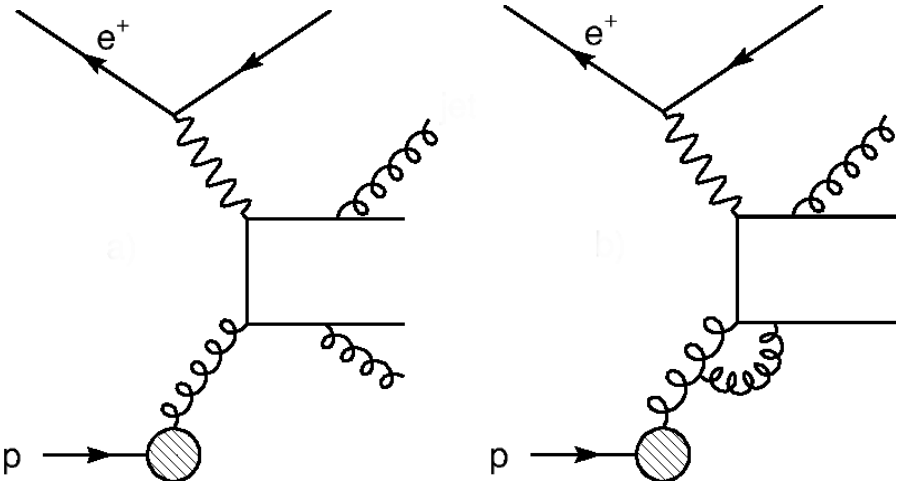

Figure 4.1: Examples of four-parton final state (left) and virtual loop (right) diagrams that contribute to the inclusive trijet cross section at NLO.

4.2 PDF Uncertainty

The parton density functions (Section 1.3.5) are convoluted with the partonic final state to calculate pQCD NLO calculations. Therefore PDF uncertainty contributes

to the overall (theoretical) uncertainty of the NLO calculations.

PDF uncertainty is introduced from the experimental data used to extract the PDF, from the differences in theoretical parameterization assumptions, and from the approximations made in the fit procedure. To estimate the full uncertainty of the PDF, one must first obtain certain PDF sets which are specially calculated to include all possible uncertainties (so-called "PDF uncertainty sets"), e.g. for CTEQ6 PDF [9], there are 40 additional sets available. The PDF uncertainty for any physical observable can then be estimated by repeating the NLO calculation with the variations in these sets (Section 8.5).

4.3 Scale Dependence and Uncertainty

Renormalisation scale is the scale at which the running coupling constant $\alpha_s(\mu_R^2)$ is evaluated (Section 1.2.3). For an all-order calculation (infinite perturbative expansion in α_s), the predicted trijet cross section would be independent of the renormalisation scale, μ_R. However, fixed-order calculations have a dependence on the μ_R, resulting in an uncertainty in the predicted trijet cross section.

The value of the renormalisation scale in principle is arbitrary and is typically chosen to be Q^2 or E_T for calculations of the inclusive jet cross sections in DIS. In this analysis, it is chosen to be $(\bar{E}_T^2 + Q^2)/4$, where for dijets (trijets) $\bar{E}_T$ is the average E_T of the two (three) highest E_T jets in a given event. The factorization scale, μ_F, can also have different choices of its value and is typically set to have the same value as μ_R.

To estimate the uncertainty due to the choice of the renormalisation and factorization scale, μ_R and μ_F were varied simultaneously by a conventional factor of 2

and the variation of the resulting cross section was measured. The magnitude of the variation in the cross section indicated the size of the contributions from higher order perturbative processes. The uncertainty associated with the choice of renormalization scale is the largest contribution to the theoretical error for jet analyses in DIS. Other contributions, including the factorization scale uncertainty and PDF uncertainty, are several times smaller, see Section 8.5.

4.4 Asymmetric Jet Cut and Invariant Mass Cut

The divergency cancellation methods used in the NLO programs guarantee the exact cancellation of ultraviolet and infrared divergencies. However, they are sensitive to certain classes of constraints placed on the phase space available to the final state partons. A typical problem is treating two classes of contributions unequally. For dijet production in the Breit frame, the two final state partons of the virtual loop contribution have equivalent jet transverse energy $E_{T,B}^{\text{jet}}$ (a feature of the Breit frame, see Section 5.5.2), while in case of the three-parton final state, due to the (real) emission of a soft gluon, the transverse energy of one of the jets is reduced, i.e. the two hard jets have unbalanced jet transverse energy. Therefore, the application of a symmetric jet cut (requiring the same minimum transverse energy for both first and second jet of dijet events) excludes the contribution from the three-parton final state near the cut boundary while the contribution from the virtual loop contribution remains. Due to the fact that virtual loop contribution is negative, the calculated NLO partonic cross section is reduced. This unphysical behavior in the NLO calculated cross section near the symmetric jet cut boundary was already shown in the dijet analysis [34].

For trijet production, symmetric jet cut is rather safe since trijet events have different jet transverse energy for each jet in the Breit frame. However, it is necessary to solve this issue when measuring the cross-section ratio of trijet to dijet production.

There are two solutions available:

- Make an asymmetric jet cut, e.g. $E_{T,B}^{\mathrm{jet},1}>8\,\mathrm{GeV}$ and $E_{T,B}^{\mathrm{jet},2}>5\,\mathrm{GeV}$, which provides sufficient phase space for soft gluon radiation.

- Make a cut on the invariant mass of the dijet system. Unlike the previous solution which only provides additional phase space for the first jet, this requirement provides additional phase space for both jets. By setting a minimum invariant mass of the dijet system, e.g. $M_{2\mathrm{jet}}>25\,\mathrm{GeV}$, one depopulates all the low energetic jet configurations, ensuring both jets are far beyond the jet transverse energy cut boundary ($E_{T,B}^{\mathrm{jet}1,2}>5\,\mathrm{GeV}$).

In order to measure the cross-section ratio correctly, the same cut must be applied to both dijet and trijet sample. The invariant mass cut is preferred because the requirement on the invariant mass $M_{3\mathrm{jet}}$ ($M_{3\mathrm{jet}}>25\,\mathrm{GeV}$) does not deplete the statistics of trijet events as much as the asymmetric jet cut.

4.5 NLOJET Program and DISENT Program

In this analysis, NLOJET program [35] is chosen to provide NLO predictions for comparison with the measured dijet and trijet cross sections in Chapter 8. NLOJET is the first NLO program which allows a computation of the trijet production cross sections to next-to-leading order, i.e. including all terms up to $\mathcal{O}(\alpha_s^3)$. DISENT [36] is used to check the NLOJET dijet results. Both programs use the subtraction method

in cancelling the divergencies.

4.5.1 Subtraction Method for Divergency Cancellations

The subtraction method [33] adds and subtracts a local counter term, $d\hat{\sigma}^{local}$, to make the real and virtual emission cross sections separately integrable. This local counter term is included in the full NLO cross section as follows:

$$d\hat{\sigma}^{NLO} = \int_{m+1} [d\hat{\sigma}^{real} - d\hat{\sigma}^{local}] + \int_{m} d\hat{\sigma}^{virtual} + \int_{m+1} d\hat{\sigma}^{local}$$
$$d\hat{\sigma}^{NLO} = \int_{m+1} [d\hat{\sigma}^{real} - d\hat{\sigma}^{local}] + \int_{m} [d\hat{\sigma}^{virtual} + \int_{1} d\hat{\sigma}^{local}] \quad (4.2)$$

where m is the number of partons in final states, in this case, $m = 3$. $d\hat{\sigma}^{local}$ is a proper approximation of $d\hat{\sigma}^{real}$ such as to have the same divergent behavior as $d\hat{\sigma}^{real}$ itself (in both soft and collinear limits). This allows the first integral on the right side of Equation 4.2 to be integrated numerically in four dimensions. Additionally, $d\hat{\sigma}^{local}$ must be analytically integrable over the one-parton phase space where the virtual-loop divergencies present. The terms associated with this integral can then be combined with those in the first integral, yielding a finite sum for the all terms in Equation 4.2. Combining all pieces, one can determine a finite result for the NLO partonic cross section.

4.5.2 Comparison of NLOJET and DISENT Program

It was checked that the LO and NLO calculations from NLOJET agree with those of DISENT at the 1-2% level for the dijet cross sections, see Figure 4.2. Notice the different implementation of $\alpha_{\rm EM}$ in two programs: for DISENT program, $\alpha_{\rm EM}$ is always fixed to be 1/137; for NLOJET program, $\alpha_{\rm EM}$ is either fixed to be 1/137 or varying as a function of Q^2 (vacuum polarization). Good agreement is observed only if both

programs use a fixed $\alpha_{\rm EM}$.

4.6 NLO Calculations Summary

The NLO predictions in this analysis were carried out in the $\overline{\rm MS}$ scheme for five massless quark flavors with the program NLOJET [35] using CTEQ6 [9], CTEQ4 [22], MRST99 [37] and ZEUS-S [7] for the proton parton density functions (PDFs). The hadron level selection cuts are applied on the NLO predictions in the same way as they are on the data and LO Monte Carlo samples. The NLO QCD predictions were corrected for hadronization effects using a bin-by-bin procedure obtained from LO MC, see Section 3.4 and Section 7.5.

For comparison with the data, the CTEQ6 PDF was used and the renormalisation and factorization scales were both chosen to be $(\bar{E}_T^2 + Q^2)/4$, see Chapter 8. The strong coupling constant was set to the CTEQ6 parameterization value, $\alpha_s(M_Z) = 0.1179$, and evolved according to the two-loop solution of the renormalisation group equation. For extraction of $\alpha_s(M_Z)$, the "A-series" of CTEQ4 PDF was used and the strong coupling constant was set to 0.110, 0.113, 0.116, 0.119, 0.122, respectively. The MRST99 and ZEUS-S PDF were used as a double-check in the determination of $\alpha_s(M_Z)$, see Section 8.4.

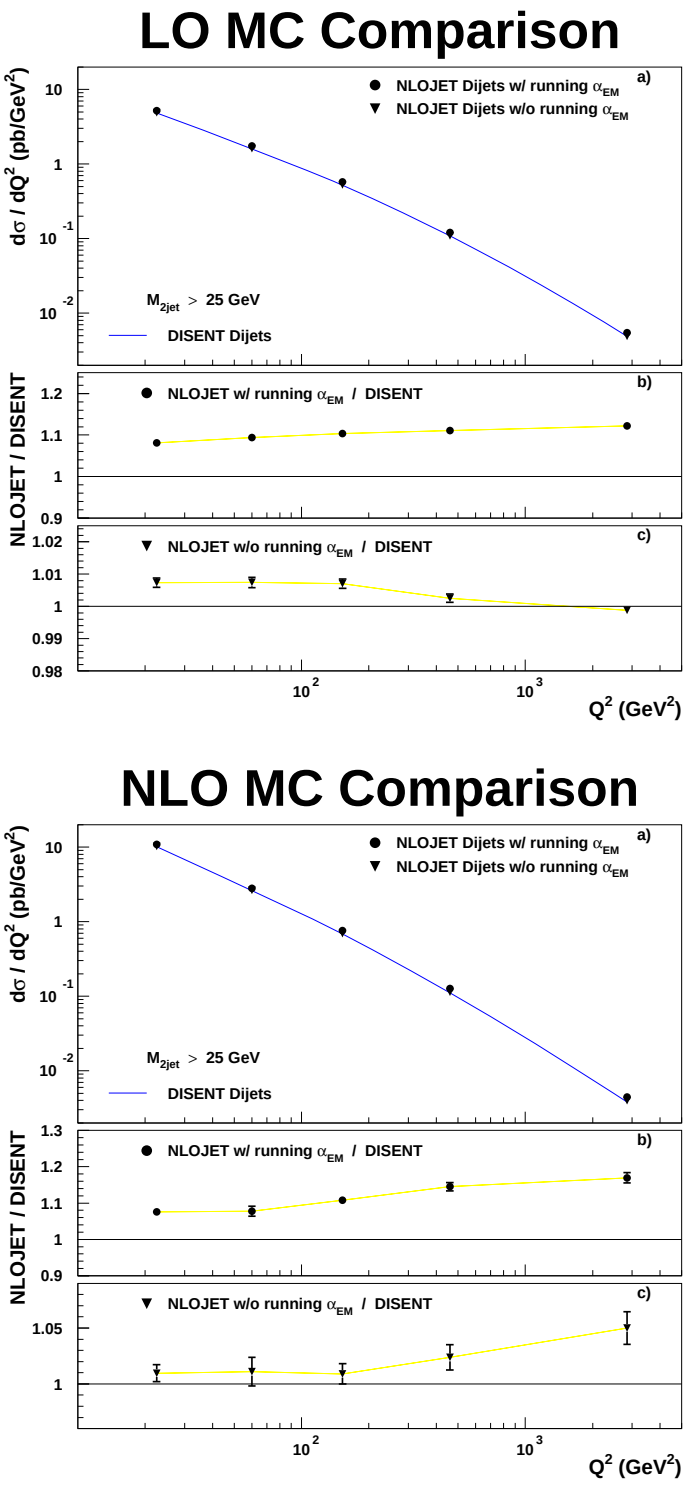

Figure 4.2: The LO and NLO comparisons of dijet cross section as functions of Q^2 for NLOJET and DISENT program.

Chapter 5

Event Reconstruction

The cross section measurement of this analysis is described in terms of the DIS kinematic variables x, y and Q^2, and the jet variables: jet transverse energy $E_{T,B}^{\text{jet}}$ and jet pseudorapidity $\eta_{\text{LAB}}^{\text{jet}}$. This chapter defines these variables, describes how they are reconstructed and verifies that the reconstruction is accurate and unbiased.

5.1 Track and Event Vertex Reconstruction

The event vertex is the collision point of the initial electron and proton and is the reference for all particle angles. The collision does not always happen at the nominal interaction point (0,0,0) in the ZEUS coordinate system. The determination of the event vertex is integrated into the track reconstruction procedure.

Charged particles create hits as they pass through the Central Tracking Detector (CTD) (Section 2.2.2). Tracks are found by starting with hits in the outermost axial superlayer, and then extrapolating toward the nominal vertex position, picking up hit information as the extrapolation spans the inner superlayers. The procedure continues for each axial superlayer in turn, excluding duplicate inner segments of previously found tracks, until all tracks that pass through the inmost superlayer are found. In

the final iteration, tracks that do not pass through the inmost superlayer, but contain information from at least two axial superlayers and one stereo superlayer are found.

All tracks passing through the inmost superlayer are included in a minimization fit procedure to determine the event vertex. Tracks can be assigned to a primary vertex (the interaction vertex) or a secondary vertex (a particle decay vertex). For these assigned tracks, their parameters are refitted using the event vertex as an additional constraint.

The vertex position is used in combination with the impact position on the calorimeter to get a precise measurement of the direction of the outgoing particles. The tracking information is used for the reconstruction of Energy Flow Objects and of the electron (see Section 5.2). It is also used for a number of cuts applied in the trigger logic and the offline analysis to improve the quality of reconstruction and to remove background events (see Chapter 6).

5.2 Calorimeter Cells and Energy Flow Objects (EFOs)

A precise jet measurement depends on a precise measurement of energy deposits. In order to improve the precision in the calorimeter measurement of energy deposits, "noisy" calorimeter cells (this noise typically comes from electrostatic discharge within the high voltage bases of the photomultiplier tubes) are removed and the calorimeter cells are recalibrated so that the energy response is the same in Monte Carlo simulation and data [34] (also see Section 5.5.3). However the tracking system has a much better angular resolution and a better energy resolution at low energies. Therefore an improved measurement of the energy deposits can be made by combining calorimeter and tracking information into Energy Flow Objects (EFOs). At ZEUS the EFOs are

also referred as “ZUFOs”. The EFOs are made massless by scaling the energy to match the momentum.

All calorimeter cells excluding those associated with the scattered electron and all *Good tracks* (Section 2.7) are used to build EFOs. First, calorimeter cells from the same shower are combined into one ’island’, then a match between tracks and islands is done. One EFO can have more than one track or island and is not required to have one track and one island at the same time. The assignment of position and energy to the EFO is based on the following procedure:

- If the tracking system has a better energy resolution than the calorimeter (e.g. at low energies), the tracking information is used. Otherwise the calorimeter information is used;

- If the calorimeter measures a much higher energy than the track, it is assumed that neutral particles hit at the same position as the charged particle. The calorimeter information is used;

- If a match consists of more than one island (track), the information from the islands (tracks) is first combined and then be used;

- If a track matches one or two islands, the positional information is taken from the tracking information;

- If a island matches more than three tracks, the calorimeter information is used.

- Unmatched tracks or islands are counted separately.

EFOs provide an improved overall resolution in $E^{\rm jet}_{T,B}$, $\eta^{\rm jet}_{\rm LAB}$ and also in the invariant mass of jet system.

5.3 Electron Reconstruction

The prime signature of neutral current DIS events is the scattered electron identified in the calorimeter. Electron candidates are identified using the neutral network program Sinistra95 [38]. As input it uses the longitudinal and transverse energy profiles of 'islands' of calorimeter cells. Islands within the CTD acceptance but without a track are not considered. The output is a probability between 0 (least probable) and 1 (most probable) for each island to be a electron. The neutral network was trained on large samples of neutral current DIS Monte Carlo events. Sinistra95 achieves both purities and efficiencies above 80% if the electron energy is greater than 10 GeV and the probability given by Sinistra95 is greater than 0.9.

The scattering (polar) angle and energy of the electron are used to kinematically reconstruct the event. The electron angle can be determined from a variety of sources. If there is an associated CTD track, the angle of the track at the event vertex gives the most accurate value of the electron angle. If the electron candidate lies in a region of the RCAL covered by the SRTD or HES, the positional information of these components can be used. If more than one source of position information is available, in that case, the more accurate one is used. The electron energy is first estimated as the sum of the energies of the calorimeter cells associated with the Sinistra95 candidate. It is then corrected for energy losses in the dead material in front of the calorimeter. Details of the correction methods are given in a previous dijet analysis [34].

5.4 Kinematic Reconstruction

The three Lorentz invariant quantities x, y and Q^2 are chosen to describe the kinematics of deep inelastic scattering events. An additional constraint imposed by the HERA fixed center-of-mass energy reduces the total number of independent kinematic variables to two: $s = \frac{Q^2}{xy}$.

Four measured quantities are available to reconstruct x, y and Q^2: the energy and polar angle of scattered electron, the energy $E - P_Z$ and polar angle of the hadronic system. Since only two are necessary, the pair that provides the most accurate reconstruction can be chosen. However, a single pair of measured quantities does not always provide the most accurate reconstruction over the entire kinematic range of interest in this analysis. Therefore, a specific reconstruction method is only used in the kinematic subregion in which it provides the best accuracy.

5.4.1 Electron Method (e)

The electron method [39] is used in this analysis to measure x and Q^2. It uses the corrected energy, E'_e, and polar angle, θ_e, of the scattered electron for the kinematic reconstruction ($E_{\mathrm{e,beam}}$ is the beam energy of the electrons, i.e. 27.5 GeV):

$$Q^2_e = 2E_{\mathrm{e,beam}}E'_e(1 + \cos\theta_e) \tag{5.1}$$

$$y_e = 1 - \frac{E'_e}{2E_{\mathrm{e,beam}}}(1 - \cos\theta_e) \tag{5.2}$$

5.4.2 Jaquet-Blondel Method (JB)

Independent from the electron method, the kinematic construction can be done using only the energy and polar angle of the hadronic system. The hadronic final state consists of many particles of which some belong to the remnant and escape through

the beam pipe. To avoid biases from the particles too close to the beam pipe, the transverse momentum of the hadronic system $P_{\mathrm{T,had}}$ and the difference between energy and longitudinal momentum $(E - P_z)_{\mathrm{had}}$ are considered. Both of these variables are close to zero for remnant particles going down the beam pipe. This method is called the Jaquet-Blondel method [40]:

$$y_{\mathrm{JB}} = \frac{1}{2E_{\mathrm{e,beam}}}(E - P_z)_{\mathrm{had}} = \frac{1}{2E_{\mathrm{e,beam}}}\sum(E_i - P_{z,i}) \tag{5.3}$$

$$Q^2_{\mathrm{JB}} = \frac{1}{1 - y_{\mathrm{JB}}}p^2_{\mathrm{T,had}} = \frac{1}{1 - y_{\mathrm{JB}}}\left[\left(\sum P_{x,i}\right)^2 + \left(\sum P_{y,i}\right)^2\right] \tag{5.4}$$

where the sum runs over all calorimeter cells except those belonging to the scattered electron.

The Jaquet-Blondel method gives an accurate determination of y for small values of y. In this analysis, y_{JB} is used exclusively to measure y.

5.4.3 Double Angle Method (DA)

The double angle method [41] is used in this analysis to measure x and Q^2 based on the polar angle of the scattered electron and the angle of the hadronic system (γ_{had}):

$$y_{\mathrm{DA}} = \frac{\sin\theta_e(1 - cos\gamma_{\mathrm{had}})}{\sin\gamma_{\mathrm{had}} + \sin\theta_e - \sin(\gamma_{\mathrm{had}} + \theta_e)} \tag{5.5}$$

$$Q^2_{\mathrm{DA}} = 4E^2_{\mathrm{e,beam}}\frac{\sin\gamma_{\mathrm{had}}(1 + \cos\theta_e)}{\sin\gamma_{\mathrm{had}} + \sin\theta_e - \sin(\gamma_{\mathrm{had}} + \theta_e)} \tag{5.6}$$

In the context of a quark parton model, the hadronic angle is the polar angle of the struck quark in the laboratory frame. In terms of the standard DIS quantities

and electron beam energy:

$$\cos\gamma_h = \frac{Q^2_{\rm JB}(1-y_{\rm JB}) - 4y^2_{\rm JB}E^2_{\rm e,beam}}{Q^2_{\rm JB}(1-y_{\rm JB}) + 4y^2_{\rm JB}E^2_{\rm e,beam}} \tag{5.7}$$

$$= \frac{(\sum P_x)^2 + (\sum P_y)^2 - (\sum E - P_z)^2}{(\sum P_x)^2 + (\sum P_y)^2 + (\sum E - P_z)^2} \tag{5.8}$$

where the sum runs over all the calorimeter cells except those belonging to the scattered electron.

The advantage of using angle quantities is that angular resolution is normally better than energy resolution in the detector, providing better accuracy in the kinematic reconstruction.

5.4.4 Kinematic Reconstruction Summary

The quality of the kinematic reconstruction depends largely on the kinematic region of interest. The double angle method has a good resolution at high values of Q^2 and x, but as x and Q^2 decreases, the resolution of the electron method becomes better [34]. To determine the transition point, a study has been done in [34] for dijet events. It showed that a good choice is to use the double angle method if the electron has a track associated with it and $\gamma_{had} < \pi/2$, otherwise use the electron method.

5.5 Jet Reconstruction

Jets were reconstructed using the k_T cluster algorithm (Section 5.5.1.3) in the longitudinally invariant inclusive mode. The jet search was conducted in the Breit frame (Section 5.5.2). For each event, the jet search was performed using a combination of track and calorimeter information, excluding the cells (tracks) associated with the scattered electron. The selected tracks and calorimeter clusters were treated as

massless Energy Flow Objects (EFOs).

To reduce the uncertainty of the absolute energy scale of the calorimeter, the jets are corrected to match the energy scale of the Monte Carlo simulation (see Section 5.5.3). After that the jet energy is corrected for energy losses in the material in front of the calorimeter (see Section 5.5.4).

5.5.1 Jet Algorithm

A jet algorithm is necessary to provide the quantitative definition of a jet. The algorithm has to be measurable, calculable and accurate. There are two classes of jet algorithms commonly used, the cone-type and the clustering-type. The cone-type algorithms use geometrical objects to search for the maximum energy flow through that object. The cluster algorithms group nearby particles or energy deposits according to their relative transverse momentum and distance.

5.5.1.1 Jet Variables

Jet algorithms use certain jet variables to make quantitative selections. The transverse energy (E_T^{jet}), pseudorapidity (η^{jet}) and azimuthal angle (ϕ^{jet}) of the jet are determined from the four-momentum (E, p_x, p_y, p_z) of the jet:

$$\begin{aligned} E_T^{\text{jet}} &= \sqrt{p_x^2 + p_y^2} \\ \eta^{\text{jet}} &= -\ln\tan\frac{\theta}{2} \\ \phi^{\text{jet}} &= \arctan p_y/p_x \end{aligned} \tag{5.9}$$

where $\theta = \arctan E_T^{\text{jet}}/p_z$.

5.5.1.2 Cone Algorithm

The most commonly used cone algorithms follow the Snowmass Convention [42]. All the particles in the event (where particles can be the partons, hadrons or calorimeter cells) which lie above a minimum transverse energy threshold are taken as the seeds (initial positions) of the jets for the event. A cone of fixed radius R is defined around a seed in the $\eta - \phi$ plane, and all particles found within this radius are grouped together:

$$\sqrt{(\eta_{seed} - \eta_i)^2 + (\phi_{seed} - \phi_i)^2} < R \tag{5.10}$$

where i indexes all the particles within the cone. This grouping defines the "first-order" jet. The jet variables, $E_T^{\rm jet}$, $\eta^{\rm jet}$, and $\phi^{\rm jet}$ are then calculated using the particles' positions inside the cone, weighted according to their transverse energy:

$$\begin{aligned} E_T^{\rm jet} &= \sum_i E_{T,i} \\ \eta^{\rm jet} &= \frac{1}{E^T{\rm jet}} \sum_i E_{T,i}\eta_i \\ \phi^{\rm jet} &= \frac{1}{E^T{\rm jet}} \sum_i E_{T,i}\phi_i \end{aligned} \tag{5.11}$$

If the new jet-axis is in a different position than the initial seed position, a cone is again drawn around the position of the jet and the jet properties are recalculated. This process is repeated until the energy flow through the cone is maximal.

The cone algorithm allows the possibility to leave some particles ungrouped, so they are not part of any jet in the event. For this reason, it is often used in hadronic collisions where significant energy remains in the detector that does not originate from the hard interaction. This conceptually simple and computationally fast algorithm is used in this analysis to pre-select events at the ZEUS Third Level

Trigger (Section 2.2.6) and does not enter into the definition of the measured cross section. The algorithm's drawbacks are its inability to handle overlapping jets without applying additional conditions on the jets, and its dependence on a seed to start the jet finding. The cone alogrithm is not infrared safe at next-to-next-leading order (NNLO) [43].

5.5.1.3 k_T Cluster Algorithm

The k_T-cluster [44] algorithm begins by defining the quantity

$$d_i = E_{T,i}^2 \tag{5.12}$$

for each particle i in the event. All the particles are then grouped into pairs and the relative position of the particles is calculated, weighted by the smaller transverse energy of the two.

$$d_{i,j} = min(E_{T,i}^2, E_{T,j}^2)[(\eta_i - \eta_j)^2 + (\phi_i - \phi_j)^2] \tag{5.13}$$

The minimum value of the set of all $d_{i,j}, d_i$ is considered. If the value corresponds to a d_i, then particle i is accepted a jet, it is then removed from the set and not considered for further clustering. If the minimum value corresponds to a $d_{i,j}$, two particles i and j are grouped together according to the following rules:

$$\begin{aligned} E_T &= E_{T,i} + E_{T,j}; \\ \eta &= \frac{E_{T,i}\eta_i + E_{T,j}\eta_j}{E_T} \\ \phi &= \frac{E_{T,i}\phi_i + E_{T,j}\phi_j}{E_T} \end{aligned} \tag{5.14}$$

and d_i and $d_{i,j}$ are then recalculated and the clustering process is iterated until all objects have been merged into jets.

The k_T algorithm has several advantages with repect to the cone-type of algorithms. It has no fixed radius for jets and is not as sensitive to soft energy in the vicinity of the jet. The algorithm allows the merging procedure to clearly separate jets from the proton remnant, which has relatively little transverse energy compared to its momentum in the original proton direction. This avoids the contamination from the proton remnant in the jets near the forward beam-pipe. Also, the k_T algorithm avoids the ambiguities related to the overlapping and merging of jets. The k_T algorithm is considered infrared safe for use with pQCD calculations of jet cross sections at all orders.

In this analysis, jets were reconstructed using the k_T cluster algorithm in the longitudinally invariant inclusive mode [45].

5.5.2 Breit Frame

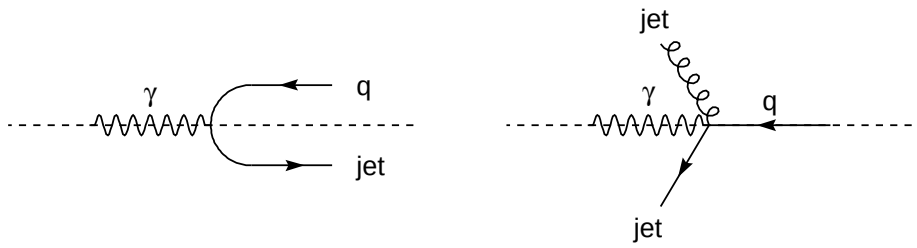

Figure 5.1: The QPM (left) and QCD-Compton (right) diagrams in the Breit Frame. The positive z-direction is horizontally from right to left.

Jet finding can be performed in different frames, one choice is the natural laboratory frame, while on the theoretical side, the Breit frame [46] has certain advantages.

In ep collisions, the Breit frame is defined as the frame in which $\vec{q} + 2x\vec{P} = 0$, where $\vec{q}$ and $\vec{P}$ are the 3-momenta of the colliding boson and proton, respectively. In

the Breit frame, the boson and a parton in the proton collide on a common axis with the z-direction chosen to be the proton direction, see Figure 5.1. In QPM events, the struck quark recoils along the common axis with opposite momentum as if it hits a "brick wall" (so-called "brick-wall frame"), producing zero transverse energy with respect the common axis. In QCDC and BGF events, the two final final state partons are produced with equal transverse energy in the Breit frame (conservation of energy and momentum). This feature of the Breit frame is convenient for selecting multijet events in DIS. By requiring a non-zero transverse energy for the jets in the Breit frame, QPM events (single jet) are rejected and events with at least two jets are kept.

In addition, the Breit frame has the advantage that every object associated with struck quark shifts towards the negative z-direction whereas every object associated with the proton remnant remains in the positive z-direction, resulting in a maximum separation between the two.

In this analysis, the jet search is conducted in the Breit frame.

5.5.3 Calorimeter Energy Scale for Jets

As discussed in Section 5.2, before jet finding occurs, the energies of calorimeter cells are corrected for the difference between the response of the detector in the Monte Carlo simulation and in the data. However, the methods used estimate the average difference in the energy response for single electrons. Differences in the energy response for jets are not expected to exactly match those for single electrons because jets are usually multi-particle objects of mostly hadrons, and can deposit energy in both the electromagnetic and hadronic sections of the calorimeter.

For measuring the energy scale, a sample of pure single-jet DIS events is studied

in the laboratory frame, where a balance between the transverse energy of the scattered electron and the jet in the laboratory frame is expected. The measured scattered electron energy is corrected for energy response difference in the MC and data and is used to predict the transverse energy of the jet. Comparisons between MC and data of the average measured jet transverse energy versus the predicted transverse energy give an estimate of the difference in the detector response between MC and data. This has been done in [47] for jets with transverse energy above 10 GeV, showing that applying these corrections reduces the uncertainty of the absolute energy scale of the calorimeter from 3% to 1%.

5.5.4 Jet Energy Correction

Jet reconstructed in the detector are corrected for energy losses in the dead material. A Monte Carlo technique is used to estimate on average the fraction of energy lost by a *hadron level* (Section 3.1) jet. The fraction roughly depends on the thickness of the dead material that the jet passed through, and thus depends on its polar angle. Therefore, the full measured jet pseudorapidity region $-1 < \eta^{\text{jet}}_{\text{LAB}} < 2.5$ is divided into 17 slices, each overing 0.2 in $\eta^{\text{jet}}_{\text{LAB}}$ (except the last bin covering 0.3).

For events that pass the kinematic selection and background rejection cuts with at least 2 jets, the *detector level* (Section 3.6) jets are then matched at hadron level by requiring hadron and detector level jets to be closer than 1 in η-ϕ-space to ensure that the jets in two levels are highly correlated. In each pseudorapidity subregion, a profile histogram is made of the transverse energy of hadron level jet versus detector level jet. A linear fit is performed in each pseudorapidity subregion, neglecting the bins with too low statistics. The slope obtained from the fit is an estimate of the fraction of the

transverse energy of a hadron level jet retained by the jet after it passes through the dead material.

The jet energy corrections for a jet reconstructed in the detector are obtained by assuming that the jet retains exactly the fraction of transverse energy determined from the fits. The corrected transverse energy of the jet, $E_{T,B}^{\mathrm{CORR}}$, is given by inverting the fit:

$$E_{T,B}^{\mathrm{CORR}} = \frac{E_{T,B}^{\mathrm{jet}} - \mathrm{A0}}{\mathrm{A1}} \tag{5.15}$$

where $E_{T,B}^{\mathrm{jet}}$ is the measured transverse energy of the jet reconstructed in the detector, and A0 and A1 are the intercept and slope, respectively, of the fit in the pseudorapidity region corresponding to the measured jet pseudorapidity.

The multiplicative jet energy correction factor C_{JE} is defined as the ratio of corrected jet transverse energy to the measured jet transverse energy and is applied to all components of the jet four-momentum.

$$C_{\mathrm{JE}} = \frac{E_{T,B}^{\mathrm{CORR}}}{E_{T,B}^{\mathrm{jet}}} \tag{5.16}$$

Chapter 6

Event Selection

The event sample used in this analysis was selected both *online* and $offline$ (Section 2.2.6). Initially, a three-level trigger system was used to select events *online*. The trigger criteria are necessary to meet the bandwidth and storage limitations of ZEUS data acquisition system, but are carefully designed to minimize the loss of events relevant to the measurement in the kinematic range of interest. Data accepted by the trigger are written to tape and later accessed during the $offline$ selection, where the specific events that enter the cross section measurement are chosen.

6.1 Online Event Selection

Event selection is made at all three levels of the ZEUS trigger system: the First Level Trigger (FLT), the Second Level Trigger (SLT) and the Third Level Trigger (TLT). The accuracy of track-based and calorimeter-based quantities improves at each subsequent level in the trigger due to the larger amount of information and increased calculation time available per event. Therefore loose requirements are placed at the first level, followed by increasingly stricter requirements at the second and third levels. For a similar reason, all the *online* requirements made in the trigger are much less

restrictive than the final requirements made in the $offline$ selection.

Neutral current DIS events were selected by requiring that the scattered electron with energy more than 4 GeV was measured in the calorimeter [48]. At each trigger level, the trigger decision is made up with a logical OR of certain number of trigger filters. The logic is defined by assigning a sub-trigger with some threshold values to each trigger filter. At least one of them has to be logical TRUE for the event to pass that level. This analysis uses a combination of three different TLT filters: The photoproduction dijet trigger (HPP14), the medium Q^2 DIS trigger (DIS03) and the fully inclusive, but prescaled DIS trigger (DIS01) (i.e. DIS01 doesn't take every event that are TRUE but only every n-th event, n is the prescale factor). Each of these triggers has its own configuration of FLT and SLT filters for which it works reliably. When using one of these filters it is necessary that at least one of the corresponding FLT and SLT filters took the events. Therefore the filter description of the FLT and SLT filters includes which TLT filter relies on them.

6.1.1 First Level Selection

The Global First Level Trigger (GFLT) decision is mainly based on calorimeter energy deposits as measured by the Calorimeter First Level Trigger (CFLT) [17] and tracking information as reported by the First Level Trigger of the Central Tracking Detector (CTD). The FLT requirements are designed to select events with properties common to events with jets. Jets can deposit both hadronic and electromagnetic energy in any region of the calorimeter. Jets that are well separated from the proton remnant typically have large values of transverse energy. Charged particles from jets result in tracks in the CTD associated with the likely interaction point (so-called "good

tracks").

Several FLT filters are used for this analysis.

- Filter FLT40 takes the event if the electromagnetic energy in the calorimeter exceeds 15 GeV.
- Filter FLT41 takes the event if the total transverse energy in the calorimeter exceeds 21 GeV.
- Filter FLT42 takes the event if there is a good track and one of the following is true:
  - the total energy in the calorimeter is greater than 15 GeV
  - the total electromagnetic energy in the calorimeter is greater than 10 GeV
  - the total electromagnetic energy in the BCAL is greater than 3.4 GeV
  - the total electromagnetic energy in RCAL is greater than 2.0 GeV.
- Filter FLT43 takes the event if the total transverse energy in the calorimeter is greater than 11.5 GeV and a good track is found.
- Filter FLT44 takes the event if the electromagnetic energy in RCAL (BCAL) is greater than 3.4 GeV (4.8 GeV).
- Filter FLT46 takes the event if there is an isolated electromagnetic deposit in the RCAL. In addition it requires one of the following:
  - the total electromagnetic energy in the RCAL is greater than 2 GeV.
  - there is SRTD data and a good track.

– there is a good track and a total energy greater than 18 GeV.

The DIS03 and DIS01 TLT filters use all the above FLT filters while HPP14 TLT filter only uses FLT40, FLT41, FLT43. Additionally, timing information from the VetoWall, C5 and SRTD is used to reject events originating from beam-gas interactions and "cosmic rays". ZEUS components is calibrated in such a way that particles produced at the nominal interaction point have a time of zero ($t = 0$ ns). Particles from beam-gas interactions and cosmic muons will deposit energy in the ZEUS detector other than the time ($t = 0$ ns) at which particles from a true ep interaction would arrive (Figure 6.1). Events are rejected as beam-gas background if the time from the VetoWall is less than -25 ns, or if the absolute value of the C5(SRTD) time is greater than 6 ns (18 ns).

6.1.2 Second Level Selection

Data from all components are available at the SLT, allowing more detailed selections to be made, such as the selection on $E-P_Z$ of the calorimeter energies. Since the $+z$ axis is defined to be along the proton beam direction, the $E - P_Z$ of the incoming proton is 0, while the $E - P_Z$ of the incoming electron is 27.5 - (-27.5) = 55 GeV. By conservation of energy and momentum, the total outgoing $E - P_Z$ must also sum to 55 GeV. Therefore events in which particles emitted from the ep hard scattering are completely contained in the ZEUS detector will have an $E-P_Z$ of 55 GeV, provided all the energy deposits are correctly measured. In DIS events with initial-state radiation (ISR), the photon escapes down the rear beam pipe and lowers the $E - P_Z$ of the event. To compensate for this effect, the energy of the photon as measured by the lumi gamma detector ($E_\gamma^{(lumi)}$) is included. A measurement of the event vertex is made

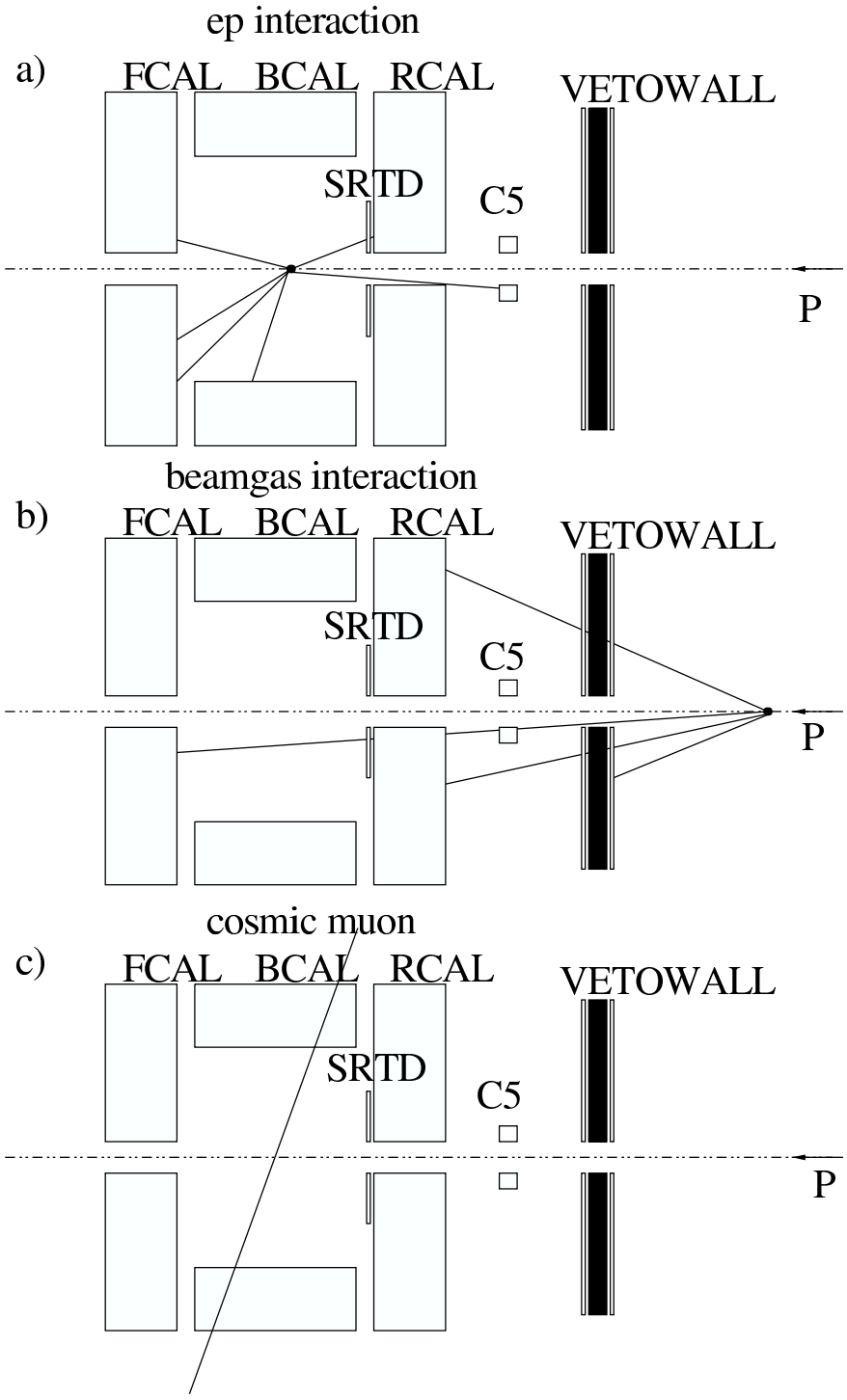

Figure 6.1: Typical signature of: (a) an *ep* interaction at the nominal interaction point, (b) an upstream proton beam-gas interaction and (c) a cosmic muon interaction.

only using the axial wires of the CTD (z-by-timing, see Section 2.7), but with rather poor resolution. By requiring the reconstructed primary vertex z-position, Z_{vertex}, to be within a certain range (somewhere nearby the nominal interaction point), one can reduce upstream or downstream beam-gas background. Further cuts can be made to the timing information in order to reject beam-gas background, sparks and cosmic ray events.

For the SLT, two filters are used:

- Filter DIS06 takes the event if $E - P_z + 2 \cdot E_\gamma^{(lumi)} > 29\,\mathrm{GeV}$ and one of the following:
  - electromagnetic energy in RCAL greater than 2.5 GeV
  - electromagnetic energy in BCAL greater than 2.5 GeV
  - electromagnetic energy in FCAL greater than 10 GeV
  - hadronic energy in FCAL greater than 10 GeV
- Filter HPP01 takes the event if all of the following is true:
  - the vertex is reconstructed with $\mid Z_{\mathrm{vertex}} \mid$ <60 cm or no vertex is reconstructed.
  - there is at least one vertex track
  - $E - P_z > 8\,\mathrm{GeV}$
  - the transverse energy (except for the innermost FCAL ring) is greater than 8 GeV.
  - $E - P_z > 8\,\mathrm{GeV}$ or $P_z/E > 0.95$

The DIS03 and DIS01 TLT filters use DIS06 SLT filter while HPP14 TLT filter uses HPP01 SLT filter.

6.1.3 Third Level Selection

The complete event information is available at the TLT. A nearly complete reconstruction of CTD tracks is used to determine the event vertex, which improves the $E - P_Z$ measurement with respect to the SLT. A jet search is performed in the laboratory frame using all calorimeter cells as input.

Three TLT filters are used and the event is taken if any of the filters takes the event.

- Filter HPP14 is a dijet PHP trigger. It requires at least two jets found in the laboratory frame with an E_T of at least 2 or 2.5 GeV (at the beginning of the 98–00 running period, it was set to 2 GeV and later on it was raised to 2.5 GeV to reduce the rate). For this analysis and this filter, it is required that the two jets with the highest transverse energy each have an uncorrected transverse energy in the lab of at least 5 GeV.

- The filter DIS03 is an inclusive DIS trigger for medium and high Q^2. It requires an electron found with at least 4 GeV energy outside of a circle with radius 35 cm centered around the beam pipe. For this analysis and this filter, it is required that the electron is outside a circle of 36 cm on the face of RCAL.

- The filter DIS01 is a fully inclusive DIS trigger. It requires an electron found with at least 4 GeV of energy outside of a region of $24 \times 12\,\mathrm{cm}^2$ centered around the beam pipe. Depending on the trigger configuration, it has a prescale factor

of 1, 10 or 100, resulting in an integrated luminosity of $11.37\,\mathrm{pb}^{-1}$ (This number has been calculated by summing up the ratios of integrated luminosity and by prescaling for individual runs). In this analysis it is used as a fall-back trigger for events that were not selected by the other two TLT filters, i.e. if an event is taken by either HPP14 or DIS03, it is filled with a weight of $1/82.2\,\mathrm{pb}^{-1}$ (corresponding to the full luminosity) and if it is not taken by those filters but taken by DIS01 it is filled with a weight of $1/11.37\,\mathrm{pb}^{-1}$ (corresponding to the prescaled luminosity).

6.2 Offline Event Selection

For an event that passes the online selection, event variables and jets are reconstructed by the methods described in Chapter 5 and offline selection criteria are imposed on these variables to obtain a sample of Neutral Current DIS trijet (dijet) events in the kinematic range of interest. Additional cuts are made to avoid low efficiency or purity (Section 7.1) regions of the detector and to reject background events.

6.2.1 Background Rejection

- $E_{\mathrm{prob}} > 0.9$ and E'_e>10 GeV, where E_{prob} is the finding probability of the scattered electron using the Sinistra95 program and E'_e is the fully corrected scattered electron energy (Section 5.3). The primary signature that distinguishes Neutral Current DIS from other processes is the scattered electron in the calorimeter. This selection ensures a high-purity sample of NC DIS events;

- $\mid X \mid$ >13 or $\mid Y \mid$ >7 cm, where X and Y are the impact positions of the scattered electron on the RCAL, to avoid the low-acceptance region adjacent to

the rear beam-pipe;

- $40 < \sum_i (E - P_Z)_i < 60\,\mathrm{GeV}$, where the sum runs over all calorimeter energy deposits. The lower cut removed background from photoproduction and events with large initial-state QED radiation. The higher cut removed cosmic-ray background;

- $(E - P_z)_e < 54\,\mathrm{GeV}$, where $(E - P_z)_e$ is the $E - P_Z$ calculated for the scattered electron only. If the electron is scattered at low angles with high energy it loses hardly any energy and $E - P_z$ (so-called "kinematic-peak events"[1]). Due to the finite energy resolution of the calorimeter, the measured energy of the scattered electron in kinematic-peak events can be larger than the kinematic limit (27.5 GeV), resulting in a poor reconstruction of the Breit frame. This rejects the kinematic-peak events;

- $| Z_{\mathrm{vertex}} | < 50$ cm to select events consistent with ep collisions and well-contained in the calorimeter and CTD acceptance regions (Section 6.1.2).

- $P_T/\sqrt{E_T} < 3\sqrt{\mathrm{GeV}}$, where P_T is the total transverse momentum of the final-state particles and E_T is the total transverse energy. Transverse momentum conservation requires no total transverse momentum in the final state for ep collisions. However, due to the finite resolution of the calorimeter, the deviation of the transverse momentum scales approximately with the transverse energy times the resolution (Section 2.5). Imposing a upper limit on P_T removes cosmic-ray events.

[1] Kinematic-peak events are those with a scattered electron near the RCAL beam pipe and with a very low value of y, such that the scattered electron energy is close to the beam energy of 27.5 GeV

- $\eta_{\max} > 2.5$, where $\eta_{\max}$ is the jet pseudorapidity in the laboratory frame of the most forward energy deposition in the calorimeter to reject diffractive events.

6.2.2 Kinematics Selection

- $10\,\mathrm{GeV}^2 < Q^2 < 5000\,\mathrm{GeV}^2$, where Q^2 is reconstructed as described in Sec. 5.4. The lower end of the kinematic region ensures good acceptance by the ZEUS detector and the upper cut was chosen to exclude low statistics regions;

- y_e<0.6, where y_e is y reconstructed via the electron method as defined in Sec. 5.4, to reduce the photoproduction background (mostly due to highly energetic pions in the very forward region of the calorimeter decaying into two photons) and avoid the low-acceptance region adjacent to the forward beam-pipe;

- y_{JB}>0.04, where y_{JB} is y reconstructed by the JB method as defined in Sec. 5.4, to ensure sufficient accuracy for the hadronic system reconstruction and to reject kinematic-peak events;

- $\cos\gamma_{had}$<0.7, where $\cos\gamma_{had}$ is the hadronic angle as defined in Sec. 5.4. Good reconstruction of jets requires a good position resolution in the calorimeter. In the Breit frame the calorimeter geometry is different from the laboratory frame: the η-ϕ space in the rear region is contracted, while the geometry in the forward region where near the proton remnant is stretched out, especially for large values of γ_{had}. Therefore the boundaries of the cells which are between the remnant and the struck quark energy deposits enlarge with respect to the laboratory frame, giving a poor granularity and a poor resolution of the jet

position measurement [47]. This selection ensures good reconstruction of jets in the Breit frame.

6.2.3 Jet Selection

The jet finding is performed on groups of energy deposits in the calorimeter called EFOs (Section 5.2). The EFOs are first boosted to the Breit frame and then passed on to the jet finder. The jet finder uses K_T cluster algorithm [44] in the longitudinally invariant inclusive mode.

- $-1 < \eta^{\rm jet}_{\rm LAB} < 2.5$, where $\eta^{\rm jet}_{\rm LAB}$ is the jet pseudorapidity in the lab frame when jets are boosted from the Breit frame to the lab frame, to make sure the jets are fully contained in the calorimeter with good acceptance;

- $E^{\rm jet}_{T,B}$>5 GeV, where $E^{\rm jet}_{T,B}$ is the (corrected) jet transverse energy in the Breit frame. Soft partonic radiation tends to produce a soft jet with low transverse energy while a hard process yields a relatively high transverse energy jet (Section 1.4). The aim of the analysis is to measure jet cross sections due to the hard *ep* scattering, thus a minimum transverse energy is required. In addition, high energy jets can be measures with higher precision than low energy jets. However, requiring too high energy jets will limit the phase-space of the measurement and the amount of usable statistics;

- Events with two or more jets were selected by requiring the invariant mass of the two highest $E^{\rm jet}_{T,B}$ jets to be: $M_{\rm 2jet}> 25$ GeV;

- Events with three or more jets were selected by requiring the invariant mass of the three highest $E^{\rm jet}_{T,B}$ jets to be: $M_{\rm 3jet}> 25$ GeV; These requirements were

necessary to ensure a reliable prediction of the cross sections to next-to-leading order, see Section 4.4.

After all online and offline cuts, 37089 events with two or more jets and 13665 events with three or more jets, remained.

Chapter 7

Analysis Method and Data Correction

The aim of this analysis is to measure cross sections of dijet and trijet production in neutral current deep inelastic scattering and compare the measured cross sections with the most accurate QCD calculations up to now — NLO calculations (Chapter 4). Based on the result of the comparison, the strong coupling constant, α_s, a fundamental parameter of the QCD theory, can therefore be determined within systematic uncertainties.

7.1 Cross Section and Corrections

The cross section is the reaction probability, i.e. the likelihood for certain physical process to occur in the particle collision (in this case, *ep* collision at HERA). The Cross section can be obtained in experiment (measured cross sections) or in theory (NLO calculations).

The measured cross section is directly proportional to the number of physical events occurring in the detector (so-called "data events"). The proportionality constant is the reciprocal of the integrated luminosity $\mathcal{L}$.

The general definition of a measured cross section:

$$\sigma_{measured} = \frac{N_{event}^{data}}{\mathcal{L}} \tag{7.1}$$

However, the number of data events cannot be measured directly, because the detector efficiency (percentage of data events observed) is not 100% and the detector purity (percentage of correctly observed data events) is not 100%.

The modified measured cross-section definition:

$$\sigma = \frac{purity}{efficiency} \cdot \frac{N_{event}^{data}}{\mathcal{L}} = c \cdot \frac{N_{event}^{data}}{\mathcal{L}} \tag{7.2}$$

where the detector correction c is defined as the ratio of the detector purity and efficiency. The detector purity and efficiency can be determined by comparing a simulated response of the detector with the ideal case (100% purity and efficiency). In order to do that, a LO Monte Carlo simulation (Chapter 3) is used. Monte Carlo simulation includes both true (*hadron level*, Section 3) and observed (*detector level*, Section 3.6) events.

The definition of the detector purity, efficiency and correction factor:

$$efficiency = \frac{number\ of\ events\ accepted\ at\ the\ hadron\ level\ AND\ observed\ at\ the\ detector\ level}{number\ of\ events\ accepted\ at\ the\ hadron\ level}$$

$$purity = \frac{number\ of\ events\ accepted\ at\ the\ hadron\ level\ AND\ observed\ at\ the\ detector\ level}{number\ of\ events\ reconstructed\ at\ the\ detector\ level}$$

$$c = \frac{purity}{efficiency} = \frac{number\ of\ events\ accepted\ at\ the\ hadron\ level}{number\ of\ events\ observed\ at\ the\ detector\ level} \tag{7.3}$$

On the other hand, NLO calculations give the cross section directly, σ_{NLO}, without counting the hadronization effects (Section 3.4) and high order QED effects (Section 3.5). Therefore, estimates of the QED effects and hadronization effects are determined using a LO MC model, as explained in Sec. 7.4 and 7.5. The QED correction

factor c_{QED} is applied to the measured cross section and the hadronization correction factor c_{HAD} is applied to the NLO calculated cross section.

The final definition of the measured (experimental) and NLO calculated (theoretical) cross sections:

$$\sigma_{measured} = c_{QED} \cdot c \cdot \frac{N_{event}^{data}}{\mathcal{L}}$$
$$\sigma_{calculated} = c_{HAD} \cdot \sigma_{NLO} \tag{7.4}$$

7.2 Comparison of Monte Carlo and Data

The LO MC must adequately describe the data sample, since a poor description of the experimental data leads to the loss of validity in the MC simulation and eventually the inaccuracy in the measured cross sections. In practice, the MC simulations in this analysis are not perfect, but describe the data adequately enough to keep the resulting systematic uncertainties low. In order to achieve a better description of the data, a reweighting method is used to improve the physics model used by the MC simulations, .

7.2.1 Monte Carlo Reweighting

In this analysis, the weight (probability) for the Monte Carlo events is adjusted (so-called "Monte Carlo Reweighting") to improve the Q^2 dependence of the simulation. The comparisons between the data and MC simulations before and after reweighting are shown in Figure 7.1. The reweighting procedure is listed below:

1. Since the dijet sample is much bigger than the trijet sample, only dijets are considered in the reweighting MC sample.

2. To best match MC simulations to data, the ratio of data to detector level MC as a function of $\log Q^2$ is plotted and fitted to a straight line (Figure 7.1).

3. For each MC event, a reweighting factor corresponding to Q^2 is given by the fit. The reweighting factors of the LEPTO and ARIADNE program are:

$$f_{\text{LEPTO}} = 1.305 - 0.202 \cdot \log_{10}(Q^2/\text{GeV}^2)$$
$$f_{\text{ARIADNE}} = 0.365 + 0.478 \cdot \log_{10}(Q^2/\text{GeV}^2) \quad (7.5)$$

4. The weight of the event is then divided by the reweighting factor.

The difference in the LEPTO (ARIADNE) correction factors before and after reweighting was negligible ($< 0.4\%$) thus reweighting MC sample doesn't bias our sample.

7.2.2 Control Plots

After reweighting, the LEPTO 6.5 MC program, as discussed in Chapter 3, is used for all data and MC comparisons. The comparison results are shown in Figs. 7.2 to 7.5 (so-called "control plots").

In Figure 7.2, the distributions of kinematic variables, Q^2, y_{EL}, y_{JB}, γ_h are compared between the data and the detector level predictions of the LEPTO MC program. The variables are well described by the Monte Carlo simulation.

In Figure 7.3, the distributions of reconstructed event variables are compared. The scattered electron energy is fully corrected as described in Chapter 5. A good description of the scattered electron energy is necessary for accurate selection of DIS events and assures the accuracy when boosting particles between the laboratory and

Before Monte Carlo Reweighting:

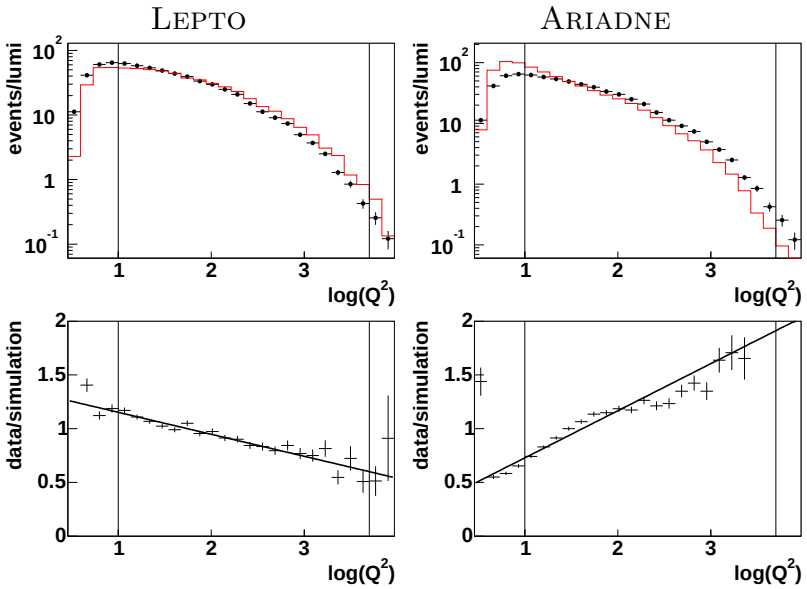

After Monte Carlo Reweighting:

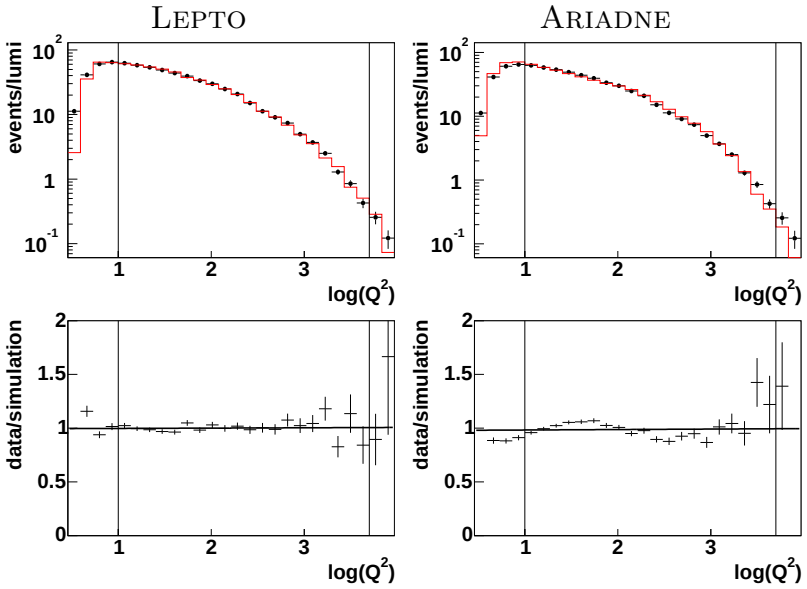

Figure 7.1: Detector level comparisons for Q^2 distributions before and after reweighting for both LEPTO (left) and ARIADNE (right). The points are the data and the solid histograms are the MC simulation.

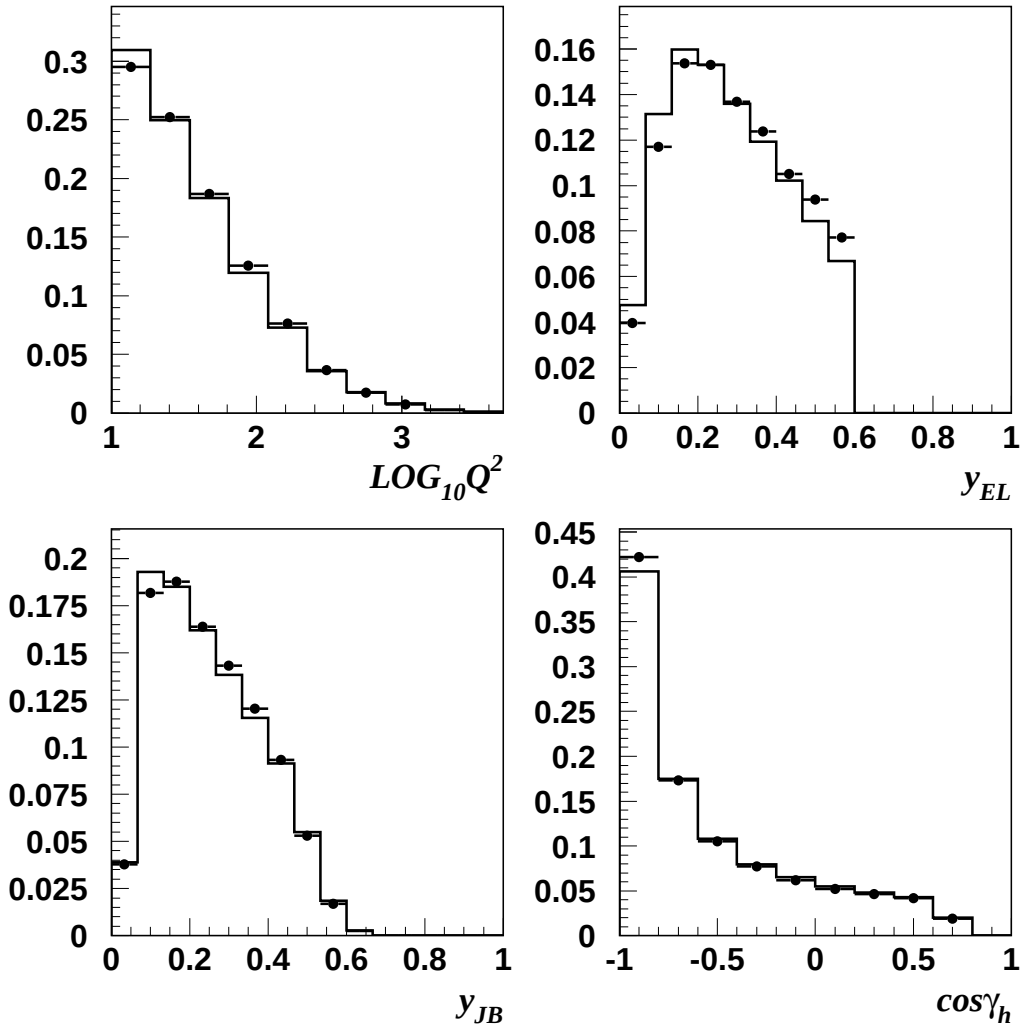

Figure 7.2: Distributions of Q^2, y_{EL}, y_{JB}, $cos\gamma_h$. The points are the data, and the solid histograms are the detector level predictions of the LEPTO MC program. The distributions are area normalized in order to compare shapes.

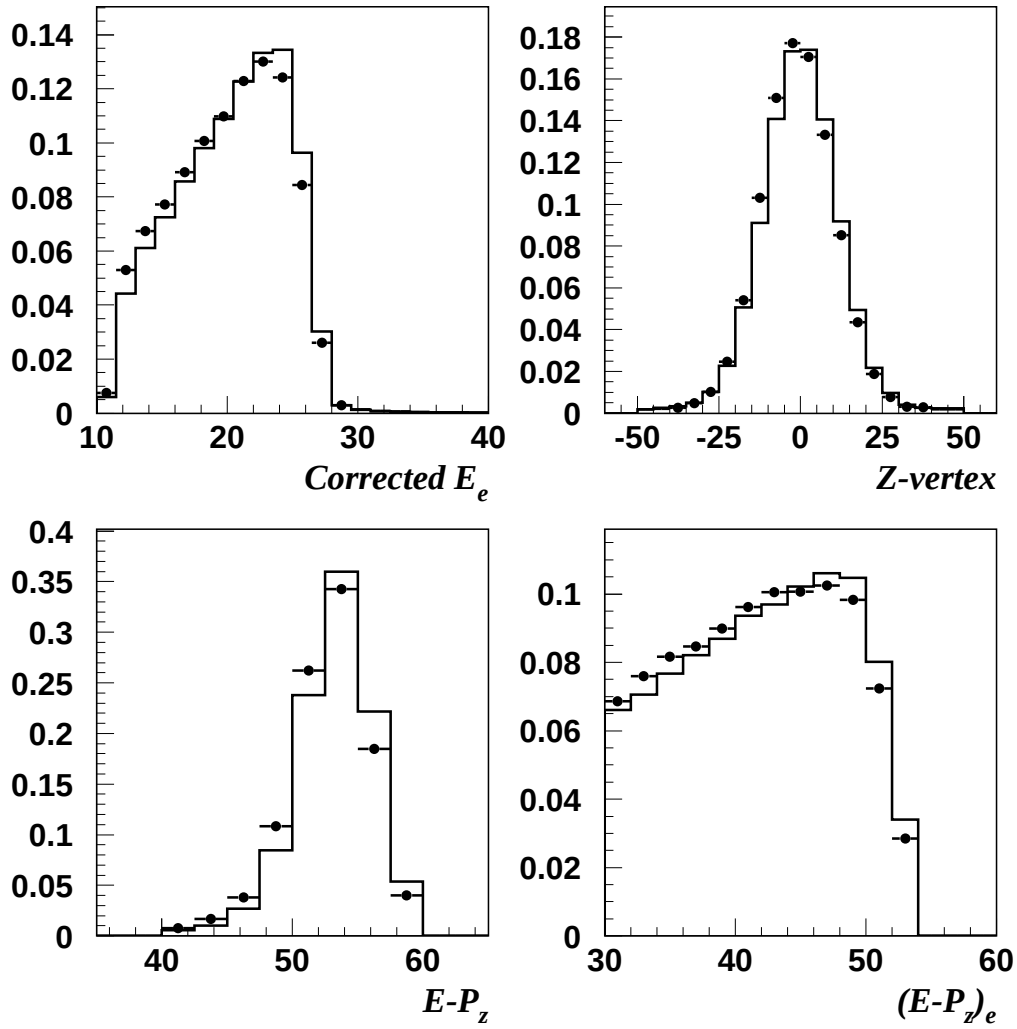

Figure 7.3: Distributions of fully corrected electron energy, z-position of the reconstructed vertex for the offline event samples, $E - P_Z$ and $(E - P_Z)_e$. The points are the data, and the solid histograms are the detector level predictions of the LEPTO MC program. The distributions are area normalized in order to compare shapes.

the Breit frame. The description of the scattered electron energy after correction is adequate, although not perfect. The level of agreement between data and Monte Carlo is comparable to the previous ZEUS analysis [49]. The detector level event vertex distribution is an input into the MC generators and was determined from the measured vertex distribution of the full inclusive NC DIS sample. Thus, the small disagreement between the data and MC distribution indicates that the measured vertex distribution of the full inclusive NC DIS sample is not equivalent to the measured vertex distribution of the selected inclusive dijet (trijet) sample. This results in a small systematic uncertainty on the measured cross sections, as described in Section 8.5. The $E - P_Z$ distribution is not very well described due to an incomplete understanding of the electromagnetic energy scale as seen in the distributions of $E - P_Z$ and $(E - P_Z)_e$, resulting in a systematic error for the measurement. However, this systematic effect is found to be negligible, as described in Section 8.5.

In Figure 7.4, the distributions of the jet transverse energies in the Breit frame and jet pseudorapidities in the laboratory frame are compared between the data and the detector level predictions of the LEPTO MC for the selected dijet sample. The pseudorapidity of the second jet is falling in the forward region due to the $\eta^{\rm jet}_{\rm LAB}$ ordering. The shapes of the jet distributions are well described except in the most forward pseudorapidity bin of the most forward jet.

In Figure 7.5, the distributions of the jet transverse energies in the Breit frame and jet pseudorapidities in the laboratory frame are compared between the data and the detector level predictions of the LEPTO MC program for the selected trijet sample. A similar observation of the falling behavior of the pseudorapidity distribution of the

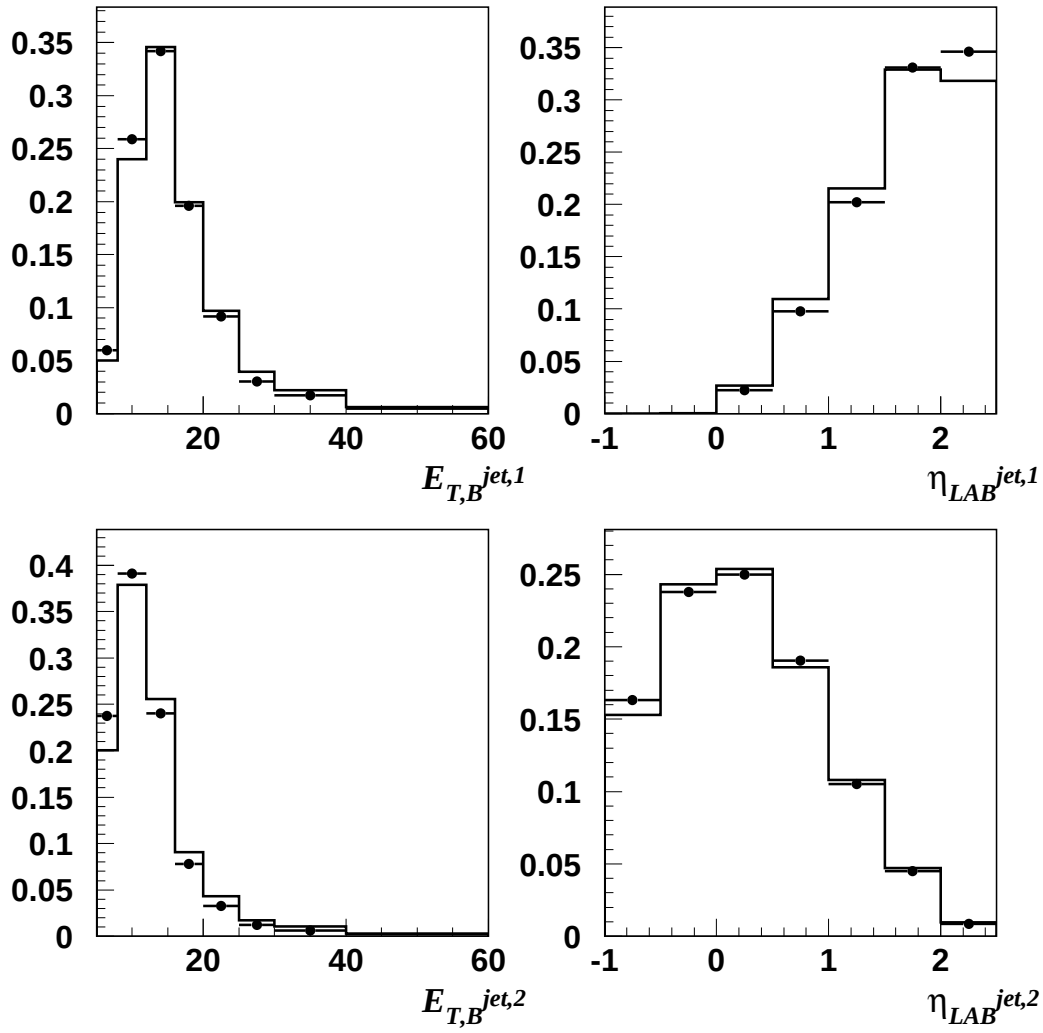

Figure 7.4: Distributions of $E_{T,B}^{\rm jet,1}$, $E_{T,B}^{\rm jet,2}$, $\eta_{\rm LAB}^{jet,1}$ and $\eta_{\rm LAB}^{jet,2}$ for the selected dijet sample. The jets were ordered either in $E_{T,B}^{\rm jet}$ or $\eta_{\rm LAB}^{\rm jet}$ ($E_{T,B}^{\rm jet,1}>E_{T,B}^{\rm jet,2}$, $\eta_{\rm LAB}^{jet,1}>\eta_{\rm LAB}^{\rm jet,2}$). The points are the data, and the solid histograms are the predictions of the LEPTO Monte Carlo program. The distributions are area normalized in order to compare shapes.

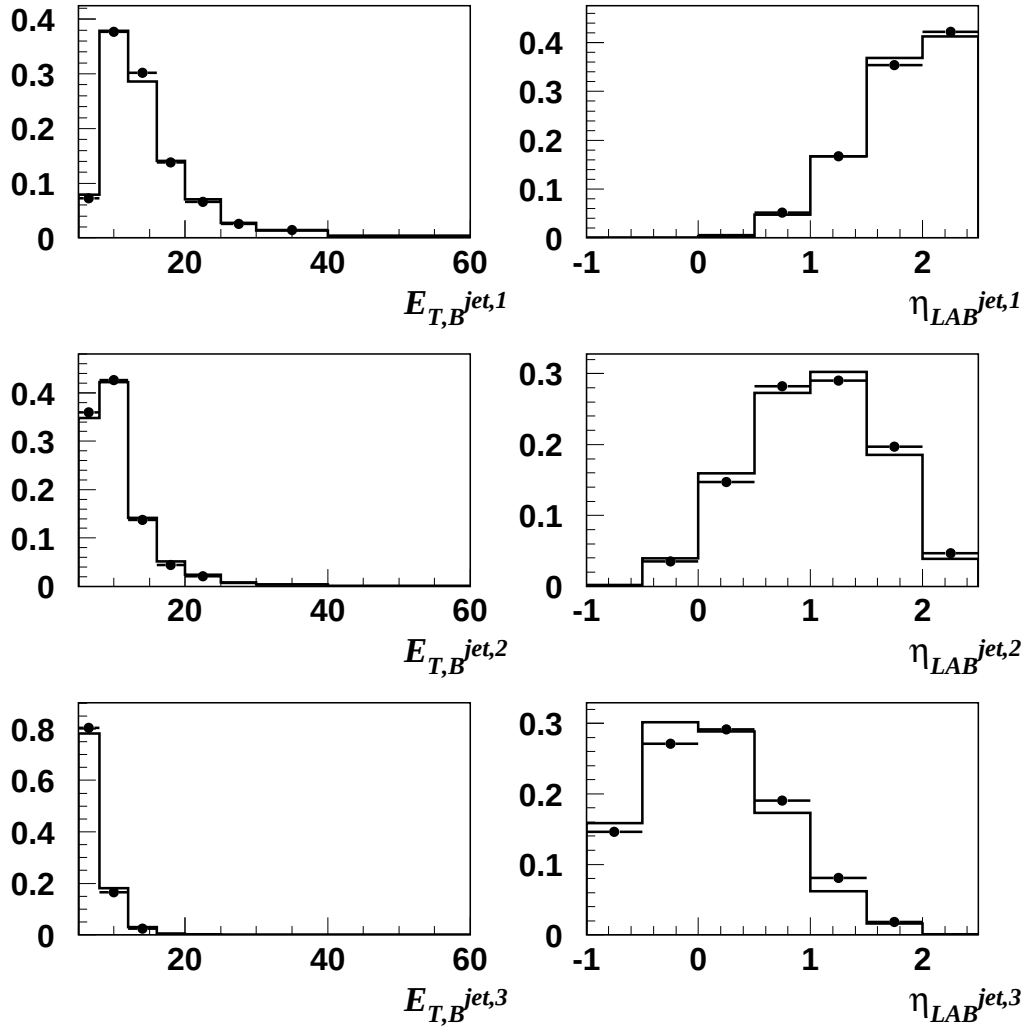

Figure 7.5: Distributions of $E_{T,B}^{\rm jet,1}$, $E_{T,B}^{\rm jet,2}$, $E_{T,B}^{\rm jet,3}$ $\eta_{\rm LAB}^{jet,1}$, $\eta_{\rm LAB}^{jet,2}$, and $\eta_{\rm LAB}^{jet,3}$ for the selected trijet sample. The jets were ordered either in $E_{T,B}^{\rm jet}$ or $\eta_{\rm LAB}^{\rm jet}$ ($E_{T,B}^{\rm jet,1}$>$E_{T,B}^{\rm jet,2}$>$E_{T,B}^{\rm jet,3}$, $\eta_{\rm LAB}^{jet,1}$>$\eta_{\rm LAB}^{\rm jet,2}$>$\eta_{\rm LAB}^{\rm jet,3}$). The points are the data, and the solid histograms are the predictions of the LEPTO Monte Carlo program. The distributions are area normalized in order to compare shapes.

second and third jet in the forward region is again due to the $\eta^{\rm jet}_{\rm LAB}$ ordering. The shapes of the jet distributions are well described.

7.3 Purities, Efficiencies, Corrections Factors

Given the agreement between data and detector level Monte Carlo simulations, the detector purities, efficiencies and corrections are ready to be calculated. The results are shown in Figs. 7.6 to 7.8.

The detector purities and efficiencies, along with the detector correction factors for Q^2 are shown in Figure 7.6. The correction factors are generally around $1-1.2$ and the purities and efficiencies are around $50\%-80\%$. It can be seen that trijet purities and efficiencies are lower than dijet ones. This is due to additional migrations introduced when requiring a third jet.

In Figure 7.7, the dijet purities, efficiencies and detector correction factors for the jet transverse energies in the Breit frame and jet pseudorapidities in the laboratory frame are shown. The correction factors are generally around $1-1.2$ except in the low jet transverse energy and backward region of the leading $E^{\rm jet}_{T,B}$ jet. Purities and efficiencies are generally within $40\%-80\%$. For the leading $E^{\rm jet}_{T,B}$ jet, the purities and efficiencies fall off in the low jet transverse energy region. Events with low generated jet energies are less likely to pass the minimum jet transverse energy and invariant mass requirements due to energy losses in dead material and the energy resolution of the calorimeter. Similarly, events with higher generated transverse energy migrate to lower values of jet transverse energy. These effects result in decreasing values of purities and efficiencies in low jet transverse energy region. However, due to the ordering in $E^{\rm jet}_{T,B}$ ($E^{\rm jet,1}_{T,B}>E^{\rm jet,2}_{T,B}$), these effects are reduced for the second $E^{\rm jet}_{T,B}$ jet. Efficiencies

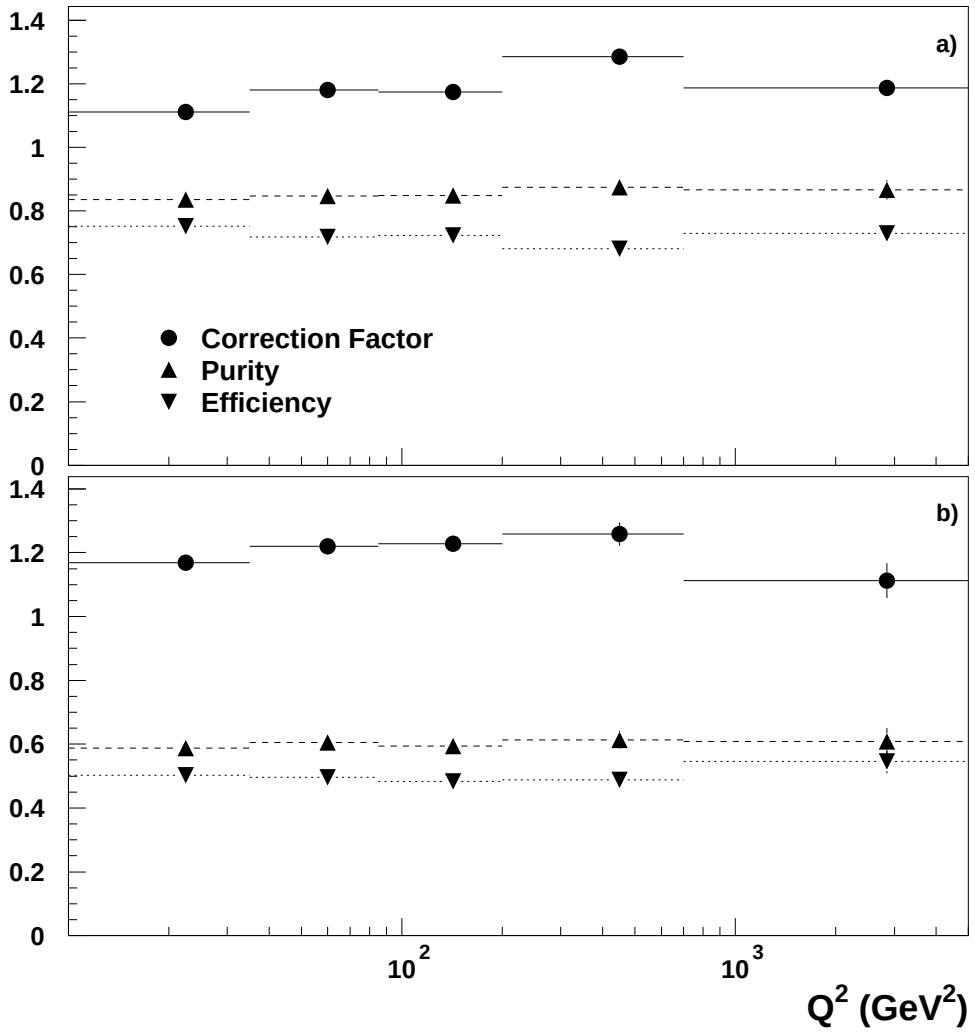

Figure 7.6: a) Purities, efficiencies and correction factors vs. Q^2 for the selected dijet sample. b) Purities, efficiencies and correction factors vs. Q^2 for the selected trijet sample. Quantities are calculated in the same bins as the measured cross sections.

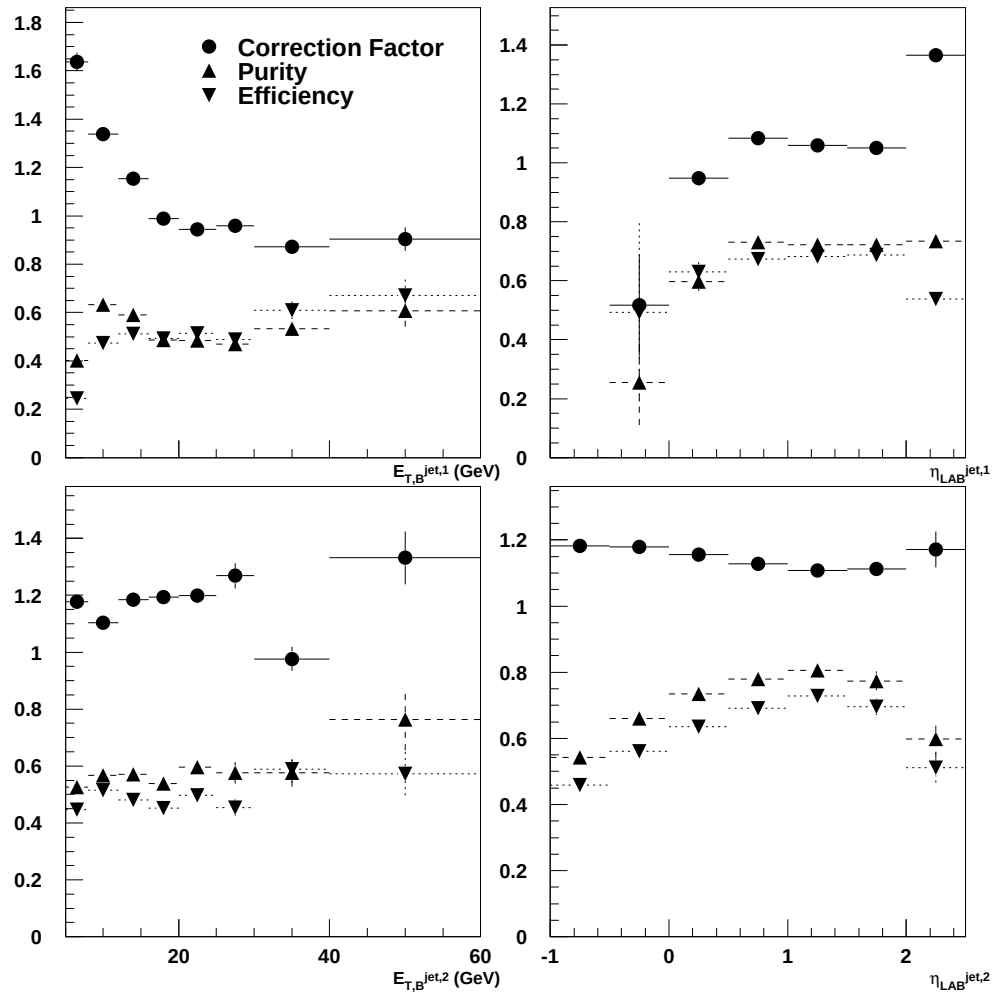

Figure 7.7: Purities, efficiencies and correction factors for $E_{T,B}^{\mathrm{jet},1}$, $E_{T,B}^{\mathrm{jet},2}$, $\eta_{\mathrm{LAB}}^{jet,1}$ and $\eta_{\mathrm{LAB}}^{\mathrm{jet},2}$ of the selected dijet sample. Quantities are calculated in the same bins as the measured cross sections.

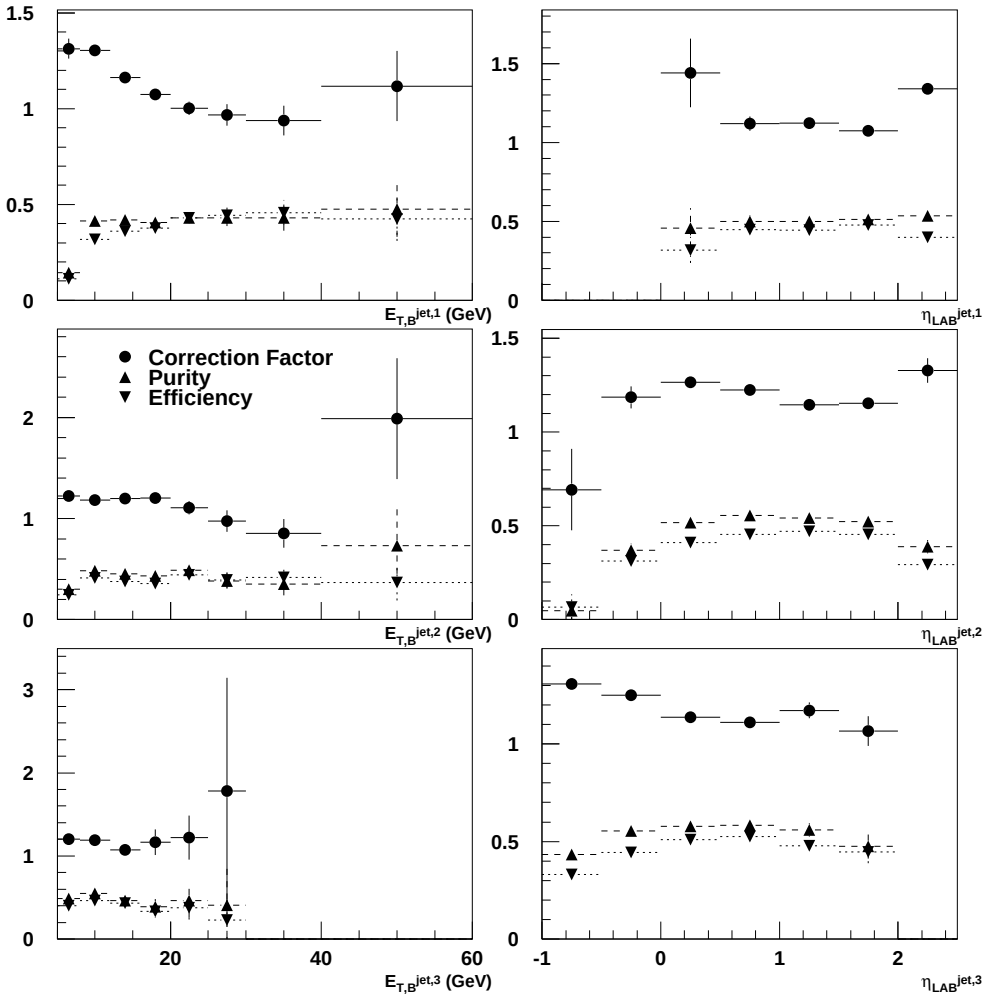

Figure 7.8: Purities, efficiencies and correction factors for $E_{T,B}^{\mathrm{jet},1}$, $E_{T,B}^{\mathrm{jet},2}$, $E_{T,B}^{\mathrm{jet},3}$, $\eta_{\mathrm{LAB}}^{jet,1}$, $\eta_{\mathrm{LAB}}^{jet,2}$ and $\eta_{\mathrm{LAB}}^{\mathrm{jet},3}$ of the selected trijet sample. Quantities are calculated in the same bins as the measured cross sections.

drop in the most forward $\eta_{\rm LAB}$ bins due to the forward limit of the CTD acceptance (Section 2.7). Efficiencies drop in the most backward region due to the low jet finding efficiency in the low jet pseudorapidity region. Purities drop near the high and low end of the jet pseudorapidity boundary due to jet migration, especially, when ordering jet in $\eta^{\rm jet}_{\rm LAB}$ ($\eta^{jet,1}_{\rm LAB}$>$\eta^{\rm jet,2}_{\rm LAB}$), the migration effect is strong in the most backward region for the leading $\eta^{\rm jet}_{\rm LAB}$ jet and the most forward region for the second $\eta^{\rm jet}_{\rm LAB}$ jet.

In Figure 7.8 the trijet purities, efficiencies and detector correction factors for the jet transverse energies in the Breit frame and jet pseudorapidities in the laboratory frame are shown. The correction factors are generally between $1-1.4$ except in the most backward region of the second $\eta^{\rm jet}_{\rm LAB}$ jet and the highest jet transverse energy bin of the second and third $E^{\rm jet}_{T,B}$ jet. Purities and efficiencies are generally within $40\%-60\%$ and lower than the dijet purities and efficiencies. Similar effects of low purities and efficiencies in low jet transverse energy region and most backward and forward region are observed, as described in Figure 7.7. Due to the strong ordering in $\eta^{\rm jet}_{\rm LAB}$, there is no sufficient statistics available for the most backward region of the leading $\eta^{\rm jet}_{\rm LAB}$ jet and the most forward region of the third $\eta^{\rm jet}_{\rm LAB}$ jet.

7.4 QED Corrections

The NLO calculations in most programs only includes LO QED effects that are easier to implement and do not include higher-order QED effects like initial and final state radiation (ISR/FSR) (Section 3.5). The data, on the other hand, include all QED effects. Therefore, certain correction factor has to be applied to the data in order to make a comparison between the measured cross sections and the NLO calculations. The cross section without radiative effects (N^{BORN}), is divided by the cross section

with radiation included (N^{RAD}) for each bin, to determine the QED correction factor in that bin:

$$c_{QED} = \frac{N^{BORN}}{N^{RAD}} \tag{7.6}$$

The QED correction factors are calculated bin-by-bin using the LEPTO program. The factors are typically below 5%.

7.5 Hadronization Corrections

The NLO calculations also do not include hadronization effects (Section 3.4) but the data do. In order to make the comparison, the NLO predictions were corrected for hadronization effects using a bin-by-bin procedure using the LEPTO program. Hadronization correction factors were defined for each bin as the ratio of the parton-level to hadron-level cross section:

$$c_{HAD} = \frac{N^{PAR}}{N^{HAD}} \tag{7.7}$$

The hadronization correction factors are in the range $1.15 - 1.35$ for most of the phase space.

Chapter 8

Results

The measured cross sections[1] are determined from the selected data sample, after corrections for detector effects and initial- and final-state radiation. In this analysis, the differential cross sections for dijet and trijet production and the differential cross-section ratio of trijet to dijet production are presented. Measurements of the inclusive dijet and trijet cross section as functions of Q^2 and the jet transverse energy, $E_{T,B}^{\text{jet}}$, in the Breit frame and the jet pseudorapidity, $\eta_{\text{LAB}}^{\text{jet}}$, in the laboratory frame are also shown. Predictions of NLO pQCD calculations are compared to the measurements. In addition, the ratio of inclusive trijet to dijet cross section, $R_{3/2}$, is presented as a function of Q^2. The dependence of this ratio on Q^2 is used to determine the strong coupling constant α_s.

8.1 Measurement of the Differential Cross Section in Q^2

Figure 8.1a shows both the differential dijet and trijet cross section as functions of Q^2. The measured cross sections are compared to the NLO predictions from the

[1]The cross sections given in this chapter are differential cross sections, i.e. the cross sections are divided up into several bins, normalized to bin widths and plotted at bin centers. No bin-center corrections are applied.

NLOJET program. The cross section decrease by three orders of magnitude in the range $10<Q^2<5000\,\mathrm{GeV}^2$ and the predictions of the NLO calculations provide a good description of both the shape and magnitude of the measured cross sections, even at low Q^2. This is shown explicitly in Figure 8.1b and Figure 8.1c where the ratio of the measured cross section to the NLO prediction is presented.

The NLO calculation of NLOJET is made with renormalization and factorization scale squared (μ_R^2 and μ_F^2) both set to $(\bar{E}_T^2+Q^2)/4$ and using the CTEQ6 input parton density function. The renormalization scale uncertainty is estimated by varying both scales up and down by a factor of 2 at the same time. The uncertainty due to this variation is shown as a hatched band. For low Q^2 ($Q^2<100\,\mathrm{GeV}^2$), the measurement is more precise than the NLO calculations: the theoretical uncertainty dominates the overall uncertainty. For high Q^2($Q^2>100\,\mathrm{GeV}^2$), the size of the theoretical uncertainty is comparable to the size of the measurement uncertainty.

8.2 Measurement of the Differential Cross Section in $E_{T,B}^{\mathrm{jet}}$

The differential trijet cross sections as functions of $E_{T,B}^{\mathrm{jet}}$ are presented in Figure 8.2. The three jets were ordered in $E_{T,B}$ ($E_{T,B}^{\mathrm{jet},1}>E_{T,B}^{\mathrm{jet},2}>E_{T,B}^{\mathrm{jet},3}$). The observed decrease of the cross section for the first jet towards small values of $E_{T,B}$ is caused by the $E_{T,B}$ ordering imposed in addition to the requirement that the second and third jet have $E_{T,B}>5\,\mathrm{GeV}$. For the second jet, a similar but less pronounced effect is observed. The NLO predictions using NLOJET are compared to the measured cross sections and agree well with the data for both the shape and magnitude, even at low $E_{T,B}$.

The differential dijet cross sections as functions of $E_{T,B}^{\mathrm{jet}}$ are presented in Fig-

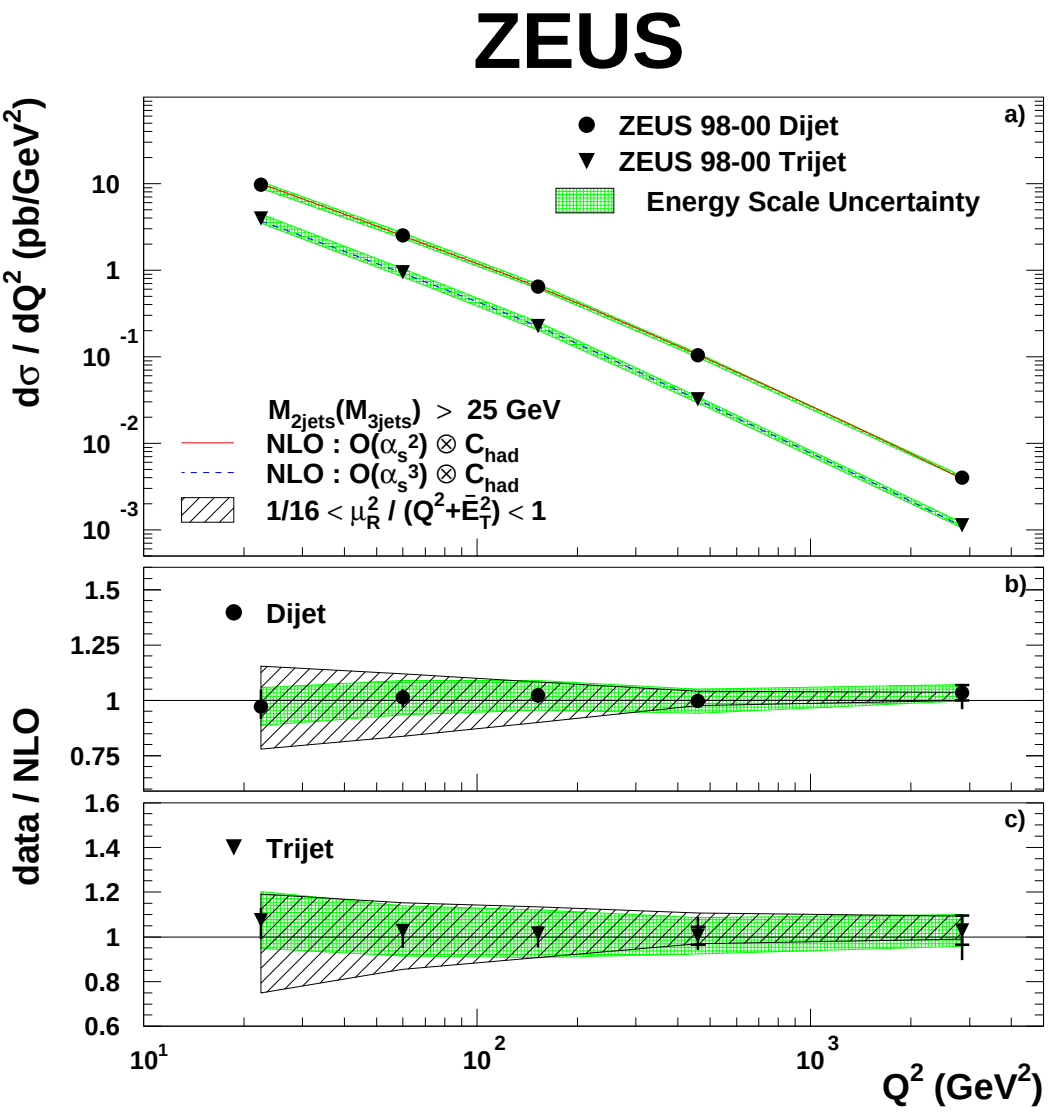

Figure 8.1: a) The inclusive dijet and trijet cross sections as functions of Q^2. The predictions of perturbative QCD in next-to-leading order, corrected for hadronisation effects and using the CTEQ6 parameterizations of the proton PDFs, are compared to the data. b) and c) show the ratio of the data over predictions. The points represent the measured cross section. The inner error bars represent the statistical uncertainties and the outer error bars represent the quadratic sum of statistical and systematic uncertainties not associated with the calorimeter energy scale. The shaded band indicates the calorimeter energy scale uncertainty. The hatched band represents the renormalization scale uncertainty of the QCD calculation.

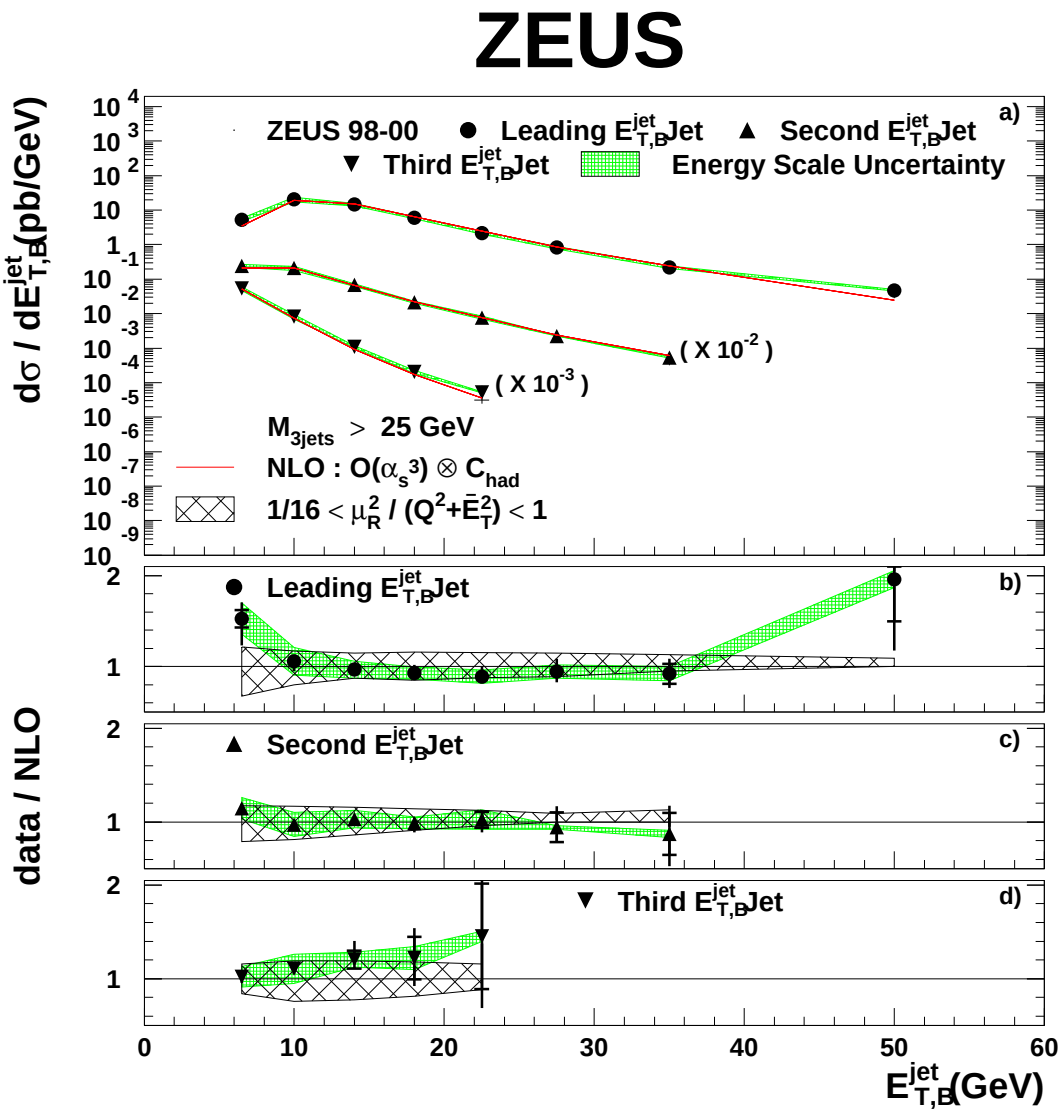

Figure 8.2: a) The inclusive trijet cross sections as functions of $E^{\rm jet}_{T,B}$ with the jets ordered in $E^{\rm jet}_{T,B}$. The cross sections of the second and third jet were scaled down for readability only. The predictions of perturbative QCD in next-to-leading order are compared to the data. b), c) and d) show the ratio of the data over predictions. Other details are as described in the caption to Fig. 8.1.

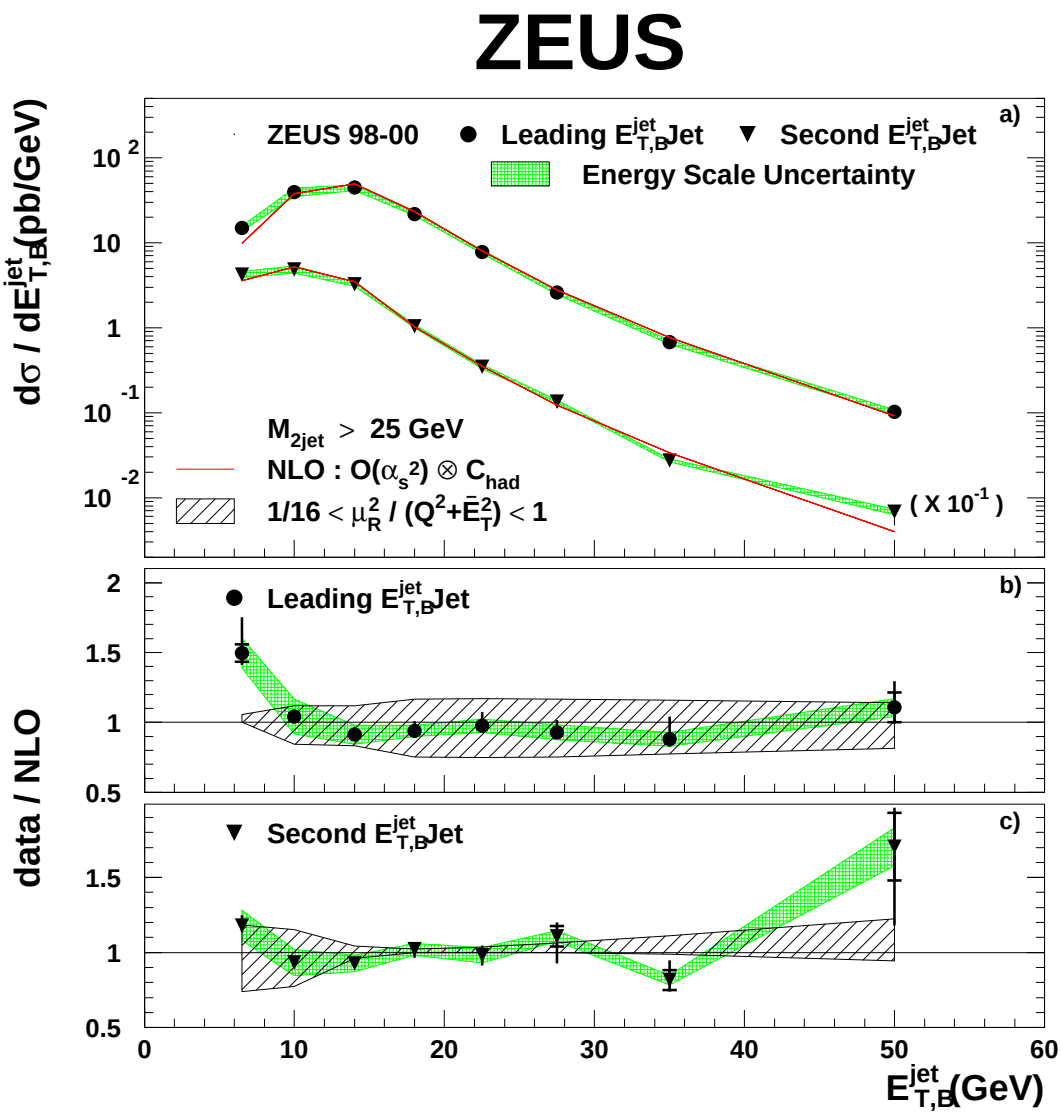

Figure 8.3: a) The inclusive dijet cross sections as functions of $E^{\rm jet}_{T,B}$ with the jets ordered in $E^{\rm jet}_{T,B}$. The cross sections of the second jet was scaled down for readability only. The predictions of perturbative QCD in next-to-leading order are compared to the data. b) and c) show the ratio of the data over predictions. Other details are as described in the caption to Fig. 8.1.

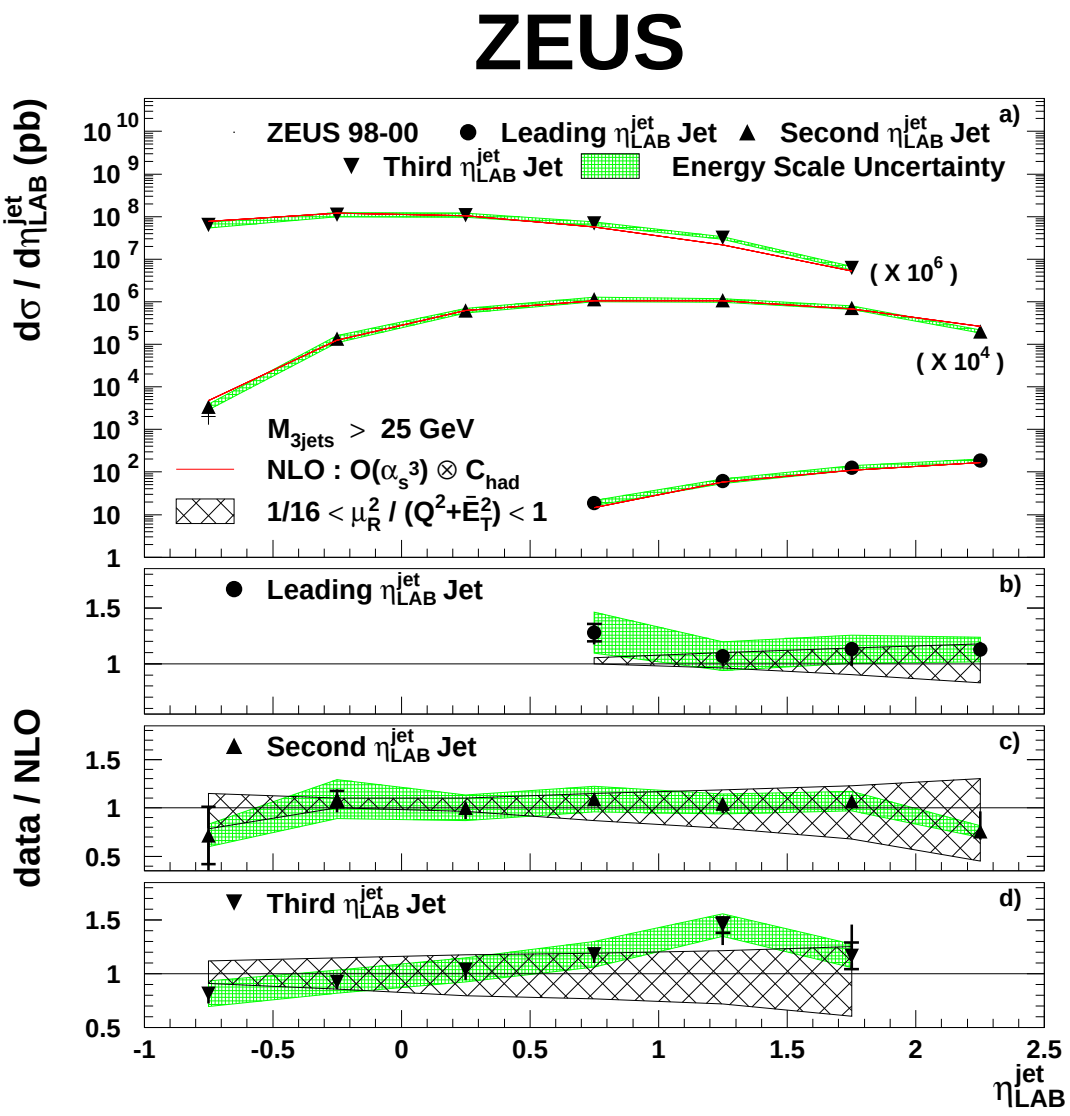

Figure 8.4: a) The inclusive trijet cross sections as functions of $\eta^{\rm jet}_{\rm LAB}$ with the jets ordered in $\eta^{\rm jet}_{\rm LAB}$. The cross sections of the second and third jet were scaled up for readability only. The predictions of perturbative QCD in next-to-leading order are compared to the data. b), c) and d) show the ratio of the data over predictions. Other details are as described in the caption to Fig. 8.1

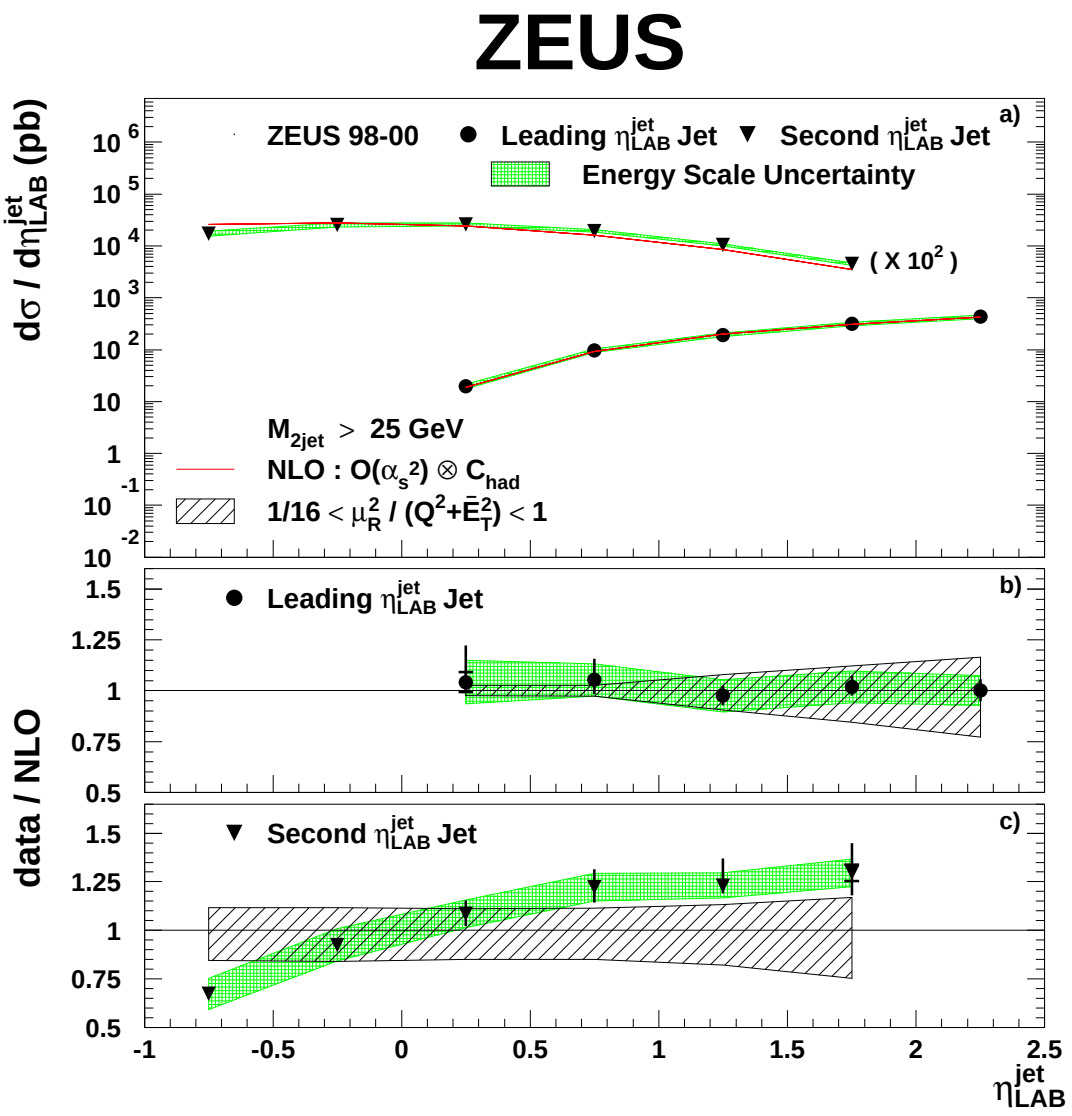

Figure 8.5: a) The inclusive dijet cross sections as functions of $\eta^{\rm jet}_{\rm LAB}$ with the jets ordered in $\eta^{\rm jet}_{\rm LAB}$. The cross sections of the second jet was scaled up for readability only. The predictions of perturbative QCD in next-to-leading order are compared to the data. b) and c) show the ratio of the data over predictions. Other details are as described in the caption to Fig. 8.1

ure 8.3. The two jets were ordered in $E_{T,B}$ ($E_{T,B}^{\mathrm{jet},1}$>$E_{T,B}^{\mathrm{jet},2}$). The observed decrease of the cross section for the first jet towards small values of $E_{T,B}$ is caused by the $E_{T,B}$ ordering as in the trijet case. At lowest $E_{T,B}$ bin of the first jet, there is some excess of the data over the NLO calculation. This might be due to the residual effects of the unphysical behavior of NLO calculation near the symmetric $E_{T,B}^{\mathrm{jet}}$ cut (Section 4.4). Overall, the NLO predictions describes the measured cross sections reasonably well for both the shape and magnitude.

For both Q^2 and $E_{T,B}^{\mathrm{jet}}$, the NLO predictions using NLOJET describes the measured cross sections well, showing that the NLO is capable of describing the data over a wide range of scales.

8.3 Measurement of the Differential Cross Section in $\eta_{\mathrm{LAB}}^{\mathrm{jet}}$

Figure 8.4 shows the differential trijet cross sections as functions of $\eta_{\mathrm{LAB}}^{\mathrm{jet}}$. The three jets were ordered in $\eta_{\mathrm{LAB}}^{\mathrm{jet}}$ ($\eta_{\mathrm{LAB}}^{jet,1}$>$\eta_{\mathrm{LAB}}^{\mathrm{jet},2}$>$\eta_{\mathrm{LAB}}^{\mathrm{jet},3}$). Due to this $\eta_{\mathrm{LAB}}^{\mathrm{jet}}$ ordering, the cross section of the most forward jet increases as $\eta_{\mathrm{LAB}}^{jet,1}$ increases while the cross section of the second forward jet and the most backward jet decrease as their $\eta_{\mathrm{LAB}}^{jet}$ go towards the forward boundary of the selected detector region. The measured cross sections are well described by the NLO calculation for both the shape and magnitude.

In general, the size of the renormalization scale uncertainty is comparable or bigger than the size of the measurement uncertainty. For high $\eta_{\mathrm{LAB}}^{\mathrm{jet}}$, theoretical uncertainty dominates. For middle and low $\eta_{\mathrm{LAB}}^{\mathrm{jet}}$, some decrease of the renormalization scale uncertainty is observed. This decrease is due to the different shape of the NLO predictions for different scales. The point where the renormalization scale uncertainty becomes minimal is the crossing point for the NLO predictions with different renor-

malization scales.

Figure 8.5 shows the differential dijet cross sections as functions of $\eta^{\rm jet}_{\rm LAB}$. The two jets were ordered in $\eta^{\rm jet}_{\rm LAB}$ ($\eta^{jet,1}_{\rm LAB}$>$\eta^{\rm jet,2}_{\rm LAB}$). Similar behavior of the cross section for the most forward and backward jet is observed as in the trijet case. Again, the measured cross sections are generally well described by the NLO calculation. The largest difference is a slightly different slope of the $\eta^{\rm jet}_{\rm LAB}$ dependence of the most backward jet.

8.4 Measurement of the Differential Cross-section Ratio and Determination of α_s

Figure 8.6 shows the cross-section ratio $R_{3/2}$ of trijet cross section to dijet cross section, as a function of Q^2. The correlated systematic and the renormalisation scale uncertainties largely cancel in the ratio. The agreement between the data and NLO predictions is good within substantially reduced uncertainties with respect to those of the di- and trijet cross sections. The total experimental and theoretical uncertainties are about 5% and 7% respectively. In particular, at low Q^2 ($Q^2 < 100$ GeV^2), the theoretical uncertainties are reduced by as much as a factor of four. This reduction allows the determination of $\alpha_s(M_Z)$ at a much lower Q^2 than in previous analyses [50, 51].

The measurement of $R_{3/2}$ as a function of Q^2 was used to determine $\alpha_s(M_Z)$ with a method similar to that of a previous ZEUS publication [52]:

- the NLO QCD calculation of $R_{3/2}$ was performed for five sets [22] of the CTEQ4

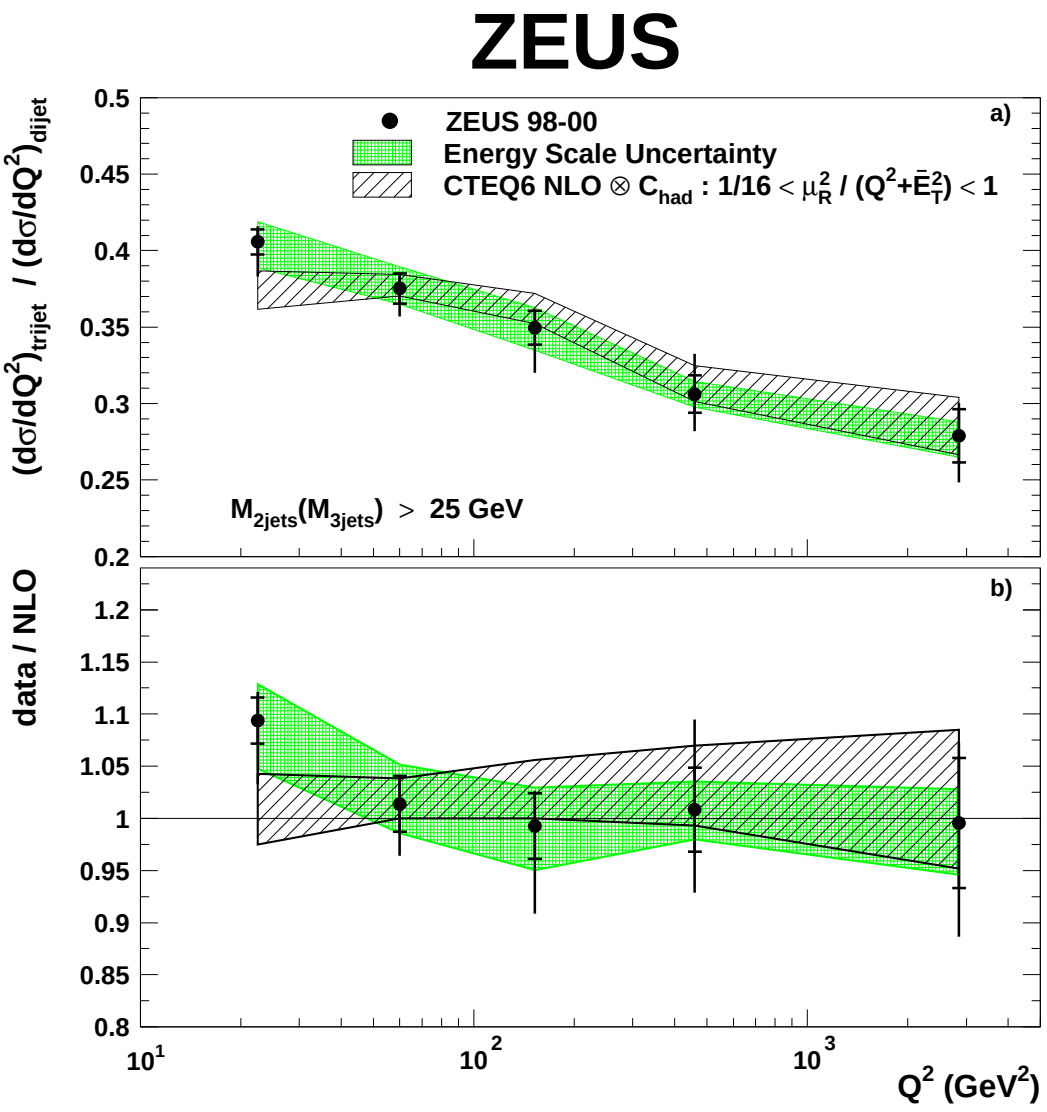

Figure 8.6: (a) The ratio of inclusive trijet over dijet cross section as a function of Q^2. The predictions of perturbative QCD in next-to-leading order are compared to the data. (b) shows the ratio of the data over the predictions. Other details are as in the caption to Fig. 8.1.

PDF[2] obtained assuming $\alpha_s(M_Z)$: 0.110, 0.113, 0.116, 0.119, 0.122;

- for each bin, i, in Q^2, the NLO QCD calculations, corrected for hadronisation effects, were used to parameterize the $\alpha_s(M_Z)$ dependence of $R_{3/2}$ according to the functional form:

$$[R_{3/2}(\alpha_s(M_Z))]^i = C_1^i \cdot \alpha_s(M_Z) + C_2^i \cdot \alpha_s^2(M_Z), \tag{8.1}$$

  where C_1^i and C_2^i are fitting parameters. This simple parameterization gives a good description of the $\alpha_s(M_Z)$ dependence of $R_{3/2}(Q^2)$ over the entire α_s range spanned by the PDF sets;

- a value of $\alpha_s(M_Z)$ was then determined in each bin of Q^2, as well as in the entire Q^2 region, by a χ^2-fit of the measured $R_{3/2}(Q^2)$ values using the parameterization in Eqn. 8.1.

This procedure correctly handles the complete α_s-dependence of the NLO differential cross sections (the explicit dependence coming from the partonic cross sections and the implicit one coming from the PDFs) in the fit, while preserving the correlation between α_s and the PDFs. Taking into account only the statistical uncertainties on the measured cross-section ratio, $\alpha_s(M_Z)$ is determined to be $\alpha_s(M_Z) = 0.1179 \pm 0.0013$(stat.).

Figure 8.7a shows the sensitivity of the cross-section ratio $R_{3/2}$ to the value of α_s. Figure 8.7b shows the $\alpha_s(M_Z)$ determined in the five bins of Q^2.

[2]The CTEQ4 PDF was chosen because the CTEQ6 does not provide PDF sets obtained with different $\alpha_s(M_Z)$ values and therefore can not be used for the determination of α_s.

As a cross-check of the extracted value of $\alpha_s(M_Z)$, the fit procedure was repeated by using the three sets of the MRST99 PDF corresponding to $\alpha_s(M_Z)$ equal 0.1125, 0.1175 and 0.1225. The result is $\alpha_s(M_Z) = 0.1178 \pm 0.0010$(stat.)

In addition, the NLO QCD analysis used to obtain the ZEUS-S PDF [7] was repeated to obtain a set of five PDFs corresponding to the values of $\alpha_s(M_Z)$: 0.115, 0.117, 0.119, 0.121, 0.123. These sets were used in the current analysis yielding $\alpha_s(M_Z) = 0.1191 \pm 0.0010$(stat.), in good agreement with the other determinations.

The experimental and theoretical uncertainties of the extracted value of $\alpha_s(M_Z)$ were evaluated by repeating the analysis above for each systematic check, as described in Section 8.5. The main contributions to the experimental systematic uncertainty in percentage are:

- *jet pseudorapidity cut* $^{+1}_{-1.5}\%$;
- *jet transverse energy and invariant mass cuts* $^{+0.5}_{-2}\%$;
- *use of different parton shower model* -2% ;
- *the absolute energy scale of the calorimeter* $^{+2}_{-2.5}\%$.

The main contributions to the theoretical uncertainty in percentage are:

- *uncertainties in the proton PDFs* $^{+1.5}_{-2}\%$;
- *uncertainties in the correction factor (*C_{had}*)* $+2\%$;
- *uncertainties due to terms beyond NLO* $^{+5}_{-3.5}\%$.

The value of $\alpha_s(M_Z)$ as determined from the measurements of $R_{3/2}$ is therefore:

$$\alpha_s(M_Z) = 0.1179 \pm 0.0013 \text{ (stat.)}^{+0.0028}_{-0.0046} \text{ (exp.)}^{+0.0064}_{-0.0046} \text{ (th.)}.$$

The result is in good agreement with recent determinations at HERA [53, 52, 51, 54, 55, 50, 56, 57, 58] and the current world average of $\alpha_s(M_Z) = 0.1182 \pm 0.0027$ [59].

8.5 Systematic Uncertainties

A detailed study of the experimental systematic uncertainties was performed [60]. The main sources contributing to the systematic uncertainties are listed below, for which an average value of the systematic uncertainties in the dijet cross section, cross-section ratio $R_{3/2}$ are indicated in parentheses correspondingly:

- *jet pseudorapidity cut* - a change of ± 0.1 (corresponding to the resolution) in the $\eta^{\text{jet}}_{\text{LAB}}$ cuts imposed on the jets in the laboratory frame for both data and MC simulated events (1%,1%);

- *jet transverse energy and invariant mass cuts* - $E^{\text{jet}}_{T,B}$ and $M_{\text{JJ}}(M_{\text{3J}})$ were simultaneously varied by the corresponding resolution near the cuts for both data and MC simulated events. Along with the previous systematic check, this takes into account the differences between the data and the MC simulation (3%,3%);

- *use of different parton shower model* - using ARIADNE instead of LEPTO to evaluate the acceptance corrections (2%,4%) ;

- *the absolute energy scale of the calorimeter, see Section 5.5.3* - varying $E^{\text{jet}}_{T,B}$ by its uncertainty of $\pm 1\%$ (>10 GeV) and $\pm 3\%$ (<10 GeV) for MC events [51] (6%,3.5%).

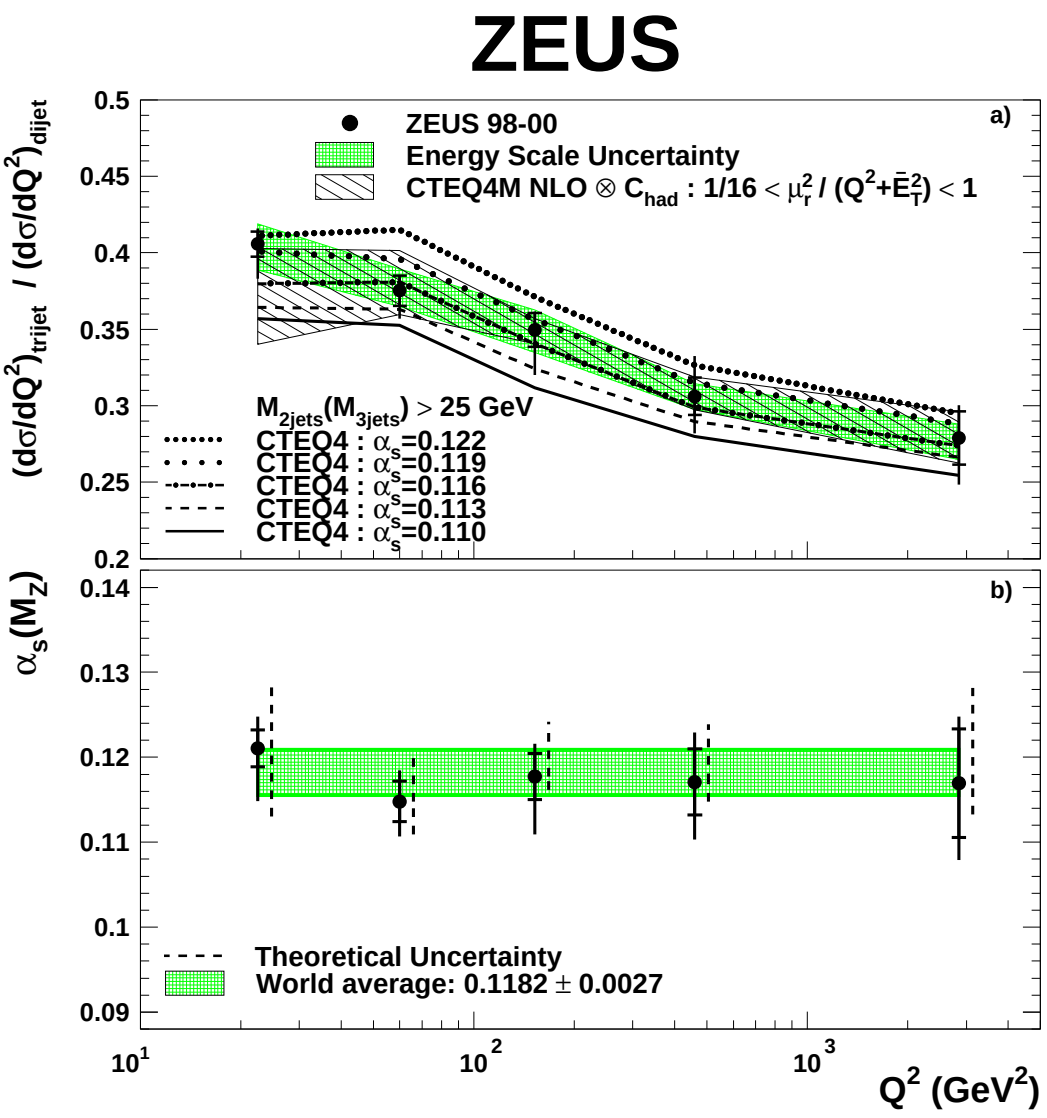

Figure 8.7: a) The ratio of inclusive trijet over dijet cross section as a function of Q^2. The predictions of perturbative QCD in next-to-leading order using five sets of CTEQ4 PDF are compared to the data. b) For each bin, a value of $\alpha_s(M_Z)$ has been extracted and is compared to the current world average. The shaded band indicates the current world average value of $\alpha_s(M_Z)$. The inner error bars represent the statistical uncertainty of the data. The outer error bars show the statistical and all systematic uncertainties added in quadrature. The dashed error bars display the theoretical uncertainties.

The systematic uncertainties not associated with the absolute energy scale of the calorimeter were added in quadrature to the statistical uncertainties and are shown on the figures as error bars. The uncertainty due to the absolute energy scale of the calorimeter is highly correlated from bin-to-bin and is shown separately as a shaded band [3].

There are also several other sources with negligible contributions to the overall experimental uncertainties, such as $E - P_Z$ cut, Z_{vertex} cut, y_e cut, y_{JB} cut, $\cos\gamma_h$ cut and the reweighting of the MC. The effects of those systematics are sufficiently small compared to the main sources mentioned above (e.g., the contribution from the reweighting of the MC is <0.4%), thus they are not included in the final systematic uncertainties.

The main contributions to the theoretical uncertainties of the NLO QCD predictions are:

- *uncertainties in the proton PDFs*, which were estimated by repeating the calculations using 40 additional sets obtained under different theoretical assumptions as part of the CTEQ6 release (2.5%,2%);

- *uncertainties in the correction factors,* C_{had}, which were estimated by using the ARIADNE program instead of LEPTO (6%,4%);

- *uncertainties due to terms beyond NLO*, which were estimated by varying both μ_R and μ_F between $(\bar{E}_T^2 + Q^2)$ and $(\bar{E}_T^2 + Q^2)/16$ (10%,7%).

[3]The uncertainty due to the luminosity measurement is 2.25%. This uncertainty comes from the way the luminosity is measured and is not included in this analysis (Section 2.2.3

The total theoretical uncertainty was obtained by adding in quadrature the individual uncertainties listed above.

Chapter 9

Conclusions and Outlook

The differential dijet and trijet cross sections have been measured with high precision in neutral current deep inelastic scattering for $10 < Q^2 < 5000\,\mathrm{GeV}^2$ at HERA using the ZEUS detector. The inclusive trijet cross section has been measured as a function of $E_{T,B}^{\mathrm{jet}}$, $\eta_{\mathrm{LAB}}^{\mathrm{jet}}$ and Q^2. The ratio $R_{3/2}$ of the trijet and dijet cross sections has been measured as function of Q^2. The predictions of perturbative QCD calculations in next-to-leading order give a good description of the dijet and trijet cross sections and the cross-section ratio $R_{3/2}$ over the whole range of Q^2. The cancellation of uncertainties in the ratio, in particular the theoretical ones, allow the extraction of α_s with good precision down to Q^2 of 10 GeV^2. The value of the strong coupling constant α_s was measured to be $\alpha_s(M_Z) = 0.1179 \pm 0.0013\ (\mathrm{stat.})^{+0.0028}_{-0.0046}\ (\mathrm{exp.})^{+0.0064}_{-0.0046}\ (\mathrm{th.})$, in good agreement with the current world average value and previous determinations of $\alpha_s(M_Z)$ at HERA.

Future improvement of this analysis can be made by reducing the systematic uncertainties, both experimental and theoretical uncertainties. The uncertainty of this measurement is dominated by the renormalization scale uncertainty, which indicates a more precise and higher order of calculation, e.g. NNLO calculation is needed. The

biggest experimental uncertainty is the energy scale uncertainty, which can be reduced by calibrating the energy scale of the calorimeter more precisely and by using the new HERA II data (Section 9.1). Other main sources of the experimental uncertainty are the parton shower model dependence and the description of the E_T and invariant mass distribution of the jets. These can be reduced by applying improved Monte Carlo models which describe the data sample better.

9.1 HERA II

During a long shutdown started in Sep 2000, the HERA collider underwent a major upgrade to improve its performance. The accelerator has had 480 meters of vacuum system replaced, and almost 80 magnets were newly designed and fitted, in order to focus the beams more strongly. These and other modifications of the interaction regions will result in a four-fold increase in the beam intensity, thus providing much more data for the experiments.

The ZEUS detector has been upgraded to take advantage of the expected floods of new data. The ZEUS collaboration has built and installed a new high-precision vertex detector, Micro Vertex Detector (MVD). This is a silicon detector which surrounds the collision point. Charged particles from a collision release an electrical charge in the silicon when they pass through it. This will give such an accurate measurement of their tracks that it will be possible to resolve the distances travelled by particles which live for only $10^{-}12$ second. The ZEUS collaboration has also upgraded the forward tracking system and trigger system.

These and other improvements mean that events with large momentum transfer will be even more precisely measured than before. HERA will be looking more

closely and accurately inside the proton than ever before, which allows accurate gluon determination and precise measurements of structure functions and heavy quarks. Furthermore, a completely new area of physics, opened up at HERA II, is the ability to study collisions between accelerated protons and polarized electrons or positrons. By switching between electrons and positrons of different polarizations, details of the way quarks interact with the weak force can be measured directly.

In Nov 2001, HERA II achieves design specific luminosity: $1.8{\cdot}10^{30}\mathrm{cm}^{-2}\mathrm{s}^{-1}\mathrm{mA}^{-2}$. The current plan is for HERA II to run, and allow the experiments to accumulate data, until 2006. By the end of this time, many more details of the proton, and of the quarks and gluons, will have been revealed.

The HERA II program aims at collecting a high luminosity sample of DIS data at higher E_T and Q^2. This analysis will benefit from the new HERA II data in many ways, e.g.:

- A tremendous increase in the experimental statistics (higher statistical precision).
- Improved kinematic reconstructions of both jets and the scattered electron in the forward region.
- At higher E_T and Q^2, jet energy and position are measured with high precision, yielding lower experimental uncertainties.

Bibliography

[1] W.A. Bardeen et al., Phys. Rev. **D 18**, 3998 (1978).

[2] F. Halzen and A.D. Martin, *Quarks and Leptons: An Introductory Course in Modern Particle Physics*. John Wiley & Sons, Inc, 1984.

[3] J.D. Bjorken, Phys. Rev. **179**, 1547 (1969).

[4] H1 Coll., S. Aid et al., Nucl. Phys. **B 470**, 3 (1996).

[5] V.N. Gribov and L.N. Lipatov, Sov. J. Nucl. Phys. **15**, 438 (1972);
L.N. Lipatov, Sov. J. Nucl. Phys. **20**, 94 (1975);
Yu.L. Dokshitzer, JETP **46**, 641 (1977);
G. Altarelli and G. Parisi, Nucl. Phys. **B 126**, 298 (1977).

[6] CTEQ Coll., R. Brock, Rev. Mod. Phys. **67**, 157 (1995).

[7] ZEUS Coll., S. Chekanov et al., Phys. Rev. **D 67**, 012007 (2003).

[8] A. D. Martin, R. G. Roberts, W. J. Stirling and R. S. Thorne, Eur. Phys. J. **C 28**, 455 (2003).

[9] J. Pumplin et al., Preprint hep-ph/0201195, 2002.

[10] ZEUS Coll., U. Holm (ed.), *The ZEUS Detector*. Status Report (unpublished), DESY (1993), available on `http://www-zeus.desy.de/bluebook/bluebook.html`;
ZEUS Coll., M. Derrick et al., Phys. Lett. **B 293**, 465 (1992).

[11] M. Derrick et al., Nucl. Inst. Meth. **A 309**, 77 (1991);
A. Andresen et al., Nucl. Inst. Meth. **A 309**, 101 (1991);
A. Caldwell et al., Nucl. Inst. Meth. **A 321**, 356 (1992);
A. Bernstein et al., Nucl. Inst. Meth. **A 336**, 23 (1993).

[12] N. Harnew et al., Nucl. Inst. Meth. **A 279**, 290 (1989);
B. Foster et al., Nucl. Phys. Proc. Suppl. **B 32**, 181 (1993);
B. Foster et al., Nucl. Inst. Meth. **A 338**, 254 (1994).

[13] I. Ambats et al., Nucl. Inst. Meth. **A 368**, 364 (1996).

[14] A. Bamberger et al., Nucl. Inst. Meth. **A 401**, 63 (1997).

[15] A. Bamberger et al., Nucl. Inst. Meth. **A 382**, 419 (1996).

[16] ZEUS Coll., J. Breitweg et al., Z. Phys. **C 74**, 207 (1997).

[17] W.H. Smith et al., Nucl. Inst. Meth. **A 355**, 278 (1995).

[18] G.P. Heath et al., Nucl. Inst. Meth. **A 315**, 431 (1992).

[19] H. Boterenbrood et al., Nucl. Inst. Meth. **A 332**, 263 (1993).

[20] G. Ingelman, A. Edin and J. Rathsman, Comp. Phys. Comm. **101**, 108 (1997).

[21] L. Lönnblad, Comp. Phys. Comm. **71**, 15 (1992).

[22] H.L. Lai et al., Phys. Rev. **D 55**, 1280 (1997).

[23] M. Bengtsson, G. Ingelman and T. Sjöstrand, *Proc. HERA Workshop*, R.D. Peccei (ed.), Vol. 1, pp. 149–165. DESY, Hamburg, Germany (1987).

[24] G. Gustafson and U. Pettersson, Nucl. Phys. **B 306**, 746 (1988).

[25] B. Andersson et al., Phys. Rep. **97**, 31 (1983).

[26] M. Bengtsson and T. Sjöstrand, Comp. Phys. Comm. **46**, 43 (1987).

[27] T. Sjöstrand, Comp. Phys. Comm. **82**, 74 (1994).

[28] B. R. Webber, Nucl. Phys. **B 238**, 492 (1984).

[29] A. Kwiatkowski, H. Spiesberger and H.-J. Möhring, Comp. Phys. Comm. **69**, 155 (1992). Also in *Proc. Workshop Physics at HERA*, 1991, DESY, Hamburg.

[30] K. Charchula, G.A. Schuler and H. Spiesberger, Comp. Phys. Comm. **81**, 381 (1994).

[31] R. Brun et al., GEANT3, Technical Report CERN-DD/EE/84-1, CERN, 1987.

[32] K. Fabricius et al., Z. Phys. **C11**, 315 (1982).

[33] R. K. Ellis, D. A. Ross and A. E. Terrano, Nucl. Phys. **B178**, 421 (1981).

[34] D. Chapin, *A Measurement of Dijet Production in Neutral Current Deep Inelastic Scattering with ZEUS at HERA*. Ph.D. Thesis, Univeristy of Wisconsin, Madison, 2001. Unpublished.

[35] Z. Nagy and Z. Trocsanyi, Phys. Rev. Lett. **87**, 082001 (2001).

[36] S. Catani and M. H. Seymour, Nucl. Phys. **B 485**, 291 (1997).

[37] A.D. Martin et al., Eur. Phys. J. **C 14**, 133 (2000).

[38] H. Abramowicz, A. Caldwell and R. Sinkus, Nucl. Inst. Meth. **A 365**, 508 (1995).

[39] K.C. Höger, *Proc. Workshop on Physics at HERA*, W. Buchmüller and G. Ingelman (eds.), Vol. 1, p. 43. Hamburg, Germany, DESY (1992).

[40] F. Jacquet and A. Blondel, *Proceedings of the Study for an ep Facility for Europe*, U. Amaldi (ed.), p. 391. Hamburg, Germany (1979). Also in preprint DESY 79/48.

[41] S. Bentvelsen, J. Engelen and P. Kooijman, *Proc. Workshop on Physics at HERA*, W. Buchmüller and G. Ingelman (eds.), Vol. 1, p. 23. Hamburg, Germany, DESY (1992).

[42] J.E. Huth et al., *Research Directions for the Decade. Proceedings of Summer Study on High Energy Physics, 1990*, E.L. Berger (ed.), p. 134. World Scientific (1992). Also in preprint FERMILAB-CONF-90-249-E.

[43] Seymour, M. H., Nucl. Phys. **B513**, 269 (1998).

[44] S.Catani et al., Nucl. Phys. **B406**, 187 (1993).

[45] S.D. Ellis and D.E. Soper, Phys. Rev. **D 48**, 3160 (1993).

[46] R.P. Feynman, *Photon-Hadron Interactions*. Benjamin, New York, 1972;
K.H. Streng, T.F. Walsh, P.M. Zerwas, Z. Phys. **C 2**, 237 (1979).

[47] O. Gonzalez, *Precise determinations of the strong coupling constant at HERA*. Ph.D. Thesis, Universidad Autonoma de Madrid, Report DESY-THESIS-2002-020, 2002.

[48] ZEUS Coll., J. Breitweg et al., Eur. Phys. J. **C 11**, 427 (1999).

[49] M. Wodarczyk, *Measurement of the F_2 Structure Function of the Proton at HERA from 1996 and 1997 ZEUS Data*. Ph.D. Thesis, University of Wisconsin, 1999.

[50] ZEUS Coll., S. Chekanov et al., Nucl. Phys. **B 700**, 3 (2004).

[51] ZEUS Coll., S. Chekanov et al., Phys. Lett. **B 547**, 164 (2002).

[52] ZEUS Coll., J. Breitweg et al., Phys. Lett. **B 507**, 70 (2001).

[53] ZEUS Coll., M. Derrick et al., Phys. Lett. **B 363**, 201 (1995).

[54] ZEUS Coll., S. Chekanov et al., Phys. Lett. **B 558**, 41 (2003).

[55] ZEUS Coll., S. Chekanov et al., Phys. Lett. **B 560**, 7 (2003).

[56] H1 Coll., C. Adloff et al., Eur. Phys. J. **C 6**, 575 (1999).

[57] H1 Coll., C. Adloff et al., Eur. Phys. J. **C 19**, 289 (2001).

[58] H1 Coll., C. Adloff et al., Eur. Phys. J. **C 21**, 33 (2001).

[59] S. Bethke, J. Phys. **G 26**, R27 (2000);
S. Bethke, Preprint hep-ex/0407021, 2004. Talk given at 7th DESY Workshop on Elementary Particle Theory: Loops and Legs in Quantum Field Theory, Zinnowitz, Germany, 25-30 Apr 2004.

[60] N. Krumnack, *Three Jet Events in Deep Inelastic Scattering.* Ph.D. Thesis, University of Hamburg, 2004.